UNIVERSIDADE FEDERAL DO CEARÁ
CENTRO DE CIÊNCIAS
DEPARTAMENTO DE FÍSICA
PROGRAMA DE PÓS-GRADUAÇÃO EM FÍSICA

UNIVERSITEIT ANTWERPEN
FACULTEIT WETENSCHAPPEN
DEPARTEMENT FYSICA

Jorge Luiz Coelho Domingos

Estudo de sistemas coloidais de partículas anisotrópicas magnéticas

---

Study of colloidal systems of anisotropic magnetic particles

Studie van colloïdale systemen van magnetische anisotrope deeltjes.

Fortaleza
2018

Jorge Luiz Coelho Domingos

Estudo de sistemas coloidais de partículas anisotrópicas magnéticas

---

Study of colloidal systems of anisotropic magnetic particles

Studie van colloïdale systemen van magnetische anisotrope deeltjes.

Tese apresentada ao Curso de Pós-graduação em Física da Universidade Federal do Ceará como parte dos requisitos necessários para a obtenção do título de Doutor em Física.

Orientador:
Prof. Dr. Wandemberg Paiva Ferreira

Co-orientador:
Prof. Dr. François M. Peeters

DOUTORADO EM FÍSICA
DEPARTAMENTO DE FÍSICA
PROGRAMA DE PÓS-GRADUAÇÃO EM FÍSICA
CENTRO DE CIÊNCIAS
UNIVERSIDADE FEDERAL DO CEARÁ

Fortaleza - CE
15 de março de 2018

Dados Internacionais de Catalogação na Publicação
Universidade Federal do Ceará
Biblioteca Universitária
Gerada automaticamente pelo módulo Catalog, mediante os dados fornecidos pelo(a) autor(a)

C617e Coelho Domingos, Jorge Luiz.
Estudo de sistemas coloidais de partículas anistrópicas magnéticas / Jorge Luiz Coelho Domingos. – 2018.
114 f. : il. color.

Tese (doutorado) – Universidade Federal do Ceará, Centro de Ciências, Programa de Pós-Graduação em Física , Fortaleza, 2018.
Orientação: Prof. Dr. Wandemberg Paiva Ferreira.
Coorientação: Prof. Dr. François Maria Leopold Peeters.

1. Matéria mole. 2. Auto-organização. 3. Colóides magnéticos. 4. Percolação. 5. Dinâmica Molecular. I. Título.
CDD 530

JORGE LUIZ COELHO DOMINGOS

STUDY OF COLLOIDAL SYSTEMS OF ANISOTROPIC MAGNETIC PARTICLES

Tese de Doutorado apresentada ao Programa de Pós-Graduação em Física do Departamento de Física da Universidade Federal do Ceará, como requisito parcial para obtenção do título de Doutor em Física. Área de concentração: Física da Matéria Condensada.

Aprovada em: 15/03/2018.

BANCA EXAMINADORA

Dr. Wandemberg Paiva Ferreira (Orientador)
Universidade Federal do Ceará (UFC)

Dr. Gil de Aquino Farias
Universidade Federal do Ceará (UFC)

Dr. Pierre Basílio Fechine
Universidade Federal do Ceará (UFC)

Dr. François Maria Leopold Peeters
University Antwerp (Bélgica)

Dr. Diego Rabêlo da Costa
University of Minnesota (UM)

Dr. Luciano Rodrigues da Silva
Universidade Federal do Rio Grande do Norte (UFRN)

To my parents, close relatives and friends.
To Izabel Jurandir (in memoriam),
Fernando Coelho (in memoriam), Jamys
Holmes (in memoriam) and Jehovah Coelho
(in memoriam).

Acknowledgments

To God, parents (Jorge and Cristina) and my wife (Hiatanara), because I owe it all to you for supporting me in my darkest and sadly days, for believing me when I was discredited and for always helping me to keep moving on. A special mention to my aunt (Terezinha) and my cousin (Romero), for all encouragement. You are great! Love you all!!

To my former teacher Luciana Colares (Tia Lulu), whom I express my eternal gratitude for her advices, support and love. Thank you.

To my supervisor, Prof. Dr. Wandemberg, for his guidance, support and friendship since my scientific initiation. I am really grateful. To my co-supervisor, Prof. Dr. François Peeters for all his insightful comments to improve this thesis and for his support during my stay in Belgium. Thank you. I would also like to thank Prof. Dr. Felipe Munarin, for help me a lot in the beginning of my PhD.

I thank the other members of the jury, Prof. Gil de Aquino, Prof. Luciano da Silva, Prof. Pierre Fechine and Dr. Diego Rabelo for the time spent reviewing this work, as well as for their very important comments, corrections and suggestions that made possible to improve the quality of the final version of this thesis.

I am grateful to all my friends for accepting nothing less than excellence for me. All of you, directly or indirectly involved in my thesis, helped me to move forward when the troubles appeared. With a special mention to my GTMC colleagues: *Diego Rabelo*, *Davi Soares*, *Jorge Bezerra*, *Danilo Borges*, *Diego Lucena* and *Levi*, also to my CMT colleagues: *Victor*, *Rebeca* and *Luca*. It is and it has always been a pleasure to share a time with you. For those friends not-involved directly in my thesis, it would be unfair if I forgot any names, so I'll just keep it simple and plain: Thank you very much for all the support throughout these years.

I would also like to thank all the employees and professors from the Department of Physics of Universidade Federal do Ceará (UFC) and from the Department of Physics of Universiteit Antwerpen (UA). Last but not least, I would like to thank the Brazilian agencies CNPq, CAPES, FUNCAP, and the Flemish agency FWO, for financial support.

"Eu sou de uma terra que o povo padece
Mas não esmorece e procura vencer.
Da terra querida, que a linda cabocla
De riso na boca zomba no sofrer
Não nego meu sangue, não nego meu nome
Olho para a fome, pergunto o que há?
Eu sou brasileiro, filho do Nordeste,
Sou cabra da Peste, sou do Ceará.."

Patativa do Assaré

Resumo

O processo de auto-organização de um sistema bidimensional de barras magnéticas é estudado. As barras são modeladas como contas dipolares unidas e alinhadas, o chamado modelo *vagem*. O sistema é estudado por meio das simulações de Dinâmica Molecular e Dinâmica de Langevin. Inicialmente, uma introdução sobre os sistemas de matéria mole, mostrando suas principais características e alguns aspectos teóricos e experimentais é apresentada. A seguir, são apresentados e discutidos os métodos computacionais adotados nas simulações, bem como o tratamento matemático do sistema. Quanto aos resultados da tese, uma diversidade de configurações auto-organizadas, tais como: (1) aglomerados, (2) percolados e (3) estruturas ordenadas são obtidas e caracterizadas em relação ao estado de agregação das partículas e ordenamento. Ao aumentar a razão de aspecto das barras magnéticas, verifica-se que em duas dimensões a transição de percolação é suprimida. Este resultado é oposto ao que é observado em sistemas semelhantes em três dimensões. Mostra-se que esse comportamento é uma conseqüência de efeitos geométricos que reduzem a mobilidade das barras à medida que a razão de aspecto destas é aumentada. No que diz respeito ao ordenamento das partículas no sistema, uma fase magnética é encontrada com ordenamento ferromagnético local, e também é observado um comportamento não monotônico incomum da ordem nemática. Com base também em simulações de Dinâmica de Langevin, as configurações auto-organizadas são estudadas para o caso especial em que o dipolo das contas que constituem as barras está desalinhado em relação ao eixo da barra. O desalinhamento é zero quando o dipolo é paralelo ao eixo axial. Verificou-se que a densidade necessária para a formação da estrutura percolada diminui com o aumento do desalinhamento do dipolo. Além disso, o sistema exibe diferentes estados de agregação (sólido ou líquido) para diferentes desalinhamentos, mesmo quando a mesma densidade é considerada. A estabilidade das estruturas auto-organizadas é estudada em relação à temperatura, e geralmente aumenta com o aumento do desalinhamento dos dipolos.

***Palavras-chave**: Matéria mole; Auto-organização; Colóides magnéticos; Percolação; Dinâmica Molecular; Dinâmica de Langevin.*

Abstract

The self-assembly process of a two-dimensional ensemble of magnetic rods is studied. The rods are modelled as aligned single dipolar beads, the so-called peapod model. The system is studied by means of Molecular Dynamics and Langevin Dynamics simulations. An introduction on soft matter systems, showing their main features and some theoretical and experimental aspects is first presented. In the following, the computational methods adopted in the simulations and the mathematical treatment of the system are presented and discussed. Concerning the results of the thesis, a diversity of self-assembled configurations such as: (1) clusters, (2) percolated and (3) ordered structures are obtained and characterized with respect to the state of aggregation of the particles and ordering. By increasing the aspect ratio of the magnetic rods, it is found that in two dimensions the percolation transition is suppressed. This is opposite to what is observed in similar three dimensional systems. It is shown that such a behavior is a consequence of geometrical effects which reduce the mobility of the rods as the aspect ratio of such rods is increased. Concerning the ordering of the particles in the system, a magnetic bulk phase is found with local ferromagnetic order and an unusual non-monotonic behavior of the nematic order is also observed. Based also on extensive Langevin Dynamics simulations, the self-assembled configurations are studied for the special case where the dipole of the beads that constitute the rods are misaligned with respect to the rod axis. The misalignment is zero when the dipole is parallel to the axial axis. It is found that the density required for the formation of the percolated structure decreases with increasing misalignment of the dipole. Also, the system exhibits different aggregation states (solid or liquid) for different misalignment, even when the same density is considered. The stability of the self-assembled structures are studied with respect to temperature, and it usually increases with increasing misalignment of the dipoles.

Keywords: *Soft-Matter; Self-assembly; Magnetic colloids; Percolation; Molecular Dynamics; Langevin Dynamics.*

Abstract

Het zelf-assemblageproces van een tweedimensionaal ensemble van magnetische staven wordt bestudeerd. De staven zijn gemodelleerd als uitgelijnde enkele dipolaire kralen, het zogenaamde peapod-model. Het systeem wordt bestudeerd met behulp van Moleculaire Dynamica en Langevin Dynamica-simulaties. Een inleiding over zachte-materie-systemen, waarin hun belangrijkste kenmerken en enkele theoretische en experimentele aspecten worden besnoken. Vewolgens worden de berekeningsmethoden die in de simulaties en de wiskundige behandeling van het systeem zijn gebruikt gepresenteerd en besproken. Met betrekking tot de resultaten van het proefschrift, wordt een diversiteit aan zelf-geassembleerde configuraties zoals: (1) clusters, (2) gepercoleerde en (3) geordende structuren verkregen en gekarakteriseerd met betrekking tot aggregatietoestand van de deeltjes en ordening. Door de aspect-verhouding van de magnetische staven te vergroten, vonden we dat in twee dimensies de percolatietransitie wordt onderdrukt. Dit is tegengesteld aan wat wordt waargenomen in vergelijkbare driedimensionale systemen. Er wordt aangetoond dat een dergelijk gedrag een gevolg is van geometrische effecten die de mobiliteit van de staven verminderen, aangezien de aspect-verhouding van dergelijke staven toeneemt. Wat betreft de ordening van de deeltjes in het systeem, wordt een magnetische bulkfase gevonden met lokale ferromagnetische orde en een ongewoon niet-monotoon gedrag van de nematische orde wordt ook waargenomen. Gebaseerd op uitgebreide Langevin Dynamica-simulaties, worden de zelf-geassembleerde configuraties bestudeerd voor het speciale geval waarbij de dipool van de korrels die de staven vormen, ten opzichte van de staafas niet goed uitgelijnd is. De foutieve uitlijning is nul wanneer de dipool parallel is aan de axiale as. We vonden dat de dichtheid die vereist is voor de vorming van de gepercoleerde structuur afneemt met toenemende foutieve uitlijning van de dipool. Ook vertoont het systeem verschillende aggregatietoestanden (vast of vloeibaar) voor verschillende scheefstanden, zelfs wanneer dezelfde dichtheid wordt beschouwd. De stabiliteit van de zelf-geassembleerde structuren wordt bestudeerd met betrekking tot temperatuur, en deze neemt gewoonlijk toe met toenemende scheefstand van de dipolen.

***Trefwoorden**: Soft-Matter; Zelfassemblage; Magnetische colloïden; Percolatie; Moleculaire dynamica; Langevin-dynamica.*

Contents

List of Figures

List of abbreviations

$2D$	Two-dimensional
$3D$	Three-dimensional
LCDs	Liquid crystal displays
LJ	Lennard-Jones
DHS	Dipolar hard sphere model
DSS	Dipolar soft sphere model
ST	Stockmayer model
MN	Magnetic nanoparticles
FN	Ferromagnetic nanoparticles
TEM	Transmission electron microscopy
MNR	Magnetic nanorods
FESEM	Field-emission scanning electron microscope
LC	Liquid crystals
MD	Molecular dynamics
CM	Center of mass
PBC	Periodic boundary conditions
RDF	Radial distribution function
FS	Flory-Stockmayer
MSD	Mean square displacement
VACF	Velocity autocorrelation function
LD	Langevin dynamics
MRI	Magnetic resonance imaging
AHS	Adhesive hard sphere

List of nomenclatures

k_B	Boltzmann constant
T	Temperature
σ	Shear stress, particle diameter
$\mathbf{F}$	Force
V	Volume, interaction potential
N	Number of particles
K	Bulk modulus, kinetic energy
G	Shear modulus
γ	Strain
A_H	Hamaker constant
D	Diffusion coeficient
ϵ	LJ interaction constant
$\boldsymbol{\mu}$	Dipole moment
l	Aspect ratio
L	Lagrangian
H	Hamiltonian
m	Mass
I	Moment of Inertia
$\mathbf{s}$	Orientation vector
$\mathbf{L}$	Angular momentum
$\boldsymbol{\omega}$	Angular velocity
$\mathbf{u}$	Tangential velocity
$\boldsymbol{\alpha}$	Tangential acceleration
$\mathbf{r}$	Particle position
$\mathbf{v}$	Center of mass velocity
$\mathbf{R}$	Center of mass position
$\boldsymbol{\eta}$	Packing fraction
$\mathbf{B}$	Magnetic field
Re	Reynolds number
Ψ	Misalignment of dipole
$\mathbf{N}, \boldsymbol{\tau}$	Torque
Γ	Friction coefficient constant
$\boldsymbol{\xi}$	Generalized Gaussian force

Part I

Introduction

1

Introduction and Overview

1.1 Soft Matter systems

Probably, condensed matter physics is the most explored field in Physical Sciences. From the need to study systems with a large group of interacting particles, as liquid and solids, it provides a framework for describing and determining the macroscopic and microscopic properties of matter [1]. However, condensed matter physics can be split into "hard" condensed matter physics, which studies quantum properties of matter, and "soft" condensed matter physics which studies those properties of matter for which quantum mechanics plays no role. The latter is related to systems which cannot be defined either as simple liquids or crystalline solids, they are usually refereed as *soft matter*. Polymers, colloids, surfactants and liquid crystals are prominent examples of soft matter (see Fig.

Figure 1.1: Examples of soft matter systems. Top panel: (left) polystyrene (polymers), and (right) jelly (colloids). Bottom panel: (left) detergents (surfactants), and (right) LCDs (liquid crystals).

1.1). Even though they are presented as being different materials, currently it is assumed that there is a continuum group of molecules and systems that they can be fit into the distinguished-behavior-gap between those four examples of basic soft materials [2] as shown in Fig. 1.2. Although they might not seem to be a broad class of molecules, the first three examples are primary materials of which the biological matter is made, excepting the bone's material and water. Because of that, there is a close relationship between soft matter physics and biophysics.

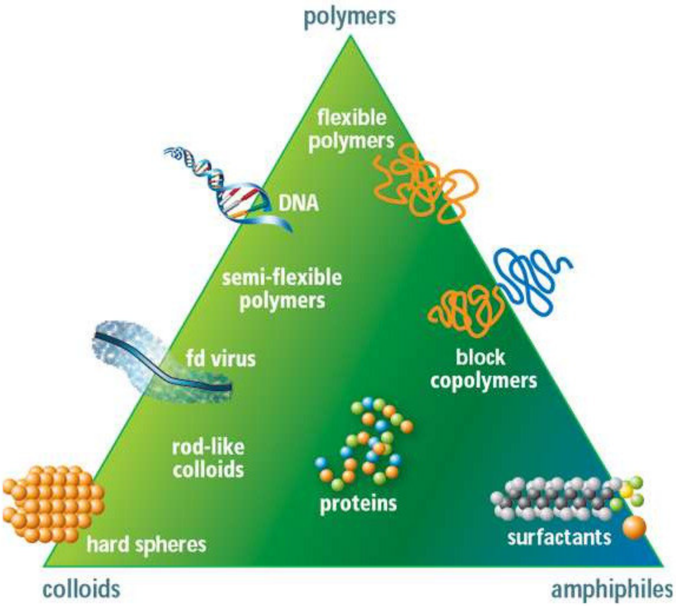

Figure 1.2: Illustrative triangle showing the continuum of molecules and materials which fills the space between spherical colloids, flexible polymers, and surfactants. Extracted from Ref. [2].

Some common features of soft matter systems are, for example, their characteristic length scales between the atomic sizes and macroscopic scales. This important feature makes soft matter systems easier to study, from the point of view of experimental set up. Concerning the theoretical description and computer simulations one can use *coarse-grained* models that does not concern about every detail of the atomic scale, as chemical bonds, hybridization or any quantum effects. Another feature is that soft matter shows a large and nonlinear response to weak forces, for instance, rubbers (polymers) can be stretched by a factor of 2, 3 or even more from their initial length and their mechanical response cannot be described by a linear relation between stress and strain [4, 5]. Also, because of their length scale, they are subject to Brownian motion [3], which makes that their common physical properties have energy scales of the order of $k_B T$, confirming that the quantum effects can be neglected. If the interaction between the constituents are weak enough, thermal agitations, resultant from Brownian dynamics, will allow the elements to adjust their positions and orientation to attain the most favourable configuration. Such a process is called *self assembly* and it leads soft matter systems to a hierarchically more complex and ordered state of aggregation. The characteristic length scale and the weak interactions are the reasons why soft matter is soft. There are two material parameters whose softness can be evaluated, namely, the bulk modulus (K) and the shear modulus (G). The latter comes from the shear stress (σ) definition:

$$\sigma = G\gamma, \tag{1.1}$$

where γ is the strain (relative deformation in a material), and G is the elasticity constant which is defined as the ratio between the force and the area, i.e., the pressure units. Therefore it can also be expressed as the ratio between the energy involved and the volume (Eq. 1.2)

$$G = \frac{F}{A} = \frac{E}{V}. \tag{1.2}$$

Typically, for a molecular solids, the energy involved is basically the binding energy ($E \approx 1$ eV) and the length scale is on the order of interatomic distances ($V \approx 1\text{Å}^3$). Therefore, as the bulk modulus is $K \approx 3G$, it is on the order of GPa. If we do the same analysis for soft matter systems we have, e.g. for colloids, $E \approx k_BT$ and $V \approx 1$ nm^3, therefore $G \approx 4$ mPa. Consequently, the bulk modulus for typical colloids differ about 13 orders of magnitude from molecular solids. In general, soft materials are typically somewhere between 11 and 14 orders of magnitude softer than regular materials [4]. One relevant class of soft matter system are the colloidal dispersions. Such systems play an important role in the soft self assembled structures, and are the object of the study of the present thesis. Firstly, let us discuss about colloidal dispersions in more detail.

1.2 Colloidal Dispersion

Colloidal systems refer to systems consisting of small particles suspended in a fluid whose typical size is between 1 nm up to 20 μm. They often behave either like regular liquids or regular solids see (Fig. 1.3). The difference from molecular and atomic systems is that the primary constituents, the small particles, can be large enough that you can see under a microscope. Phase transitions (like crystallization, gas-liquid phase separation and formation of nematics and smectics) and critical phenomena (like critical slowing down of diffusion and critical opalescence) are amongst the phenomena that colloidal systems have in common with molecular systems. Because of that, colloids have been also used as model systems for understanding many properties of molecular or even atomic materials. Also, their dynamics are slow, in particular we can follow them in real time watching their dynamics using, for example, *video microscopy* technique. One way to describe that is using the diffusion coefficient definition (D) in terms of the thermal energy (k_BT), viscosity (η) and the particle diameter (a), where, roughly speaking, $D \approx k_BT/\eta a$. Due to the relative large length scale of a, the diffusion coefficient of soft materials are typically 4 orders of magnitude smaller than typical coefficient values of hard materials. Thus, the typical relaxation are somewhere between microseconds and hundred of seconds.

Therefore the experimental study of colloids is usually much simpler than for molecular systems. The dispersed particles are large enough to describe the solvent as a continuous and homogeneous background. However they are small enough to present Brownian motion which arises from collisions of particles and solvent. As a result, the kinetic energy of colloids K is closely related to the kinetic energy of particles of the solvent, or the kinetic energy of colloids conform to Boltzmann distribution

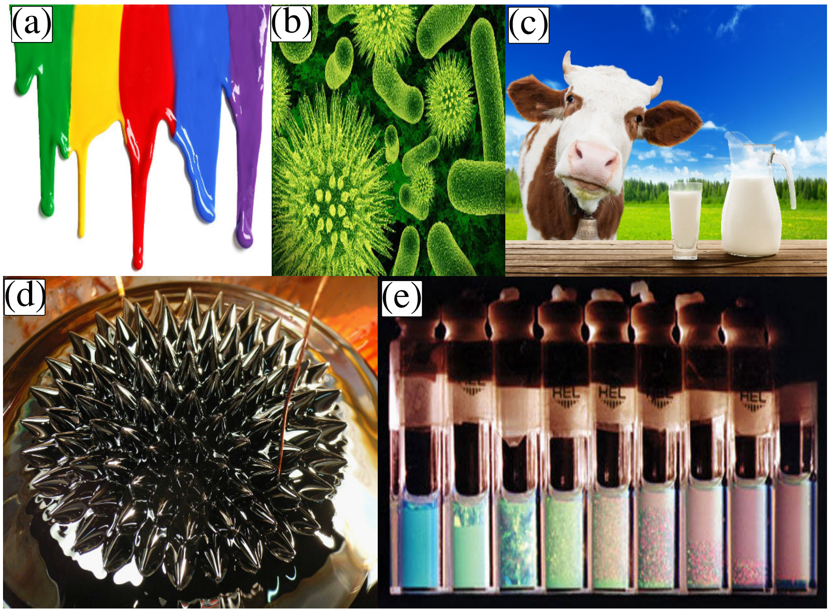

Figure 1.3: Examples of colloids. (a) Paints. (b) Viruses. (c) Milk. (d) Ferrofluid. (f) Colloidal Crystals.

$$p(K)\ \alpha\ exp\left(-\frac{K}{k_BT}\right), \tag{1.3}$$

where $k_B = 1.38 \times 10^{-23}\ J/K$ is the Boltzmann constant and T is the absolute temperature. If the colloids are subjected to an external potential also conforms to the Boltzmann distribution according to the Virial theorem, then:

$$p(V)\ \alpha\ exp\left(-\frac{V}{k_BT}\right) \quad \text{or} \quad p(r)\ \alpha\ exp\left(-\frac{V(r)}{k_BT}\right). \tag{1.4}$$

1.2.1 Pair interaction between colloids

♦ van der Walls interaction

It arises from the fact that all colloids attract each other, with a few caveats. The uncharged colloids weakly interacts via a fluctuating induced dipolar force between the neighbouring atom or molecule. As a result, it leads to an attractive force. If the van der Walls is the only interaction which is present, the colloidal suspension is unstable, because the colloids would attract each other turning into a big mass that fall to the bottom of the suspension. This instability can be overcomed by, e.g., charging the colloids in order that *screened Coulomb* interaction counteracts the van der Walls attraction. This brings to a topic of the colloidal stability. The potential U_{pd} between a pair of dipoles which one dipole is induced by one another, separated by a distance r varies as

$$U_{pd} \sim \frac{1}{r^6}. \tag{1.5}$$

After a double integration over the volume of the (two identical) colloids, we end up into this expression [6]

$$U_{vw}(r) = -A_H \left[\frac{2R^2}{r^2 - 4R^2} + \frac{2R^2}{r} + \ln\left(1 + \frac{4R^2}{r^2}\right) \right], \tag{1.6}$$

where R is the particle radius, r is the center-to-center distance, and A_H is the Hamaker constant, which depends on the dielectric constant of the particles and of the medium. Typical values of A_H is around $\approx 10k_BT$, for typical length scale of colloids, $U_{vw} \approx 500k_BT$ [5], therefore, the van der Walls interaction is strong.

♦ Lennard-Jones potential

Roughly speaking, the microscopic model for any system which exhibits any of the most common states of matter as solid, liquid and gas is based on spherical particles that interact with one another. Therefore a pair interaction that provides, at the simplest level, the two principal features of an interatomic force: close-range repulsion and short-range attraction is the Lennard-Jones (LJ) potential which is the best known of such potentials, originally proposed for liquid argon [7]. The LJ potential is a very simple model widely used to simulate colloids. It counts of a short-range attractive term (van der Walls) and

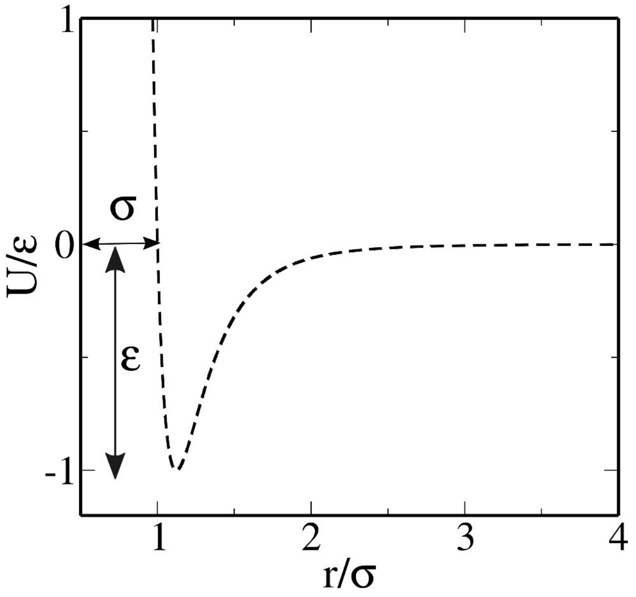

Figure 1.4: Lennard-Jones potential curve.

a repulsive term which comes from the *Pauli repulsion* at close ranges due to overlapping electron orbitals. The most common expression for the LJ potential is [7, 8]

$$U_{LJ} = \begin{cases} 4\epsilon \left[\left(\frac{\sigma}{r}\right)^{12} - \left(\frac{\sigma}{r}\right)^{6} \right] & r \le r_c, \\ 0 & r > r_c, \end{cases} \tag{1.7}$$

where σ is the particle diameter and it is related to the length scale, which is usually normalized to the particle diameter. ϵ is the depth of the potential well which governs the strength of the interaction (see Fig. 1.4). The interaction repels at close range, then attracts till a cut off limiting separation r_c.

♦ Polar colloids interaction

Here we present some of the frequently studied model in the context of the dipolar colloids. We can point to three models: dipolar hard sphere (DHS), Stockmayer model (ST) and dipolar soft sphere (DSS) model. A common feature of the aforementioned three models is the description of long-range anisotropic interaction in terms of a point dipole-dipole potential. However, they differ in the short range interaction. In addition with the dipolar term, the DHS model employs hard core repulsion, whereas the ST potential employs the Lennard-Jones (LJ) potential. The intermediate DSS model adopts the soft repulsive core of the LJ potential. The fields of applications for these three model potentials are the same, they are used as simple models for polar molecules. All three models, DHS, DSS and ST, exhibit a transition from an isotropic liquid to an orientationally ordered liquid and show quite similar dielectric properties, whereas a gas-liquid (GL) transition is established for the ST fluid only [9, 10], and it is still a matter of debate. In this thesis we focus on the DSS to simulate the interaction of the system, however, further information about the not-covered interactions can be found in the Refs. [9, 11] for DHS model, and Refs. [12, 13] for ST model.

- Dipolar soft sphere interaction

As mentioned previously, the DSS potential is the dipolar interaction added of the soft repulsive core of the LJ potential. The DSS is expected to show the same phase behavior like the DHS model [14]

$$U^{DSS} = \frac{\boldsymbol{\mu}_i \cdot \boldsymbol{\mu}_j}{r_{ij}^3} - \frac{3(\boldsymbol{\mu}_i \cdot \mathbf{r}_{ij})(\boldsymbol{\mu}_j \cdot \mathbf{r}_{ij})}{r_{ij}^5} + 4\epsilon \left(\frac{\sigma}{r_{ij}} \right)^{12}, \tag{1.8}$$

where $\mathbf{r}_{ij} = \mathbf{r}_j - \mathbf{r}_i$, $r_{ij} = \|\mathbf{r}_{ij}\|$ and $\boldsymbol{\mu}_i$ is the dipole moment of ith particle. Due to the presence of the repulsive LJ-term, the dimensionless units are similar to the ones in the LJ model. The interaction depends on the relative orientation of the particles. The most favourable arrangement, as shown in Fig. 1.5, is the so-called head-to-tail arrangement (red dashed-line), presenting a similar behavior to the LJ curve (black solid line).

Particles which can be modelled with dipolar interaction must present a magnetic monodomain. In general, the size of the particles rules this feature. The typical length

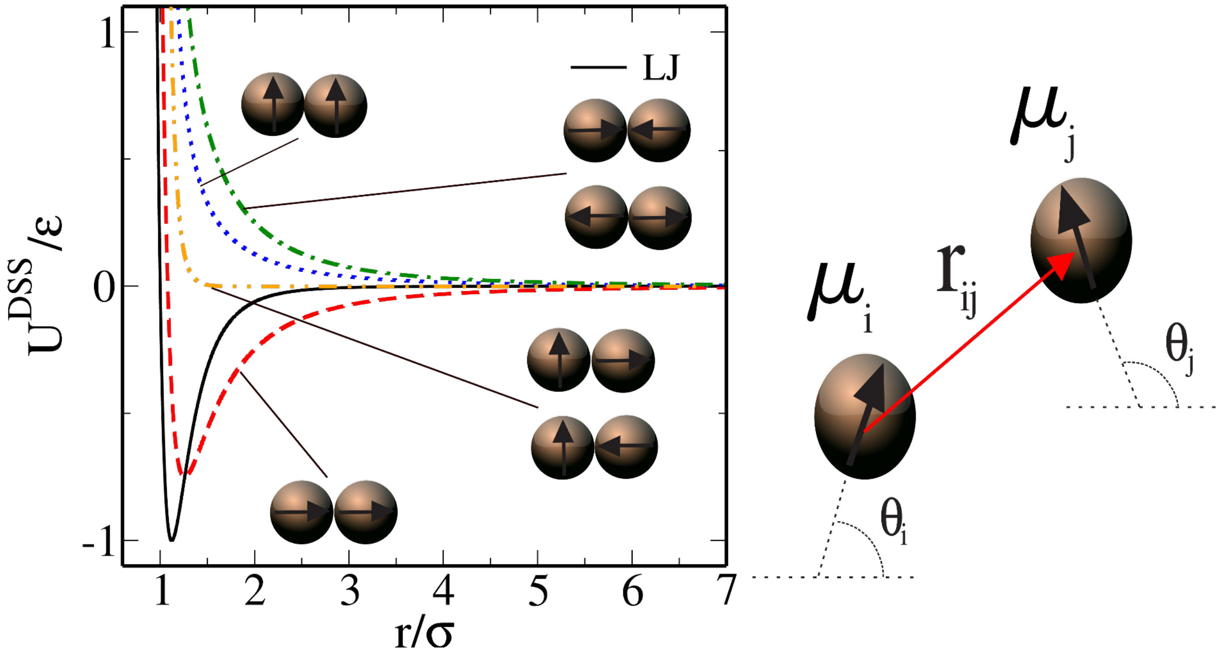

Figure 1.5: Total DSS pair potential for different configurations as a function of the interparticle separation. For comparison purposes, LJ curve is also plotted in the black solid line. A sketch with the relevant parameters in the interaction is also shown.

scale of the dipolar particles is on the order of the nanometers, so they are refereed as magnetic nanoparticles. In the following sections, we sometimes make reference to the modelled particles in this term.

1.2.2 Magnetic Nanoparticles

Magnetic nanoparticles (MN) are used in different applications, including magnetic fluids [15], biomedicine [16], magnetic resonance imaging (MRI) [17], data storage [18], among others. Basically, MN are particles with a magnetic dipole moment associated, which are regarded as particles composed of a magnetic monodomain when they have a typical size from 15 *nm* to 150 *nm* [19]. While a number of suitable methods have been developed for the synthesis of magnetic nanoparticles of different compositions, successful application of such particles in the aforementioned areas are highly dependent on their stability under a variety of different conditions. The MN perform better, as regards the intended applications, when their size is below a critical value, which depends on the material, but is typically around $10 - 20$ *nm* [20]. Then, each particle becomes a single magnetic domain and shows a superparamagnetic behavior for a sufficient high temperature, namely, the blocking temperature [1]. An interesting application of MN occurs in ferrofluids [Fig. 1.3(d)], which are colloidal systems where the solute is composed of

---

[1] Heating a ferromagnetic material will make it paramagnetic in a sufficiently high temperature. By cooling and magnetizing, the ferromagnetic property is recovered, indicating superparamagnetism. The transition temperature at which this occurs is called *the blocking temperature*.

ferromagnetic nanoparticles (FN), normally magnetite (Fe_3O_4), and usually dissolved in an organic fluid. FN are particles with permanent magnetic dipole moment whose structural behavior is mainly ruled by the dipolar interaction, leading to a variety of self-assembled structures, such as rings, chains, crystal lattices, worm-like, among others. In Fig. 1.6 is illustrated a ferromagnetic dispersion without an external magnetic field [Fig. 1.6(a)] and under the presence of an uniform magnetic field [Fig. 1.6(b)][21].

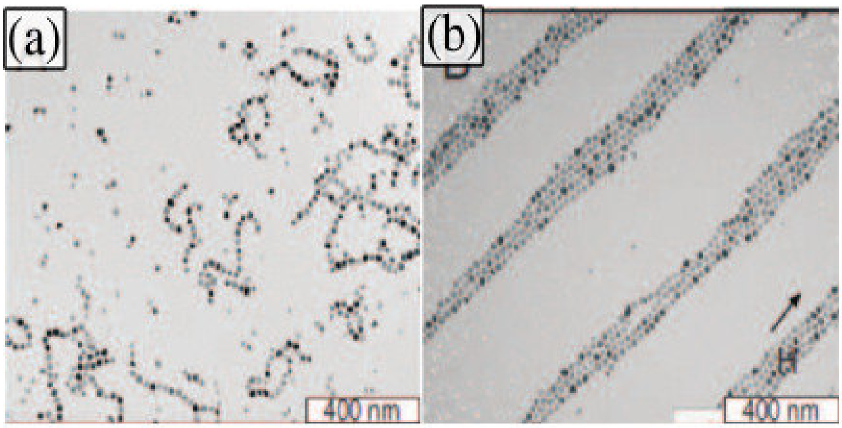

Figure 1.6: *In situ* image by Transmission Electron Microscopy (TEM) of dispersion of Fe_3O_4 in $C_{10}H_{18}$ (a) without magnetic field (b) with homogeneous magnetic field ($0.2\,T$). The transition occurs for equally spaced column that displays hexagonal symmetry. Figure extracted from Ref. [21].

Beyond the interest in study systems with such anisotropic interaction, same attention is also addressed to the particles with anisotropic shapes. Rod-like particles are a prominent example of such systems. In this thesis we focus our study on magnetic rods, which is the subject of the following section.

1.2.3 Magnetic Rods

Many efforts are currently being devoted to the synthesis and characterization of magnetic particles with anisotropic shape, e.g., rod-like particles. Within this area of research, rod-like particles play an important role as active microrheology probes, since it is possible, by the torque provided by an uniform magnetic field, to enhance the visualization of their viscoelastic properties [22, 23]. Other successful applications of magnetic rods are: (i) as components in micromechanical units [24, 25, 26], i.e., to generate localized particle trapping and stirring; (ii) as microscale propellers [27, 28, 29], i.e., magnetic units able to be remotely driven or guided in a fluid medium, and thus to potentially move and transport chemical or biological cargos in small channels or pores. Beyond the aforementioned applications, it has already been reported that particles with anisotropic shape show distinguished properties when compared to those of ferrofluids consisting of spherical particles, namely, magnetic birefringence [30] and thermal conductivity [31]. Recently, iron oxide nanorods were found to have potential for biomedical applications [32]. Colloidal rings and ribbons can be obtained from magnetic manipulation of Janus nanorods [33] and ferromagnetic ellipsoids [34]. The anisotropic shape allows, by definition, a wide variety of structures and self-assembled patterns [35] (see Fig. 1.2.3). Compared with the individual magnetic particles, the collective behavior of rod-like particles is much less understood. Alvarez and Klapp [36], in a recent paper, analyzed the structure formation of a special class of rods by computer simulations using the Monte Carlo method. They quote the possibility of simulate such systems using a special class of magnetic nanorods (MNR) consisting of dipolar beads which are permanently linked to each other composing a stiff chain with internal head-to-tail alignment of the dipole moment (see Fig. 1.8). The first approach shown in Fig. 1.8(a) is based on recent experiments by Birringer *et al.* [37]. The authors performed a field assisted deposition technique to produce magnetic rods made of iron oxide beads aligned as illustrated in Fig. 1.9.

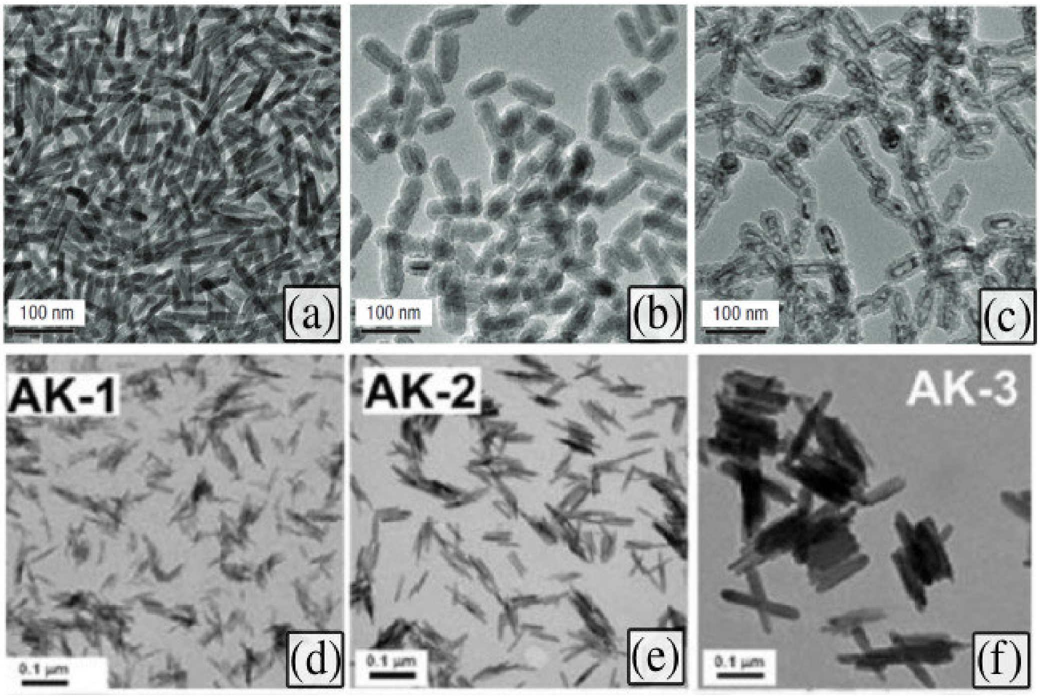

Figure 1.7: TEM images of dispersion of magnetic rods. (a) β-FeOOH nanoparticles. (b) Silica-coated β-FeOOH nanoparticles. (c) Iron oxide/silica nanocomposite after calcination at 500° C for 5h. Figure extracted from Ref. [32].(d)-(e)-(f) TEM micrographs of the nanorods (45 to 450 nm). Figure extracted from Ref. [35].

The direction of the magnetic dipole is not necessarily the same to the long axis of the magnetic rod. Anisotropic particles with a permanent tranverse magnetic dipole were studied experimentally in a recent studies [38, 34, 39]. In Fig. 1.10, we show a Field-Emission Scanning Electron Microscope (FESEM) image of peanut-shaped particles with a transverse dipole.

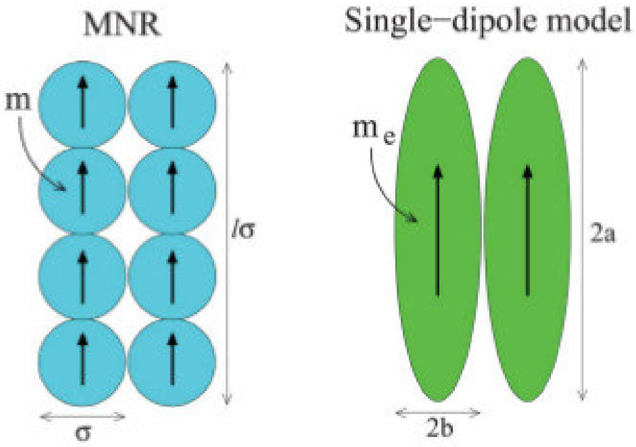

Figure 1.8: Two possible approaches to simulate nanorods: (a) MNR approach, where each particle has a diameter σ and dipole moment m, the lenght of each rod is $l\sigma$. (b) Spheroids with dipole moment m_e for minor radius b and the major radius a. Figure extracted from Ref. [36].

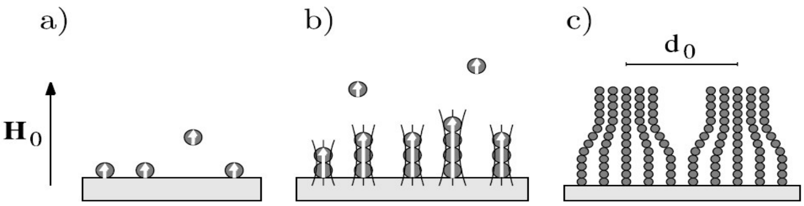

Figure 1.9: Schematic representation of the experimental rods synthesis procedure. (a) The magnetic dipole moment (white arrows) are aligned to an external field H_0 during deposition. (b) Magnetic field assisted self-assembly of individual dipolar rods. The build-up of field gradients is symbolized by flux-lines. (c) Further growth of individual rods is accompanied by a change in growth mode resulting in the formation of bundles of rods. Figure extracted from Ref. [37].

As a matter of fact, the possibility of the manipulation of the direction of the magnetic dipole can be used as a controlling parameter to functionalize the MN through the interaction direction, i.e. by tuning the dipole moment's direction of a peapod-like rigid rod. This is experimentally realised through the synthesis of monodisperse magnetoresponsive rods of desired diameter, length, and magnetic susceptibility submitted to an external magnetic field [40](see Fig. 1.11).

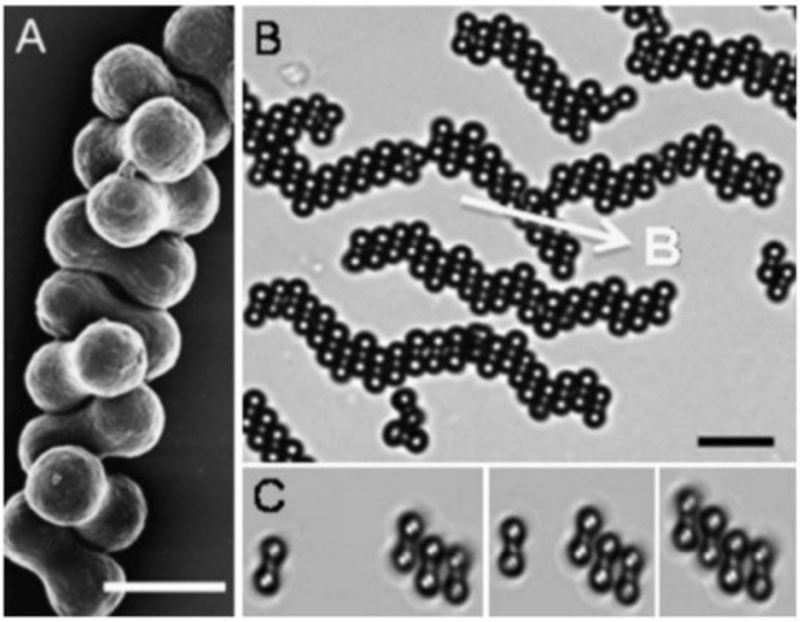

Figure 1.10: Peanut-shaped particles with a permanent transverse magnetic dipole. Figure extracted from Ref. [39].

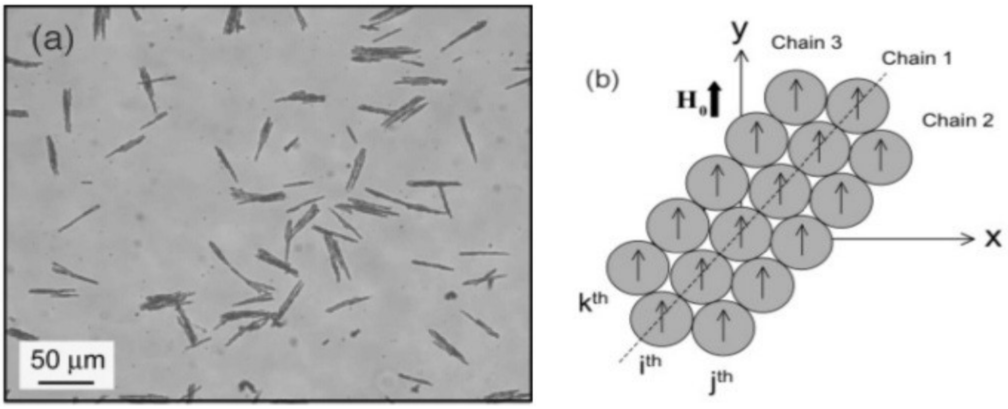

Figure 1.11: Illustration of a formation of ribbon-like chains by magnetic rods with a non-axial dipole moment. Figure extracted from Ref. [40].

1.3 Liquid Crystals-Like States

Liquid crystals (LC) are basically anisotropic molecules that display some kind of order, but not complete order. In crystals, all the particles are arranged in a crystalline lattice, so they have a perfect translational order. In the other hand, an isotropic liquid does not have any kind of translational order, it is a disordered material. LC, as the name implies, are something that are in between the two. There are different kinds of LC, perhaps the most common is called *nematic liquid crystals*. These are typically made from rod-shaped molecules, not necessarily very big. A nematic crystal has no positional order, but the molecules are oriented about a particular direction. Because of the anisotropy in the structure, these have interesting optical properties, i.e., they polarize light. This is why LC are useful for display technologies. Another type of LC is *smetic*. As the nematic phase, they have orientational order, however they also have some positional order, which is not necessarily in all directions as illustrated in Fig. 1.12(b). A smetic phase can be ordered in a particular direction but disordered in other. There is also an interesting variance of LC, which are the so-called *cholesteric liquid crystals*. In the cholesteric phase, the molecules are directionally oriented and stacked in a helical pattern, with each layer rotated at a slight angle with respect to the ones above and below it. The fundamental thing about LC is that they have orientational order but not always translational order. An important order parameter used to investigate the orientational order is the so-called nematic order parameter [41] related to the largest eigenvalue (G_2) of the following matrix:

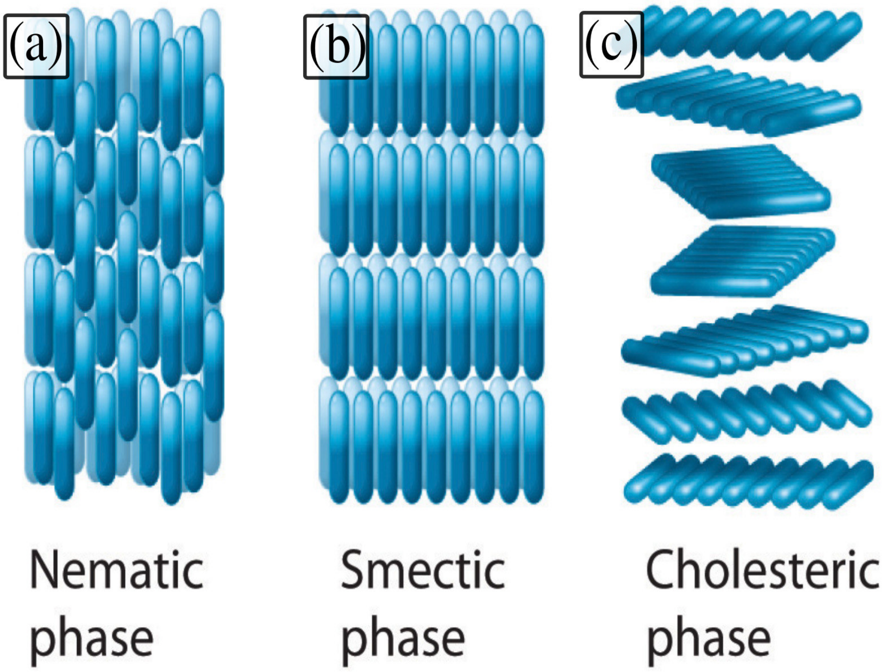

Figure 1.12: Examples of Liquid crystals.

$$\boldsymbol{Q_{kf}} = \frac{1}{2N}\sum_{i}^{N}(3\hat{\boldsymbol{s}}_k^i\hat{\boldsymbol{s}}_f^i - \delta_{kf}), \tag{1.9}$$

where i refers to particle i, the indexes k and f denote the cartesian components of the orientation vector s, N refers to the number of particles, and G_2 is 0 for isotropic phase and 1 for nematic phase.

Part II

Theoretical framework and methodology

2

Numerical Methods

The majority of the laws of nature is expressed by equations that one can hardly solve them exactly, but in very special conditions. However, it is possible to solve such equations with a good accuracy by using computers through numerical methods. For instance, much of the theoretical condensed matter physics, deals with systems consisting of many atoms and molecules. Such systems are not feasible to be studied analytically. Therefore, numerical methods applied in physical systems enables us to predict the behavior of a system before it is studied experimentally. In this chapter we will discuss the computational methods that have enabled this work. A brief but not vague description of Molecular Dynamics Simulation will be presented.

2.1 Molecular Dynamics Simulation

Molecular dynamics (MD) is a computer simulation method, based on the physical equations of motion of the atoms and molecules in the context of N-body simulation. The atoms and/or molecules are allowed to interact to each other for a period of time reproducing the particle motion. The trajectories of atoms and molecules are determined by solving numerically the Newton's equations for a system of interacting particles, where the forces between the particles and the potential energy are defined by the interatomic potentials or molecular mechanics force fields. Therefore, it is a deterministic method to simulate the physical system. The MD measurement approach is quite similar to the real experiment's. We must first prepare the sample of N particles, then we solve the Newton's equations to know their time evolution, when the system reaches the equilibrium, all the averages of interest are performed. The motion equation can be written in several ways. Perhaps one of the most fundamental form is the Lagrangian equation of motion

$$\frac{d}{dt}\left(\frac{\partial L}{\partial \dot{q}_k}\right) - \frac{\partial L}{\partial q_k} = 0, \tag{2.1}$$

where q and $\dot{q}$ are the generalized coordinates and velocities of all particles, respectively, the Lagrangian function $L(q, \dot{q})$ is defined in terms of kinetic (K) and potential (V)

energies

$$L = K - V. \tag{2.2}$$

By Legendre transformation, the Hamiltonian is obtained such as

$$H(p,q) = \sum_k \dot{q}_k p_k - L(q,\dot{q}), \tag{2.3}$$

where p_k is the generalized momentum defined by

$$p_k = \frac{\partial L}{\partial \dot{q}_k}. \tag{2.4}$$

If the Hamiltonian is a purely quadratic function of the velocities and the potential energy does not depend on the velocities, the Hamiltonian will match the system total energy

$$H = \frac{1}{2}\sum_i \frac{p_i^2}{m_i} + \sum_{i<j} V(r_{ij}), \tag{2.5}$$

where $r_{ij} = |dx\,\hat{\mathbf{x}} + dy\hat{\mathbf{y}}|$ is the interparticle distance, and p_i and m_i are the momentum and the mass of the i particle, respectively. In MD, we must take into account all the forces which all the particles are submitted. Once we know the interaction potential between the particles, we can obtain the interaction force by:

$$\mathbf{f}_{ij} = -\boldsymbol{\nabla} V. \tag{2.6}$$

The net force in particle i is calculated in terms of their components

$$f_{x_i} = -\frac{dx}{r_{ij}}\left(\frac{\partial V(r_{ij})}{\partial r}\right), \qquad f_{y_i} = -\frac{dy}{r_{ij}}\left(\frac{\partial V(r_{ij})}{\partial r}\right), \qquad f_{z_i} = -\frac{dz}{r_{ij}}\left(\frac{\partial V(r_{ij})}{\partial r}\right). \tag{2.7}$$

E.g., in the case that $V(r)$ is equal to Eq. (1.8)

$$\begin{aligned} f_x = {} & \left[3\frac{\boldsymbol{\mu}_i \cdot \boldsymbol{\mu}_j}{r_{ij}^5} - 15\frac{(\boldsymbol{\mu}_i \cdot \boldsymbol{r}_{ij})(\boldsymbol{\mu}_j \cdot \boldsymbol{r}_{ij})}{r_{ij}^7} + 48\epsilon\left(\frac{\sigma^{12}}{r_{ij}^{14}}\right)\right] dx + {} \\ & \frac{3}{r_{ij}^5}\left[\mu_{jx}(\boldsymbol{\mu}_i \cdot \boldsymbol{r}_{ij}) + \mu_{ix}(\boldsymbol{\mu}_j \cdot \boldsymbol{r}_{ij})\right], \end{aligned} \tag{2.8}$$

$$\begin{aligned} f_y = {} & \left[3\frac{\boldsymbol{\mu}_i \cdot \boldsymbol{\mu}_j}{r_{ij}^5} - 15\frac{(\boldsymbol{\mu}_i \cdot \boldsymbol{r}_{ij})(\boldsymbol{\mu}_i \cdot \boldsymbol{r}_{ij})}{r_{ij}^7} + 48\epsilon\left(\frac{\sigma^{12}}{r_{ij}^{14}}\right)\right] dy + {} \\ & \frac{3}{r_{ij}^5}\left[\mu_{ij}(\boldsymbol{\mu}_i \cdot \boldsymbol{r}_{ij}) + \mu_{iy}(\boldsymbol{\mu}_j \cdot \boldsymbol{r}_{ij})\right]. \end{aligned} \tag{2.9}$$

Therefore, the equation of motion of each particle is given by

$$m_i\left(\frac{d^2\mathbf{r}_i}{dt^2}\right) = \mathbf{F}_i = \sum_{j\neq i}^{N} \mathbf{f}_{ij}, \tag{2.10}$$

where $\mathbf{f}_{ij}$ is the force exerted on j by particle i.

For linear rigid bodies, e.g. rods, in addition to the forces, we must also take into account the torques. Considering that there are only two rotational degrees, the torque on a linear molecule can be written as a sum over a interaction sites

$$\mathbf{N} = \sum_i \mathbf{r}_i \times \mathbf{f}_i = \mathbf{s} \times \sum_i d_i \mathbf{f}_i = \mathbf{s} \times \mathbf{G}, \tag{2.11}$$

where the orientation is defined by $\mathbf{s}$, the unit vector along the molecular axis, and where d_i is the distance of each interaction site from the center of mass (CM), see Fig. 2.1. In the linear case, the angular momentum is simply $\mathbf{L} = I\boldsymbol{\omega}$, ($I$ is the rod moment of inertia and $\boldsymbol{\omega}$ is the angular velocity), so that the equations of motion to the angular case, using Eq. (2.11), are

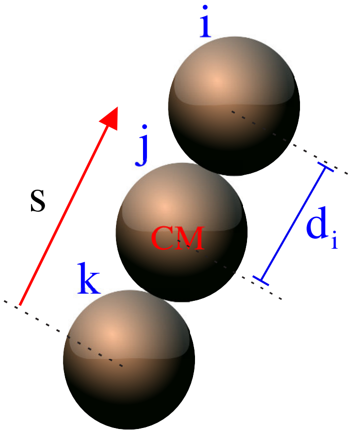

Figure 2.1: Illustration of important parameters of a linear rigid body model.

$$I\frac{d\boldsymbol{\omega}}{dt} = \mathbf{s} \times \mathbf{G}, \tag{2.12}$$

$$\frac{d\mathbf{s}}{dt} = \mathbf{u} = \boldsymbol{\omega} \times \mathbf{s}. \tag{2.13}$$

The quantity $\mathbf{u}$ is the tangential velocity, and it gives the information of how the orientation of the linear body, given by $\mathbf{s}$, is changing over time. Thus, we can obtain the tangential acceleration ($\boldsymbol{\alpha}$) by doing the derivative of Eq. (2.13) with respect to the time

$$\frac{d\mathbf{u}}{dt} = \boldsymbol{\alpha} = \frac{d\boldsymbol{\omega}}{dt} \times \mathbf{s} + \boldsymbol{\omega} \times \mathbf{u}. \tag{2.14}$$

From Eq. (2.12) we have

$$\boldsymbol{\alpha} = \frac{1}{I}(\mathbf{s} \times \mathbf{G} \times \mathbf{s}) + \boldsymbol{\omega} \times \boldsymbol{\omega} \times \mathbf{s}. \tag{2.15}$$

Using the identity of Eq. (A38), we have that

$$\begin{aligned} \boldsymbol{\alpha} &= -I^{-1}\mathbf{s}(\mathbf{G}\cdot\mathbf{s}) + I^{-1}\mathbf{G}\underbrace{(\mathbf{s}\cdot\mathbf{s})}_{1} + \boldsymbol{\omega}\underbrace{(\boldsymbol{\omega}\cdot\mathbf{s})}_{0} - \mathbf{s}\underbrace{(\boldsymbol{\omega}\cdot\boldsymbol{\omega})}_{\omega^2}, & (2.16) \\ &= I^{-1}\left(-\mathbf{s}(\mathbf{G}\cdot\mathbf{s}) + \mathbf{G}\right) - \mathbf{s}\omega^2, & (2.17) \end{aligned}$$

as $\boldsymbol{\omega}$ is perpendicular to $\mathbf{s}$ so, $\boldsymbol{\omega}\cdot\mathbf{s}=0$. Doing the dot product of $\mathbf{s}$ and $(-\mathbf{s}(\mathbf{G}\cdot\mathbf{s})+\mathbf{G})$, we can see that they are perpendicular to each other. So we can say that : $\mathbf{G}_\perp = (-\mathbf{s}(\mathbf{G}\cdot\mathbf{s})+\mathbf{G})$. For linear rods in a plane, $\boldsymbol{\omega}=\omega\hat{\mathbf{z}}$ and $\mathbf{s}=s_x\hat{\mathbf{x}}+s_y\hat{\mathbf{y}}$, then

$$\begin{aligned}\mathbf{u}\cdot\mathbf{u} &= (\boldsymbol{\omega}\times\mathbf{s})\cdot(\boldsymbol{\omega}\times\mathbf{s}),\\ &= \left[\omega\hat{z}\times(s_x\hat{x}+s_y\hat{y})\right]\cdot\left[\omega\hat{z}\times(s_x\hat{x}+s_y\hat{y})\right],\\ &= \omega^2 s_x^2+\omega^2 s_y^2=\omega^2\underbrace{(s_x^2+s_y^2)}_{1}=\omega^2. \qquad (2.18)\end{aligned}$$

Thus, using Eq. (2.17), the tangential acceleration for a linear rod in two-dimensions

$$\boldsymbol{\alpha}=I^{-1}\mathbf{G}_\perp-\mathbf{s}(\mathbf{u}\cdot\mathbf{u}). \qquad (2.19)$$

2.1.1 Integration of The Equations of Motion

To integrate the equations of motion numerically, we will use the so-called Verlet-Scheme [8, 43], which we will focus on the Leapfrog method and the velocity Verlet method. Despite its low order, the Leapfrog method has excellent energy conservation properties and it is widely used. It is equivalent to Verlet Method [44]. The derivation of the Leapfrog method follows immediately from the Taylor expansion [45] of the coordinate variable - $\mathbf{r}(t)$

$$\mathbf{r}(t+\delta t)=\mathbf{r}(t)+\mathbf{v}(t)\delta t+(\delta t^2/2)\frac{\mathbf{f}(t)}{m}+O(\delta t^3), \qquad (2.20)$$

where $\mathbf{f}(t)$ is the force and m is the mass of the particle. We can rewrite Eq. (2.20) by

$$\mathbf{r}(t+\delta t)=\mathbf{r}(t)+\delta t\left[\mathbf{v}(t)+(\delta t/2)\frac{\mathbf{f}(t)}{m}\right]+O(\delta t^3). \qquad (2.21)$$

The term multiplying δt is just the Taylor expansion of $\mathbf{v}(t+\delta t/2)$, and the truncation error is on the order of $O(\delta t^3)$. Similarly, if we subtract the Taylor expansion of $\mathbf{v}(t-\delta t/2)$ from the corresponding expression for $\mathbf{v}(t+\delta t/2)$ we have the complete integration leapfrog scheme

$$\mathbf{v}(t+\delta t/2)=\mathbf{v}(t-\delta t/2)+\frac{\mathbf{f}(t)}{m}\delta t, \qquad (2.22)$$

$$\mathbf{r}(t+\delta t)=\mathbf{r}(t)+\mathbf{v}(t+\delta t/2)\delta t. \qquad (2.23)$$

The velocities and coordinates are evaluated at different times, but it does not denote a problem. In order to evaluate the instantaneous kinetic energy, we need the instantaneous velocity $\mathbf{v}(t)$, for this purpose we perform as the following equation

$$\mathbf{v}(t)=\frac{1}{2}\left(\mathbf{v}(t+\delta t/2)+\mathbf{v}(t-\delta t/2)\right). \qquad (2.24)$$

For the angular motion, we have similar equations from Eqs. (2.22) and (2.23), thus

$$\mathbf{u}(t+\delta t/2)=\mathbf{u}(t-\delta t/2)+\boldsymbol{\alpha}(t)\delta t, \qquad (2.25)$$

$$\mathbf{s}(t+\delta t)=\mathbf{s}(t)+\mathbf{u}(t+\delta t/2)\delta t. \qquad (2.26)$$

From Eq. (2.25) we obtain

$$\mathbf{u}(t-\delta t/2) = \mathbf{u}(t) - \frac{\delta t}{2}\boldsymbol{\alpha}(t). \tag{2.27}$$

We can obtain the relation $u(t) \cdot u(t)$ needed from Eq. (2.19) by doing the dot product of $\mathbf{s}(t)$ in both sides of Eq. (2.27) we have

$$\begin{aligned}
\mathbf{s}(t)\cdot\mathbf{u}(t-\delta t/2) &= \mathbf{s}(t)\cdot\mathbf{u}(t) - \mathbf{s}(t)\cdot\left\{I^{-1}\mathbf{G}_\perp(t) - \mathbf{s}(t)\left[\mathbf{u}(t)\cdot\mathbf{u}(t)\right]\right\}\frac{\delta t}{2}, \\
&= -\left(\mathbf{u}(t)\cdot\mathbf{u}(t)\right)\frac{\delta t}{2}, \\
\mathbf{u}(t)\cdot\mathbf{u}(t) &= -\frac{2}{\delta t}\mathbf{s}(t)\cdot\mathbf{u}(t-\delta t/2), \qquad (2.28)
\end{aligned}$$

where we used $\mathbf{s}(t)\cdot\mathbf{s}(t) = 1$, $\mathbf{s}(t)\cdot\mathbf{u}(t) = 0$ and $\mathbf{s}(t)\cdot\mathbf{G}_\perp(t) = 0$.

However, it is possible to cast an integration scheme which evaluates the positions and the velocities at the same instant of time. The so-called velocity Verlet algorithm also can be derived from a Taylor expansion

$$\mathbf{r}(t+\delta t) = \mathbf{r}(t) + \mathbf{v}(t)\delta t + \frac{\mathbf{f}(t)}{2m}\delta t^2, \tag{2.29}$$

$$\mathbf{s}(t+\delta t) = \mathbf{s}(t) + \mathbf{u}(t)\delta t + \boldsymbol{\alpha}(t)\delta t^2. \tag{2.30}$$

The update of the velocities is given by

$$\mathbf{v}(t+\delta t) = \mathbf{v}(t) + \frac{\mathbf{f}(t)+\mathbf{f}(t+\delta t)}{2m}\delta t, \tag{2.31}$$

$$\mathbf{u}(t+\delta t) = \mathbf{u}(t) + \frac{\boldsymbol{\alpha}(t+\delta t)+\boldsymbol{\alpha}(t)}{2}\delta t. \tag{2.32}$$

Eliminating the velocities in these equations will trace back to the original Verlet algorithm [43], so the original and the velocity version are completely equivalent. To calculate the trajectories and the orientations, the Eqs. (2.29) - (2.32) are processed gradually by the simulation program. Compared to other integrators with only one force evaluation like the Euler method with error on the order δt^2, the numerical stability of the Verlet algorithm is much higher and the errors are of order δt^2. From a physical point of view the time reversibility is very important.

2.1.2 Periodic Boundary Conditions

Despite the rise of computing power since adoption of the MD simulation method, the simulations are still usually performed for a small number of particles. Most simulations for this work were done on systems with a little bit more of 2500 particles. Simulations with more particles were only done as a check for finite size effects. The reason for the small number of particles is not the lack of memory of computers, it is rather the computational power spent on evaluating the forces between the particles which is proportional to N^2, which it can be decreased by special techniques not discussed in this thesis, further information in Refs. [46, 47]. Because we are interested in bulk phases properties, it is not satisfactory to simulate the system as a closed box. In such a simulation box of a system of 1000 particles, arranged on a simple squared lattice, a not-neglected amount of particles are in contact with the surface of the box. These particles will experience quite different forces as particles inside the bulk. This problem can be overcome by implementing *periodic boundary conditions* (PBC). The small system of particles is expanded to infinity by surrounding the central simulation box with identical copies till an infinite space-filling array is obtained. It works as if the sample is simulated as a small piece within a larger portion of the same material. So if the particles leave the central simulation box, an image of their own will re-enter it directly through the opposite face. That is, if a particle in the integration step, leaves the simulation box through its right end by a distance δx, e.g., it will be replaced at a distance δx to the right from the left end of the box, while the positions of the other particles are held. The same goes for the interactions, as a direct consequence of periodic boundary conditions is the *minimum image convention* first used by Metropolis et al. in Monte Carlo (MC) simulations [48]. If all interactions between a central particle and the other particles in the box should be calculated in periodic systems, we have to take into account that some copies of particles are closer to the central one, than the particle itself. Once the particles are in the rightmost edge, e.g., they interact with the others as they are in the left extreme of the box as though they are in a box which is immediately to the left of the first one. This idea is extended to $3D$ systems.

A two-dimensional system subjected to PBC is illustrated in Fig. 2.2. There are several boxes with length L, identical to the central one, periodically distributed around that. If a particle is located at r_i relative to the center of the main box, then the system will also recognize a set of *ghost particles* with locations given by $r_i + nL$, where $n \in \mathbf{Z}$, so the potential energy is given by

$$U(r_i, ..., r_N) = \sum_{i<j} u(r_{ij}) + \sum_{n} \sum_{i<j} u(\mid r_{ij} + nL \mid). \tag{2.33}$$

The expression above presents a problem for systems with long-range interactions[1], e.g., Coulomb interactions, because, in this case, Eq. (2.33) diverges. In terms of simulation for this type of system, we must use a technique to truncate the system energy. Among several methods, *Ewald Sum* [42] is the one of the most used. For systems with short-range interaction, we just need to worry about limiting the interactions of the particles that are within a region whose radius is called the *cutoff radius*. In general, the cutoff radius would be the distance which the interaction energy is very small, so that we can neglect the interactions of particles whose distance is greater than this cutoff range. In order the cutoff radius concept to work properly, one defines the size of the box as the double cutoff radius. Thus, the distance between a particle and its image will not be less than half of the size of the box. We are not going to go into the details of long-range

---

[1] It is said long-range interaction when the potential has the asymptotic behavior of the type $r^{-\nu}$ where ν is less than or equal to the dimension of the system [41].

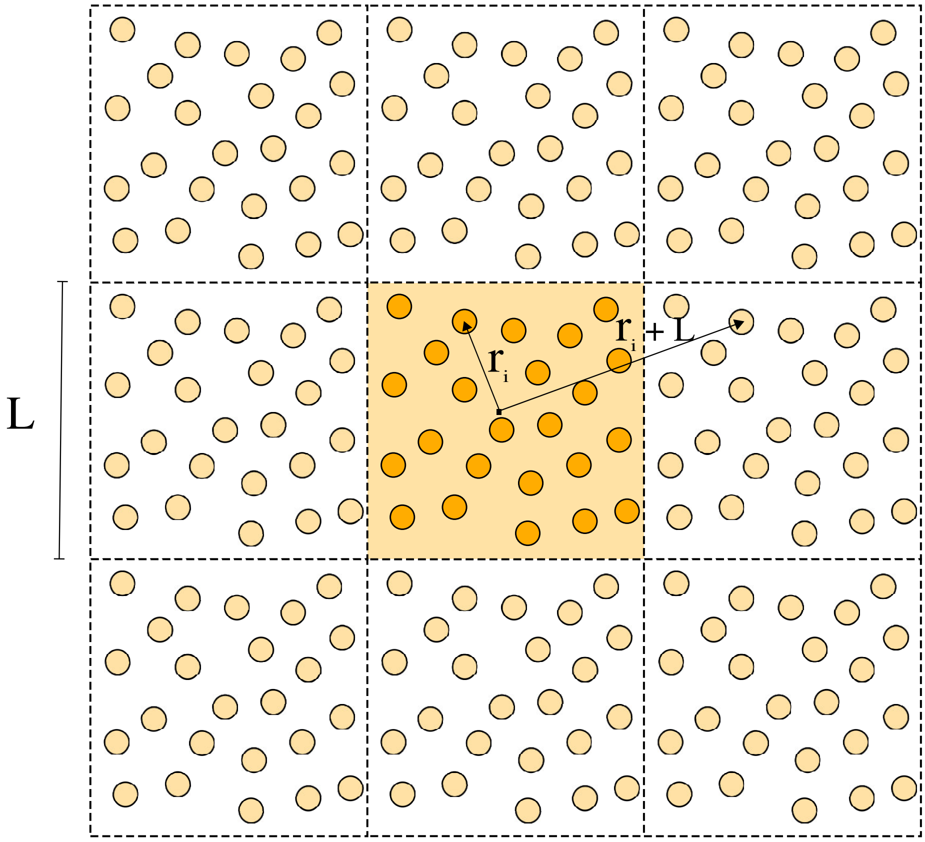

Figure 2.2: Illustration of a 2D system subject to PBC. The yellow-shaded box represents the central (real) simulation box.

technique because in the $2D$ case, the dipolar pair interaction falls off fast (r^{-3}) and therefore it is sufficient to take the simulation box sufficiently large such that no special long-range summation techniques is necessary.

2.1.3 Statistical Mechanics and Molecular Dynamics

MD simulations provide knowledge of the classical microscopic states of the system. Every microstate is represented by a particular point in phase space corresponding to a full set of generalized coordinates q_j and conjugate momenta p_j, $\Gamma = (q_1, ..., q_{6N}, p_1, ..., p_{6N})$ composing a multidimensional space (see Fig. 2.3). A set of points Γ in the phase space is the *ensemble*. When we perform a computer simulation, we often want some system information at macroscopic level such as: pressure, internal energy, specific heat, etc. Therefore we need to draw on the *Statistical Physics* to convert the microscopic level information obtained by the simulation such as molecular or atomic positions and velocities. In statistical mechanics, one is mainly interested in systems where the number of degrees of freedom is large, a macroscopic quantity A, depending on the microstate Γ,

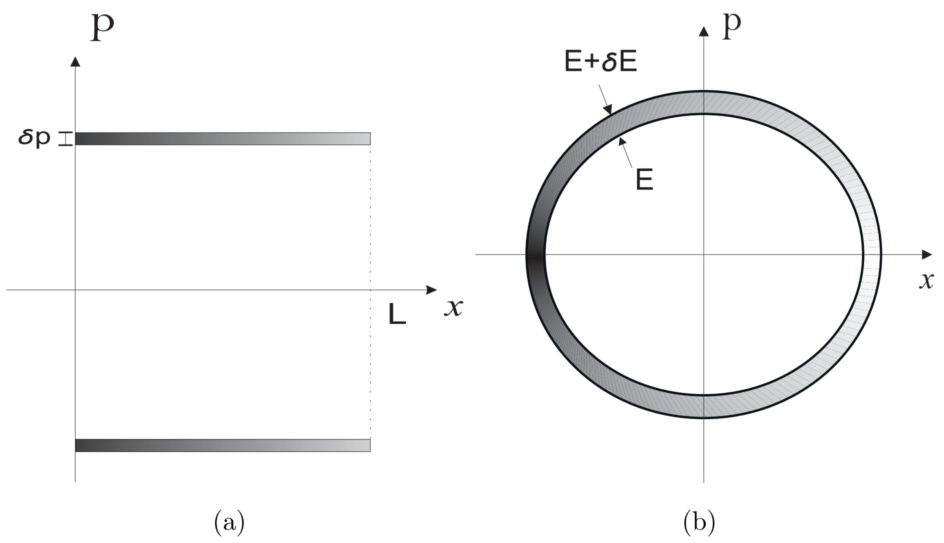

Figure 2.3: Some examples of classic phase spaces - (a) Phase space of a free particle for $0 < x < L$ and $p, p + \delta p$ - (b) Phase space for harmonic oscillator with energy $E, E + \delta E$

is given by the ensemble average [49, 50]

$$\langle A \rangle = \frac{\int A(\Gamma)\rho(\Gamma)d\Gamma}{\int \rho(\Gamma)d\Gamma}, \tag{2.34}$$

where $\rho(\Gamma)$ is the phase density. From a single system configuration/snapshot produced by molecular dynamics simulation we can determine the instantaneous value $A(\Gamma)$. With running simulation the system evolves in time, so that a trajectory in phase space $\Gamma(t)$ is produced and $A(\Gamma(t))$ will change. To measure the observable macroscopic property A_{obs} from simulation, we determine the time average over a definite time period t_{obs}

$$A_{obs} = < A(\Gamma(t)) > = \lim_{t_{obs} \to \infty} \frac{1}{t_{obs}} \int_0^{t_{obs}} A(\Gamma(t))dt. \tag{2.35}$$

In general, time averaging should be done over infinite times to get macroscopic quantities, but in practice this might be satisfied with long enough finite times t_{obs}. Since MD simulation does not provide continuous time development of the system, we have to sum the instantaneous values of A at integer multiples of the time step δt. For instance, in the canonical ensemble (NVT), where the number of particles, volume and temperature are conserved, the ensemble average (in equilibrium) of A can be expressed in terms of phase space integrals taking into account the total potential energy of the system, $U = U(\mathbf{r}^N)$, as

$$\langle A \rangle = \frac{\int A(\mathbf{r}^N) \exp^{-\beta U(\mathbf{r}^N)} d\mathbf{r}^N}{\int \exp^{-\beta U(\mathbf{r}^N)} d\mathbf{r}^N}, \tag{2.36}$$

where $\mathbf{r}^N$ is the set of coordinates, $Z = \int \exp^{-\beta U(\mathbf{r}^N)} d\mathbf{r}^N$ is the partition function. This average corresponds to a series of measurements over an ensemble of independent systems. The ensemble average consists in analyzing the state of all microsystems constituents (all points Γ), in the same instant of time, and make an average of all these states. So, it is important to know the distribution of the points Γ in phase space. The *Liouville theorem* [41] ensures that the distribution function of the phase space is constant over time. As a result, if there is a trajectory in the phase space that goes through all the points of it, so that $\rho_{ens} \neq 0$, then, each system will eventually visit all states. Such a system is called *ergodic*. This ensures the possibility of replacing the time average to an ensemble average. Therefore, the MD method is based on the assumption that the ergodic principle holds, and then the time that a particle spends in a given region of the phase space is proportional to the volume of this region. In other words, the ergodic principle states that all the accessible microstates are equally likely for the limit $t \to \infty$. Consequently, the temporal average obtained in a MD run should be, in principle, the same as the ensemble average, i.e.

$$A_{obs} = \frac{1}{M} \sum_{i=1}^{M} A_i(\mathbf{r}^N) = \langle A \rangle, \tag{2.37}$$

where M is the total number of measurements for independent runs.

In general the ergodicity of a system has always to be proved for a definite set of parameters, but this is hard to do. In MD ergodicity is often destroyed by metastable states trapping the system for extended periods of time. This problem can be avoided by comparing averages of observables from different simulations with the same simulation parameters, but different initial configurations. Even in this case one cannot be sure, however, to reach every region in phase space.

2.1.4 Molecular Dynamics Scheme

A typical MD simulation run consists of the following basic steps:

1. Initialization of the system, i.e., assign initial coordinates and initial velocities for all the particles in the system;

2. Calculation of the interaction force between pairs of particles. This is the most time-consuming part of any MD simulation;

3. Numerical integration of the equation of motion by using a suitable scheme i.e., velocitity Verlet, leapfrog algorithm;

4. Apply the periodic boundary conditions, if necessary.

These are all done in one single time-step. If m is the total number of time-steps in the simulation, then $t_{tot} = m\delta t$ is the total time of the simulation run, and δt is the discrete time interval between time-steps. After a given number of simulation steps, the system should, in principle, attain an equilibrium state. In order to check that the system has indeed reached an equilibrium situation, one could, for instance, calculate the total energy of the system (total potential energy per particle plus the total kinetic energy per particle) over time and check if it has reached a stationary value, i.e., constant over time. The number of time-steps in order the system to reach this equilibrium situation depends on each problem specifically, therefore a careful analysis should be done for each particular case. The time interval between the beginning of the simulation and the equilibrium state is usually called the thermalization procedure. Only after the thermalization procedure one should calculate physical properties of interest, either structural properties (e.g., radial distribution function (RDF)) or dynamical properties (e.g., mean square displacement (MSD) and velocity autocorrelation function (VACF)).

2.1.5 Control of Temperature

One of the concerns when one performs MD simulation is to bring the system to the desired temperature as the system is in contact to a thermal reservoir. One of the most known controlling method is based on the rescaling of the velocities ($\mathbf{v}$ and $\mathbf{u}$). The advantage of integration methods aforementioned is the possibility of adjusting the velocities of the particles straightforwardly according to the nominal temperature T_0 of the thermal reservoir

$$\mathbf{v}(t+\delta t/2) = \sqrt{\frac{T_0}{T(t)}}\mathbf{v}(t-\delta t/2) + \frac{\mathbf{f}(t)}{m}\delta t, \tag{2.38}$$

where $T(t)$ is the temperature at time (or step) t, this property is calculated based on the energy equipartition theorem, where each degree of freedom of the system contributes with $k_B T/2$ for the total energy. So, the instantaneous temperature is given by

$$T(t) = \sum_{i=1}^{N} \frac{m_i v_{\alpha,i}^2(t)}{N k_B}, \tag{2.39}$$

where $v_{\alpha,i}$ is the α component of the velocity of i-th particle of a system with N particles.

In order to allow fluctuations of the kinetic energy, we can make the system to be weakly coupled to the heat bath. For this, a further refinement of the velocity rescaling approach has been proposed by Berendsen [51], at each time step, velocities are scaled by a factor

$$\chi = \left(1 + \frac{\delta t}{\tau}\left(\frac{T(t)}{T_0} - 1\right)\right)^{-1/2}, \tag{2.40}$$

where δt is the time step, and τ is a constant called the “rise time” of the thermostat. It describes the strength of the coupling of the system to a hypothetical heat bath. The larger τ, the weaker the coupling. This method does not generate states in the canonical ensemble, but it seems to be very useful for purposes of changing state and equilibrating a system at the new temperature. A several methods was proposed to reproduce a NVT ensemble, prominent examples are: Andersen thermostat [52], Nosé-Hoover thermostat [53] and Langevin thermostat [54, 55]. The latter we will discuss in more details in the following sections.

2.1.6 Important Measured Quantities

♦ Pair correlation function

A measurement for the structure of matter is the radial pair distribution function $g(r)$, dependent only on the pair separation r for a translational invariant system of identical particles. It gives the probability of finding a pair of particles a distance r apart, relative to the probability expected for a completely random distribution for the same density. We get the radial pair distribution function by the definition [8]

$$g(r) = \frac{V}{N^2} \left\langle \sum_i \sum_{j \neq i} \delta(r - r_{ij}) \right\rangle , \tag{2.41}$$

where V is volume, N is the number of particles, r_{ij} is the i and j particles separation, and $\langle ... \rangle$ stands for an average over the realizations. From the point of view of statistical mechanics, where usually the number of degrees of freedom is large, the function represents an important physical measure to characterize structural properties of molecular systems, e.g., liquids, glasses and super-cooled liquids, etc. As $r_{ij} = r_{ji}$, which makes the Eq. (2.41) to be reduced to

$$g(r) = \frac{2V}{N^2} \left\langle \sum_i \sum_{j < i} \delta(r - r_{ij}) \right\rangle . \tag{2.42}$$

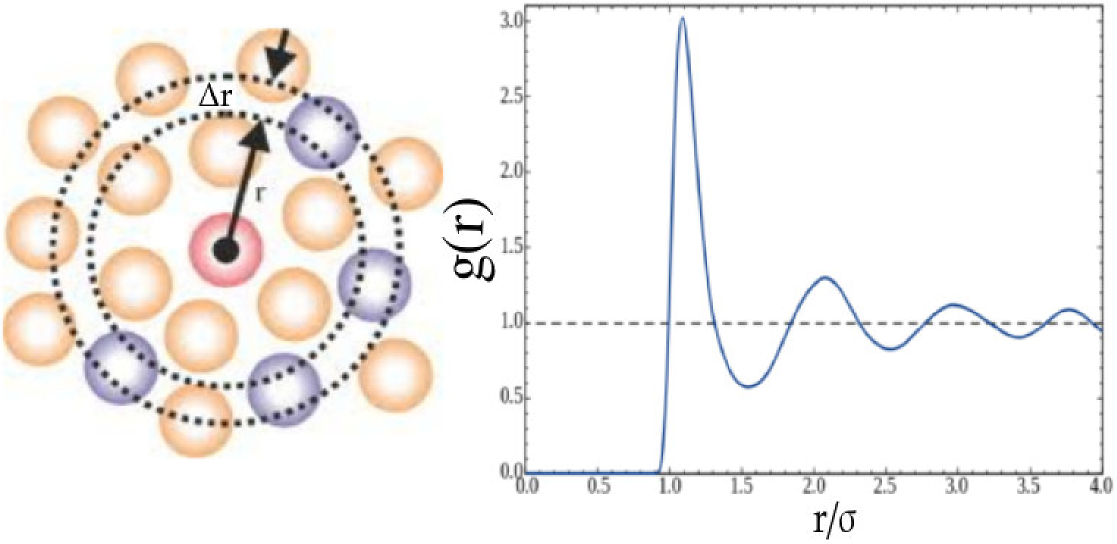

Figure 2.4: Illustration of evaluation of the pair correlation function. (a) In the center there is a reference particle (pink circle). The spheres around represent other particles in the system. A centered ring is drawn as reference and it has radius r, relative to the reference particle, and width Δr. (b) As an example, we show the typical radial distribution function for a LJ system in the liquid phase. Modified from Refs. [56, 57].

As $\rho = N/V$ (N/A), for $3D$ $(2D)$, and considering it constant, we get to, after a both sides integration

$$\rho \int g(r)dr = \frac{2}{N} \int \left\langle \sum_{i} \sum_{j<i} \delta(r - r_{ij}) \right\rangle = N - 1, \tag{2.43}$$

which is the result of counting the number of remaining particles around a chosen particle at the origin.

In terms of simulation, Eq. (2.42) is evaluated as a histogram in order to count the number of particles in a given shell of radius Δr, which is at a distance r from the reference (origin) particle (see Fig. 2.4). For a $2D$ system, consider h_n the number of pairs of atoms (i, j) with the condition $(n-1)\Delta r \leq r_{ij} < n\Delta r$. By counting the pair of atoms in the shell Δr, one would get [8]

$$\mathbf{g}(r_n) = \frac{h_n}{\pi r_n \rho \Delta r}, \tag{2.44}$$

where $r_n = (n - 1/2)\Delta r$ and n is the index of the each bin of the histogram.

♦ Clustering properties

Cluster formation is a very important subject of self-assembled systems, because is a real physical process and some models exhibit special properties to clusters. In MD simulations, it is important to be able to identify conditions which particles belong to a same cluster. Often it is used an energy criteria which considers two particles bonded when there is a attraction interaction between two particles. Another alternative method requires less computation effort based on the interparticle distance. The latter condition considers two particles bonded, let us say i and j, if their separation $r_{ij} < \delta_c$, where δ_c is the critical separation for two particles to be considered bonded. The value of δ_c is typically based on energy conditions.

There are basically some quantities that help us to analyze the clustering properties. The so-called polymerization [58] evaluates the tendency of the system to form clusters and it is defined by

$$\Phi = \left\langle \frac{N_c}{N} \right\rangle, \tag{2.45}$$

where N_c is the number of clustered particles and N is the total number of particles. When $\Phi = 1$ every particle belongs to a cluster, not necessarily the same. For $\Phi = 0$, in another hand, it stands for a monomer phase. Another important quantity is the cluster size distribution $n(s)$ (see Fig. 2.5). It is an important tool to identify percolated structures since right at the percolation threshold, the cluster size distribution of an infinite system shows a power-law decay $n(s) \sim s^{-\tau}$, where τ is the so-called Fisher exponent that assumes specific values for characteristic systems close to percolation transition, i.e, $\tau \propto -187/91$ [59] for random percolated $2D$ structures.

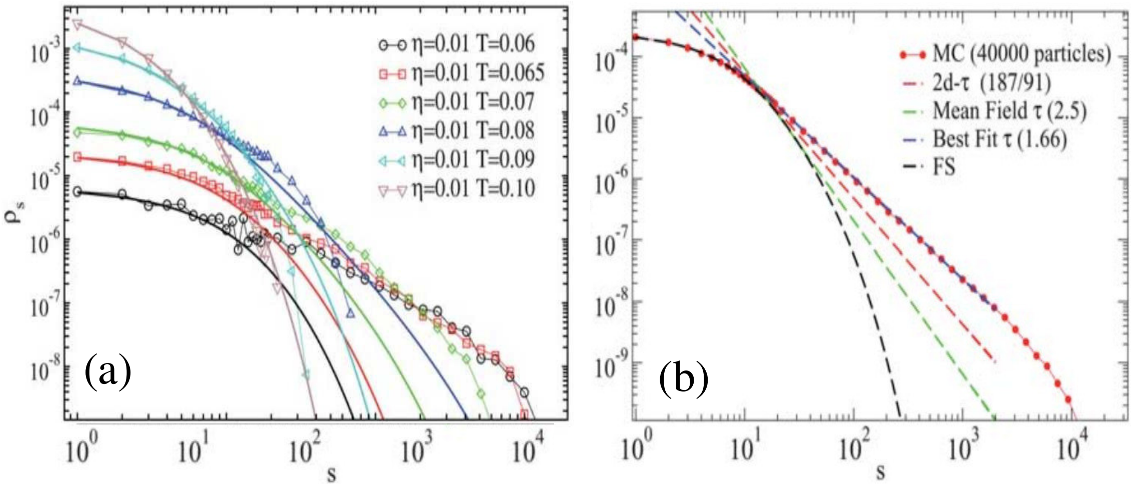

Figure 2.5: (a) Cluster size distribution for packing fraction $\eta = 0.01$ (ratio of the occupied area over the available area) at several temperatures; (b) Cluster size distribution close to percolation ($T = 0.078$ and density $\rho = 0.1$). To minimize size effects, 40000 particles have been simulated. The different straight lines show the theoretical predictions for mean-field and 2d-percolation, as well as the best fitting slope of the numerical cluster distribution. The cluster size predicted by the Flory–Stockmayer (FS) theory [60] is also reported, but its range of validity is limited to only small clusters. $\rho(s)$ stands for the frequency of appearance of s-sized cluster. Extracted from Ref. [61].

♦ Percolation properties

Percolation is another important connectivity property defined as a geometrical transition, in which interacting units such as the particle in a fluid, the spins on a lattice, or the nodes of a network spontaneously form system-spanning clusters termed the "percolated phase" [62]. In contrast, the units are distributed homogeneously or form isolated clusters of finite size in the non-percolated phase. More recent(experimental and theoretical) research on continuous percolation often involves colloidal suspensions. One important topic in this area concerns the percolation of rod-like colloids (see Fig. 2.6), From an applicational point of view the underlying idea is that the percolated network leads to lightweight materials with strongly enhanced mechanical stability and electrical (and/or thermal) conductivity. Another main topic, which concerns particularly complex colloidal mixtures [64, 65] and colloids with directional interactions [66, 67, 68], is the intimate relation between percolation and the formation of a physical gel, which is a state in which particles are connected via bonds of limited lifetime. It is now well established that such colloidal gels, which are characterized through a very specific dynamic behavior, can form at extremely low packing fractions. Note, however, that gelation is a phenomenon which normally occurs for very strong coupling conditions, i.e., at temperatures far below those related to the vapor-liquid critical point (if the latter exists at all).

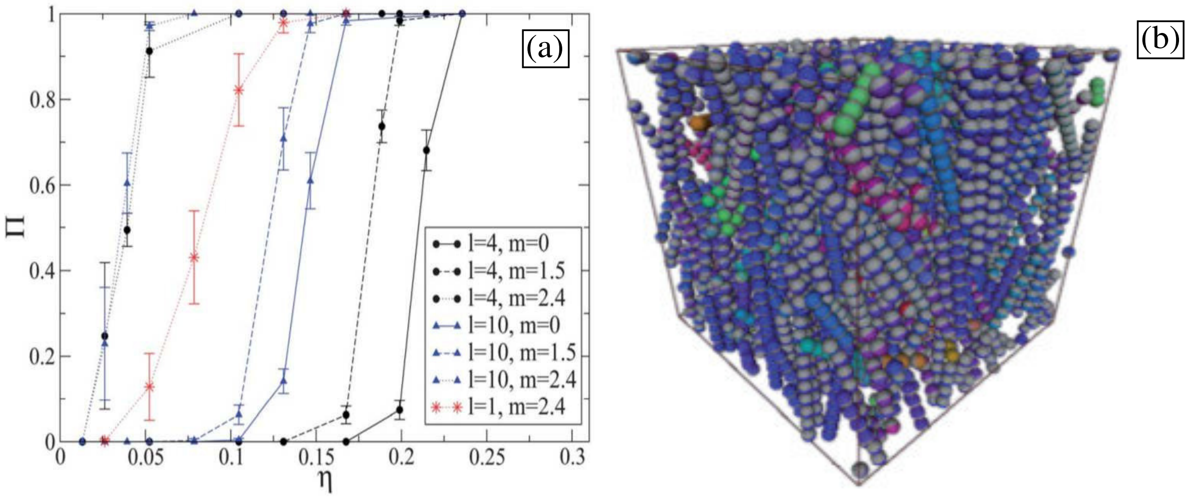

Figure 2.6: (a) Percolation probability as a function of the volume fraction for different aspect ratio (l) and dipole moment (m). (b) Example of a $3D$-percolated cluster system of nanorods. Extracted from Ref. [36].

Percolation on continuous systems was originally discussed as a phenomenon in the context of flow through a porous media, however the statistical theory of percolation has been used to understand the critical behavior of fluids. Percolation is defined according to the conventional method when at least 50% of the sampled configurations in the simulation trajectory contain a system-spanning cluster, i.e., the percolation probability is evaluated by counting the number of appearances of a cluster which spans over the system in a such way it is possible to make a continuum path through any sequence of bonds and any two opposite edges that limit the system. Under these circumstances, the cluster is effectively infinite when applying periodic boundary conditions. Typical percolating fluids exhibit a single peak in the cluster distribution comparable to the system size and these states are denoted as random percolated (see Fig. 2.7).

The spanning cluster probability depends on many factors such as the kind of percolation (site or bond), type of lattice, boundary conditions, etc. In MD simulation, one always deals with a finite lattice. Because of that, one way to check the infinite cluster appearance is to check the largest clusters size. However, for the largest cluster size distribution, the calculations will include all the configurations whether the lattice spans or not. The largest cluster, in fact, enjoys a double role in sense that it may or may not happen to be the spanning cluster. The probability of smaller clusters being the spanning one is relatively much smaller. Even when the lattice is spanned, the largest cluster may or may not be the spanning one. For finite and interacting systems, when transient bonds are present, a very useful order parameter is the fraction of monomers in the largest cluster [69, 70].

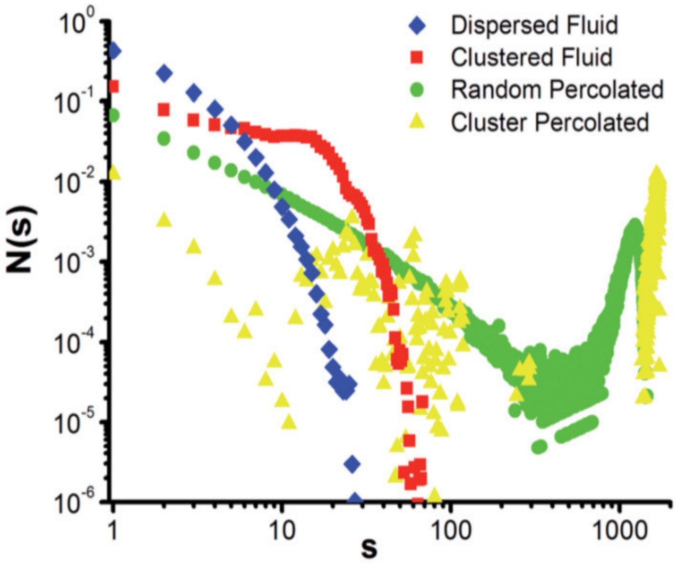

Figure 2.7: Cluster size distribution for a short range attraction and long range repulsion system showing four possibles states. The dispersed fluid is mainly represented by monomers. However, for systems when there are clusters with small or medium size we have the clustered fluid. And for the percolated phases, in the percolation threshold the $N(s)$ will exhibit a power-law decay with a specific critical exponent related to the random percolation prediction, but the cluster percolated phase is a distinctly different structural state due to a different concentration and a preferred cluster size. Extracted from Ref. [63].

2.2 Langevin Dynamics

The basic idea of Langevin Dynamics (LD) is to reproduce the dynamics of a particle in suspension in a solvent, as a consequence, this particle will be subject to the Brownian motion. When the solute particle moves towards any direction, it is expected that it encounters more collisions pushing it back to the opposite direction of its flow. The simplest treatment of Brownian motion is just to apply the Newton's second law

$$m_i \frac{d\mathbf{v}_i}{dt} = -\zeta \mathbf{v}_i + \boldsymbol{f}_i(t), \tag{2.46}$$

where v is the velocity of the particle, ζ is the drag coefficient, that for spheres of radius R suspended in a liquid of viscosity η assumes $\zeta = 6\pi R\eta$. The last term is a stochastic force that comes from the collisions of the solvent particles and the solute, and also depends on the absolute temperature T acting as the heat bath coupling. One thing to keep in mind is the characteristic time scale for the $\boldsymbol{f}(t)$ forces. The stochastic force is related to the frequency of the collisions between the solvent and solute particles. So, $f(t)$, in general, fluctuates around a time scale on the order of 10^{-12} s [4], and this has to do with how often such collisions occur. As a consequence, if we measure the autocorrelation $\langle \boldsymbol{f}(t) \cdot \boldsymbol{f}(t + \delta t)\rangle$ it will decay around on time scale of picoseconds. However, in another hand, taking a look at the non-stochastic terms, we can notice that there is a natural time scale $\tau = m/\zeta$. For typical colloids suspended, e.g., in water τ is on the order of 10^{-7}. Therefore, what typically is done is that $\boldsymbol{f}(t)$ is approximated by a delta function [71]. In order to satisfy those dissipation-fluctuation assumptions, it is often assumed that the stochastic force is Gaussian distributed and has the statistical properties:

$$\langle \boldsymbol{f}_i(t) \rangle = 0, \tag{2.47}$$

$$\langle \boldsymbol{f}_i(t) \boldsymbol{f}_j(t') \rangle = \boldsymbol{G}_t \delta_{ij} \delta(t - t'), \tag{2.48}$$

where G_t is the translational fluctuation strength.

In the previous section we mentioned that the Berendsen thermostat does not reproduce the canonical ensemble, however, the most frequently used ensemble in statistical mechanics is the canonical (NVT) ensemble where the temperature of the system, rather than its energy, is constant. A variety of methods for conducting MD simulations in the canonical ensemble have been proposed over the years. An advantage of using LD simulations is that this method itself reproduces the (NVT) ensemble.

2.2.1 Langevin Equations for Rod-like particles

The drag coefficient is well-defined for spherical particles, as aforementioned $\zeta = 6\pi R\eta$. The point here is how we can define the drag coefficient present in the Langevin equations for rod-like particles.

♦ The creeping flow equations

The expression for drag force comes from the assumptions of the *Stokes flow*, therefore we must look into those assumptions for the rod-like case. The equation which rules such a behavior is the Navier-Stokes's

$$\rho \frac{\partial \boldsymbol{u}(\boldsymbol{r}, t)}{\partial t} + \rho \boldsymbol{u}(\boldsymbol{r}, t) \cdot \nabla \boldsymbol{u}(\boldsymbol{r}, t) = \eta_0 \nabla^2 \boldsymbol{u}(\boldsymbol{r}, t) - \nabla \rho(\boldsymbol{r}, t) + \boldsymbol{f}^{ext}, \tag{2.49}$$

where ρ is the density of the fluid, $\mathbf{u}$ is the flow velocity, η_0 is the viscosity of the fluid and $\boldsymbol{f}^{ext}$ is the external forces acting on the fluid. We are considering here incompressible fluids, such that $\nabla \cdot \boldsymbol{u}(\boldsymbol{r}, t) = 0$. A typical fluid flow velocity is the velocity v of the colloidal objects. The fluid flow velocity decreases from a value v, close to a Brownian particle, to a much smaller value, over a distance of the order of a typical linear dimension a of the particles (for rotating rods a is the length of the rod). Because of this, it is worth to introduce the rescaled variables

$$\boldsymbol{u}' = \boldsymbol{u}/v, \quad \boldsymbol{r}' = \boldsymbol{r}/a, \quad t' = t/(M/\zeta), \quad p' = \frac{a}{\eta_0 v} p, \quad \boldsymbol{f}'^{ext} = \frac{a^2}{\eta_0 v} \boldsymbol{f}^{ext}, \tag{2.50}$$

with M the mass of the colloidal particle. Those variables transform Eq. (2.49) to

$$\rho \frac{a^2 \zeta}{M \eta_0} \frac{\partial \boldsymbol{u}'}{\partial t'} + Re\, \boldsymbol{u}' \cdot \nabla' \boldsymbol{u}' = \nabla'^2 \boldsymbol{u}' - \nabla' p' + \boldsymbol{f}'^{ext}. \tag{2.51}$$

The dimensionless number Re is the so-called *Reynolds number*. For a diffusive regime the time scale is $\gg M/\zeta$, then we can neglect the time derivative contribution due to relaxation of the Brownian particle velocity as a result of friction with the solvent during the time interval M/ζ. In addition, for a typical situation in flows when the fluid velocities are very slow compared to large values of the viscosities, we have $Re \ll 1$. So, Eq. (2.50) is simplified to

$$\nabla p(\boldsymbol{r}, t) - \eta_0 \nabla^2 \boldsymbol{u}(\boldsymbol{r}, t) = \boldsymbol{f}^{ext}(\boldsymbol{r}). \tag{2.52}$$

Together with the incompressibility condition ($\nabla \cdot \boldsymbol{u}(\boldsymbol{r}, t) = 0$) Eq. (2.52) is the *creeping flow equations* [72]. They are also refereed to *Stokes flow equations* and it is related to the fact that Reynolds number is small, which is the case when the typical fluid flow velocity v is small. The velocity of the Brownian particle can be estimated from the equipartition theorem $\frac{1}{2}M\left\langle v^2\right\rangle = \frac{3}{2}k_B T$. For typical scales of colloidal particles already discussed in the previous chapter, we find the Reynolds number on the order of 10^{-2} [73], justifying the using of the creeping flow equations for colloidal particles, of which the inertial forces are thus small in comparison to pressure and friction forces.

♦ The Oseen Tensor

As the force acts only at a single point $\mathbf{r}'$ of the fluid, $\boldsymbol{f}^{ext}$ can be described as

$$\boldsymbol{f}^{ext}(\boldsymbol{r}) = \boldsymbol{f}_0 \delta(\boldsymbol{r} - \boldsymbol{r}'), \tag{2.53}$$

where $\boldsymbol{f}_0 = \int d\boldsymbol{r}' \boldsymbol{f}^{ext}(\boldsymbol{r}')$ is the total force acting on the fluid. As the creeping flow equations are linear, the velocity and pressure are proportional to $\boldsymbol{f}_0$ and they are also proportional to a tensor that connects a point $\mathbf{r}$ to $\mathbf{r}'$

$$\boldsymbol{u}(\boldsymbol{r}) = \boldsymbol{T}(\boldsymbol{r} - \boldsymbol{r}') \cdot \boldsymbol{f}_0, \tag{2.54}$$

$$\boldsymbol{p}(\boldsymbol{r}) = \boldsymbol{g}(\boldsymbol{r} - \boldsymbol{r}') \cdot \boldsymbol{f}_0. \tag{2.55}$$

Thus

$$\boldsymbol{u}(\boldsymbol{r}) = \int d\boldsymbol{r}' \boldsymbol{T}(\boldsymbol{r} - \boldsymbol{r}') \cdot \boldsymbol{f}^{ext}(\boldsymbol{r}'), \tag{2.56}$$

$$\boldsymbol{p}(\boldsymbol{r}) = \int d\boldsymbol{r}' \boldsymbol{g}(\boldsymbol{r} - \boldsymbol{r}') \cdot \boldsymbol{f}^{ext}(\boldsymbol{r}'). \tag{2.57}$$

Replacing Eqs. (2.56) and (2.57) into the creeping flow equations, this leads to Green's functions equations

$$\nabla \cdot \boldsymbol{T}(\boldsymbol{r}) = 0, \tag{2.58}$$

$$\nabla \boldsymbol{g}(\boldsymbol{r}) - \eta_0 \nabla^2 \boldsymbol{T}(\boldsymbol{r}) = \hat{\boldsymbol{I}} \delta(\boldsymbol{r}), \tag{2.59}$$

where $\hat{\boldsymbol{I}}$ is the (3×3)-dimensional unit tensor. Solving the differential equations we end up to

$$\boldsymbol{T}(\boldsymbol{r}) = \frac{1}{8\pi\eta_0} \frac{1}{r} \left[\hat{\boldsymbol{I}} + \frac{\boldsymbol{r}\boldsymbol{r}}{r^2}\right], \tag{2.60}$$

$$\boldsymbol{g}(\boldsymbol{r}) = \frac{1}{4\pi} \frac{\boldsymbol{r}}{r^3}. \tag{2.61}$$

The Oseen tensors are the Green's functions for the creeping flow equations and these will help us to derive the drag coefficients for rod-like particles.

♦ Hydrodynamic Friction of a Single Peapod-Like Rod

As already mentioned, we use in this thesis a rod consisting of beads. In the present section, the friction coefficient for long and thin rods will be derived. This approach makes such a derivation more easily, by considering a rod to be made up of spherical beads with a diameter D as illustrated in Fig. 2.8. The number of beads is given by $nL/D-1$(with L the length of the rod). With n ranging from $-n/2$ to $+n/2$. The flow velocity around a moving rod is given, using Eq. (2.56)

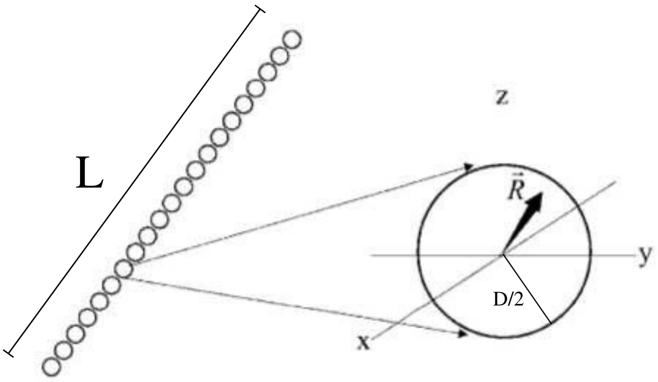

Figure 2.8: The peapod-like rod representation and the definition of the vector **R** on the surface of a bead. Modified from Ref. [73].

$$\boldsymbol{u}(\boldsymbol{r}) = \oint_{\partial V} d\boldsymbol{S}' \, \boldsymbol{T}(\boldsymbol{r}-\boldsymbol{r}') \cdot \boldsymbol{f}^{ext}(\boldsymbol{r}'), \tag{2.62}$$

where the force $\boldsymbol{f}^{ext}(\boldsymbol{r}')$ is the applying force per unit area that a surface element at $\boldsymbol{r}'$ on the fluid. As the relative velocities of the solvent particles with respect to the Brownian particle is almost zero for creeping conditions, the velocity of the flow is equal to the colloidal particle velocity at its very close vicinity. Therefore, we can make use of stick boundaries conditions [74]

$$\boldsymbol{u}(\boldsymbol{r}) = \boldsymbol{v}_c + \boldsymbol{\Omega} \times (\boldsymbol{r}-\boldsymbol{r}_c), \quad \mathbf{r} \in \partial V, \tag{2.63}$$

where $\boldsymbol{v}_c$ and $\boldsymbol{r}_c$ is the translational velocity and the position of the center of the rod, respectively, and $\boldsymbol{\Omega}$ is the angular velocity of the rod with respect to its center. The center of the position of jth bead is denoted as $\mathbf{r}_j = \mathbf{r}_c + jD\hat{\mathbf{u}}$, $\hat{\mathbf{u}}$ is the unit vector along the long axis of the rod. Eq. (2.63) can be rewritten as

$$\boldsymbol{u}(\boldsymbol{R}+\boldsymbol{r_j}) = \sum_{i=-\frac{n}{2}}^{\frac{n}{2}} \oint_{\partial V_0} d\boldsymbol{S}' \, \boldsymbol{T}(\boldsymbol{R}-\boldsymbol{R}'+\boldsymbol{r_{ji}}) \cdot \boldsymbol{f}_i(\boldsymbol{R}'), \tag{2.64}$$

where $\boldsymbol{R} = \boldsymbol{r} - \boldsymbol{r}_j$, $\boldsymbol{R}' = \boldsymbol{r}' - \boldsymbol{r}_i$ and $R = D/2$. By the stick boundary conditions, Eq. (2.63) becomes

$$\boldsymbol{u}(\boldsymbol{R} + \boldsymbol{r_j}) = \boldsymbol{v}_c + \boldsymbol{\Omega} \times (\boldsymbol{R} - jD\hat{\boldsymbol{u}}). \tag{2.65}$$

The derivation of the friction coefficients are based on the assumption that the translational and rotational motion is a linear superposition of the results.

♦ Translational Friction

In this section, we are considering just the translational motion without shear flow, Eq. (2.65) reduces to $\boldsymbol{u}(\boldsymbol{R} + \boldsymbol{r_j}) = \boldsymbol{v}_c$. Such that

$$\boldsymbol{v}_c = \sum_{i=-\frac{n}{2}}^{\frac{n}{2}} \oint_{\partial V_0} d\boldsymbol{S}'\, \boldsymbol{T}(\boldsymbol{R} - \boldsymbol{R}' + \boldsymbol{r_{ji}}) \cdot \boldsymbol{f}_i(\boldsymbol{R}'). \tag{2.66}$$

We must do the integration $(\sum_{j=-\frac{n}{2}}^{\frac{n}{2}} \oint_{\partial V dS})$ in both sides of Eq. (2.66) which yelds

$$\boldsymbol{v}_c = \frac{1}{\pi L D} \sum_{j=-\frac{n}{2}}^{\frac{n}{2}} \sum_{i=-\frac{n}{2}}^{\frac{n}{2}} \oint_{\partial V_0} d\boldsymbol{S} \oint_{\partial V_0} d\boldsymbol{S}'\, \boldsymbol{T}(\boldsymbol{R} - \boldsymbol{R}' + \boldsymbol{r_{ji}}) \cdot \boldsymbol{f}_i(\boldsymbol{R}'). \tag{2.67}$$

By Eq. (2.60) we have

$$\oint_{\partial V_0} d\boldsymbol{S}'\, \boldsymbol{T}(\boldsymbol{r} - \boldsymbol{R}') = \frac{D}{4\eta_0} \left\{ \left[\frac{D}{2r} + \frac{1}{3}\left(\frac{D}{2r}\right)^3 \right] \hat{\mathbf{I}} + \left[\frac{D}{2r} - \left(\frac{D}{2r}\right)^3 \right] \frac{\mathbf{rr}}{r^2} \right\}. \tag{2.68}$$

We must analyze two cases, the first one, for $i = j$, the surface integrals in Eq. (2.67) are reduced to

$$\oint_{\partial V_0} d\boldsymbol{S}'\, \boldsymbol{T}(\boldsymbol{R} - \boldsymbol{R}' + \boldsymbol{r_{ji}}) = \frac{D}{3\eta_0} \hat{\mathbf{I}}. \tag{2.69}$$

The second case is for $i \neq j$, then we must do a Taylor-expansion in the Oseen tensor

$$\mathbf{T}(\mathbf{R} - \mathbf{R} + \mathbf{r_{ji}}) = \mathbf{T}(\mathbf{r_{ij}}) + (\mathbf{R} - \mathbf{R}') \cdot \boldsymbol{\nabla} \mathbf{T}(\mathbf{r_{ij}}). \tag{2.70}$$

Using Eqs. (2.67) and (2.69) and the leading order in L/D from Eq. (2.70), yields

$$\mathbf{v}_c \approx -\frac{1}{3\pi\eta_0 L} \sum_{i=-\frac{n}{2}}^{\frac{n}{2}} \mathbf{F}_i^h - \frac{D}{L} \left[\sum_{j=-\frac{n}{2}}^{\frac{n}{2}} \sum_{i=-\frac{n}{2}, i \neq j}^{\frac{n}{2}} \mathbf{T}(\mathbf{r}_{ij}) \right] \cdot \mathbf{F}_i^h, \tag{2.71}$$

where $\oint_{\partial V^0} d\mathbf{S}' \boldsymbol{f}_i(\mathbf{R}') = -\mathbf{F}_i^h$ is the total force on bead i. For long rods, all forces $\mathbf{F}_i^h$ can be take as equal since end-effects may be neglected, since the most of beads experiences approximately the same force, therefore, the total force on the rod is $\mathbf{F}^h = \frac{L}{D}\mathbf{F}_i^h$. After some math calculations Eq. (2.71) is reduced to (see the detailed derivation in Ref. [73])

$$\mathbf{v}_c \approx -\frac{1}{4\pi\eta_0 L} ln\left(\frac{L}{D}\right) [\hat{\mathbf{I}} + \hat{\mathbf{u}}\hat{\mathbf{u}}] \cdot \mathbf{F}^h. \tag{2.72}$$

We now can finally obtain the drag coefficient by inverting Eq. (2.72)

$$\boldsymbol{F}^h = -\boldsymbol{\Gamma}\cdot\boldsymbol{v}_c, \quad \text{with} \quad \boldsymbol{\Gamma} = \frac{4\pi\eta_0 L}{ln(L/D)}\left[\hat{\boldsymbol{I}} - \frac{1}{2}\hat{\boldsymbol{u}}\hat{\boldsymbol{u}}\right]. \tag{2.73}$$

Notice that Γ is the drag coefficient and it is now a tensor. Also, the drag coefficient for rods is no longer collinear with its velocity, i.e., it depends on the orientation of the motion of the rod. When this is parallel to its orientation, the friction force on the rod can be obtained by multiplying the force expression in Eq. (2.73) by $\hat{\mathbf{u}}\hat{\mathbf{u}}$

$$\boldsymbol{F}^{\boldsymbol{h}}_{\parallel} = -\zeta_{\parallel}\boldsymbol{v}_{\parallel}, \quad \text{with} \quad \zeta_{\parallel} = \frac{2\pi\eta_0 L}{ln(L/D)}. \tag{2.74}$$

For the motion perpendicular to the rod axis, we multiply Eq. (2.73) by $\hat{\mathbf{I}} - \hat{\mathbf{u}}\hat{\mathbf{u}}$ instead

$$\boldsymbol{F}^{\boldsymbol{h}}_{\perp} = -\zeta_{\perp}\boldsymbol{v}_{\perp}, \quad \text{with} \quad \zeta_{\perp} = \frac{4\pi\eta_0 L}{ln(L/D)}, \tag{2.75}$$

where $\zeta_{\parallel}$ and $\zeta_{\perp}$ are the parallel and perperdincular components of the drag coefficients. In addition, $\boldsymbol{F}^h = F^h_{\parallel}\hat{\boldsymbol{u}}\hat{\boldsymbol{u}} + F^h_{\perp}[\hat{\boldsymbol{I}} - \hat{\boldsymbol{u}}\hat{\boldsymbol{u}}]$, $\boldsymbol{v}_c = v_{\parallel}\hat{\boldsymbol{u}}\hat{\boldsymbol{u}} + v_{\perp}[\hat{\boldsymbol{I}} - \hat{\boldsymbol{u}}\hat{\boldsymbol{u}}]$ and $\boldsymbol{\Gamma} = \zeta_{\parallel}\hat{\boldsymbol{u}}\hat{\boldsymbol{u}} + \zeta_{\perp}[\hat{\boldsymbol{I}} - \hat{\boldsymbol{u}}\hat{\boldsymbol{u}}]$. In terms of simulation, it is easier to represent the velocities and the forces with respect to the parallel and perpendicular axis of the rods, in order to simulate the effect of the drag force on such an anisotropic-shape particles.

♦ Rotational Friction

Once we have obtained the total force on each bead belonging to a rod, the derivation of the rotational friction is straightforward. For the orientational case, the translation is zero ($\mathbf{v}_c = 0$). Consider the torque on a rod

$$\boldsymbol{N} = \sum_{i=-\frac{n}{2}}^{\frac{n}{2}} \boldsymbol{r}_i \times \boldsymbol{F}^h_i, \quad \text{with} \quad \boldsymbol{r}_i = iD\hat{\boldsymbol{u}} \quad \text{and} \quad \boldsymbol{F}^h_i = \frac{D}{L}\boldsymbol{F}^h, \tag{2.76}$$

thus

$$\boldsymbol{N} = -\frac{D^3}{L}\zeta_{\perp}[\hat{\boldsymbol{u}} \times (\boldsymbol{\Omega} \times \hat{\boldsymbol{u}})] \sum_{i=-\frac{n}{2}}^{\frac{n}{2}} i^2. \tag{2.77}$$

Then, using $\sum_{i=-n/2}^{n/2} \approx \frac{n^3}{12}$, for large n

$$\boldsymbol{N} = -\frac{L^2}{12}\zeta_{\perp}\boldsymbol{\Omega}, \tag{2.78}$$

and therefore

$$\boldsymbol{N} = -\zeta_r\boldsymbol{\Omega}, \quad \text{with} \quad \zeta_r = \frac{\pi\eta_0 L^3}{3\,ln(L/D)}, \tag{2.79}$$

where ζ_r is the drag coefficient for a rotating rod. That finishes the derivation of the drag coefficients.

Correction for small L/D

The derivation of the drag coefficients in the last subsections made use of the assumption that the rods are very long. But it is possible to use such expressions for small rods upon making corrections for each expression of ζ. The correction factors was first obtained in Refs. [75, 76]

$$\zeta_{\parallel} = \frac{2\pi\eta_0 L}{ln(L/D)+\delta_{\perp}}, \quad \zeta_{\perp} = \frac{4\pi\eta_0 L}{ln(L/D)+\delta_{\perp}}, \quad \zeta_r = \frac{\pi\eta_0 L^3}{3\,ln(L/D)+\delta_r}, \tag{2.80}$$

where

$$\begin{aligned} \delta_{\parallel} &= -0.207+\frac{0.987}{L/D}-\frac{0.133}{(L/D)^2}, \\ \delta_{\perp} &= 0.839+\frac{0.185}{L/D}+\frac{0.233}{(L/D)^2}, \\ \delta_r &= -0.622+\frac{0.917}{L/D}-\frac{0.050}{(L/D)^2}. \end{aligned} \tag{2.81}$$

In Fig. 2.9, we illustrate the perpendicular component of the drag coefficient before and after applying the correction factors as a function of small values of aspect ratio.

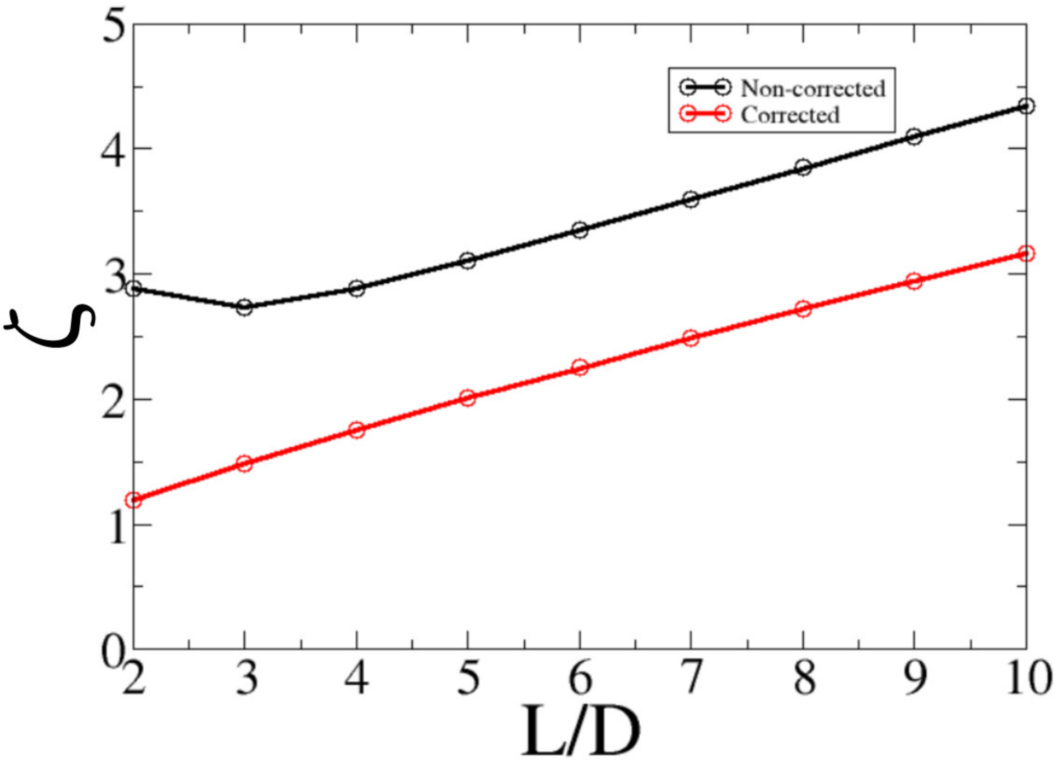

Figure 2.9: Non-corrected and corrected perpendicular component of the drag coefficient as a function of the aspect ratio.

2.2.2 Fluctuation Strengths

The Langevin equations for linear rod-like particles, as presented in the last sections, are

$$m\frac{d\mathbf{v}}{dt} = -\mathbf{\Gamma}\cdot\mathbf{v} + \boldsymbol{f}(t), \tag{2.82}$$

$$I\frac{d^2\mathbf{\Omega}}{dt} = -\zeta_r\mathbf{\Omega} + \mathbf{T}(t). \tag{2.83}$$

As mentioned in the previous sections, $\boldsymbol{f}(t)$ is the fluctuating force. Similarly, $T(t)$ is the fluctuating torque. As the fluctuating force [see Eqs. (2.47), and (2.48)], the fluctuating torque has similar statistical properties as

$$\langle\mathbf{T}(t)\rangle = 0, \tag{2.84}$$

$$\langle\mathbf{T}(t)\mathbf{T}(t')\rangle = \boldsymbol{G}_r\delta(t-t'). \tag{2.85}$$

Similarly, as G_t is the translational fluctuation strength in Eq. (2.48), G_r is the rotational fluctuation strength. We can derive G_t easily by splitting $\boldsymbol{f}(t)$ into the parallel and perpendicular components. Therefore the statistical properties of each components are

$$\langle\boldsymbol{f}_{\parallel}(t)\rangle = 0, \tag{2.86}$$

$$\langle\boldsymbol{f}_{\perp}(t)\rangle = 0, \tag{2.87}$$

$$\langle\boldsymbol{f}_{\parallel}(t)\cdot\boldsymbol{f}_{\parallel}(t')\rangle = G_{\parallel}\delta(t-t'), \tag{2.88}$$

$$\langle\boldsymbol{f}_{\perp}(t)\cdot\boldsymbol{f}_{\perp}(t')\rangle = G_{\perp}\delta(t-t'), \tag{2.89}$$

where $\boldsymbol{f}_{\parallel}(t) = f_{\parallel}(t)\hat{\mathbf{u}}\hat{\mathbf{u}}$ and $\boldsymbol{f}_{\perp}(t) = f_{\perp}(t)(\hat{\mathbf{I}} - \hat{\mathbf{u}}\hat{\mathbf{u}})$.

The general solutions for Eq. (2.82), for both components of $\mathbf{v}$ are

$$v_{\parallel}(t) = v_{\parallel}(0)e^{-\frac{\zeta_{\parallel}}{m}t} + \frac{1}{m}\int_0^t e^{-\frac{\zeta_{\parallel}}{m}(t-t'}f_{\parallel}(t')dt', \tag{2.90}$$

$$v_{\perp}(t) = v_{\perp}(0) + e^{-\frac{\zeta_{\perp}}{m}t} + \frac{1}{m}\int_0^t e^{-\frac{\zeta_{\perp}}{m}(t-t'}f_{\perp}(t')dt'. \tag{2.91}$$

Squaring, Eqs. (2.90) and (2.91) we have

$$v_{\parallel}(t)^2 = v_{\parallel}(0)^2e^{-\frac{2\zeta_{\parallel}}{m}t} + \frac{2v(0)}{m}e^{-\frac{2\zeta_{\parallel}}{m}t}\int_0^t e^{-\frac{\zeta_{\parallel}}{m}(t-t')}f_{\parallel}(t')dt' + \\ + \frac{1}{m^2}\int_0^t e^{-\frac{\zeta_{\parallel}}{m}(t-t')}f_{\parallel}(t')dt'\int_0^t e^{-\frac{\zeta_{\parallel}}{m}(t-t'')}T(t'')dt'', \tag{2.92}$$

$$v_{\perp}(t)^2 = v_{\perp}(0)^2e^{-\frac{2\zeta_{\perp}}{m}t} + \frac{2v(0)}{m}e^{-\frac{2\zeta_{\perp}}{m}t}\int_0^t e^{-\frac{\zeta_{\perp}}{m}(t-t')}f_{\perp}(t')dt' + \\ + \frac{1}{m^2}\int_0^t e^{-\frac{\zeta_{\perp}}{m}(t-t')}f_{\perp}(t')dt'\int_0^t e^{-\frac{\zeta_{\perp}}{m}(t-t'')}f_{\perp}(t'')dt''. \tag{2.93}$$

Taking the average $\lim_{t\to\infty}\langle\ldots\rangle$, and using Eqs. (2.88) and (2.87)

$$\lim_{t\to\infty}\left\langle v(0)^2 e^{-2\frac{\zeta}{m}t}\right\rangle = 0, \tag{2.94}$$

$$\lim_{t\to\infty}\left\langle 2e^{-2\frac{\zeta}{m}t}v(0)\int_0^t e^{-\frac{\zeta_\perp}{m}(t-t')}f(t')dt'\right\rangle = 0, \quad \text{since} \quad \langle f(t)\rangle = 0. \tag{2.95}$$

Referring v, ζ and f as general velocities, drag coefficient and fluctuating force, respectively in Eqs. (2.92) and (2.93)

$$\left\langle v^2\right\rangle = \lim_{t\to\infty}\frac{1}{m^2}\int_0^t\int_0^t e^{-\frac{\zeta}{m}(t-t')}e^{-\frac{\zeta}{m}(t-t')}\left\langle f(t')f(t'')\right\rangle dt'dt'', \tag{2.96}$$

$$\left\langle v^2\right\rangle = \lim_{t\to\infty}\frac{1}{m^2}\int_0^t\int_0^t e^{-\frac{\zeta}{m}(t-t')}e^{-\frac{\zeta}{m}(t-t')}G\delta(t'-t'')dt'dt''. \tag{2.97}$$

Using Eqs. (2.86) and (2.87), we have

$$\left\langle v^2\right\rangle = \lim_{t\to\infty}\frac{1}{m^2}\int_0^t e^{\frac{-2\zeta}{m}(t-t')}Gdt', \tag{2.98}$$

$$\left\langle v^2\right\rangle = \frac{G}{2m\zeta}. \tag{2.99}$$

By the equipartition theory, for a two-dimensional rods system, we have that

$$\left\langle v_\parallel^2\right\rangle = \frac{k_BT}{m}, \tag{2.100}$$

$$\left\langle v_\perp^2\right\rangle = \frac{k_BT}{m}. \tag{2.101}$$

and finally

$$G_\parallel = 2k_BT\zeta_\parallel, \tag{2.102}$$

$$G_\perp = 2k_BT\zeta_\perp. \tag{2.103}$$

The derivation of the rotational fluctuation strength is similar to it was presented for the translational case. Using the fact that $\langle\Omega^2\rangle = k_BT/I$, we get

$$G_r = 2k_BT\zeta_r. \tag{2.104}$$

Once the fluctuation strengths is obtained, we can rewrite the Langevin equations, replacing $\boldsymbol{f}_\parallel(t) = \sqrt{2k_BT\zeta_\parallel/\delta t}\hat{\boldsymbol{\xi}}_\parallel(t)$ and $\boldsymbol{f}_\perp(t) = \sqrt{2k_BT\zeta_\perp/\delta t}\hat{\boldsymbol{\xi}}_\perp(t)$ [77, 78], where $\hat{\boldsymbol{\xi}}_\parallel(t)$ and $\hat{\boldsymbol{\xi}}_\perp(t)$ are a dimensionless stationary Gaussian process with zero mean and unit variance [79].

Part III

Results

3

Self-assembly of rigid magnetic rods consisting of single dipolar beads in two dimensions

MD simulations are used to investigate the structural properties of a two-dimensional ensemble of magnetic rods, which are modelled as aligned single dipolar beads. A diversity of self-assembled configurations that we characterized as: (1) clusters, (2) percolated and (3) ordered structures, are identified and the structural properties of those different phases are investigated in detail. By increasing the aspect ratio of the magnetic rods, we show that the percolation transition is suppressed due to the decreased mobility in two dimensions. Such a behavior is opposite to the one observed previously in three dimensions. A magnetic bulk phase is found with local ferromagnetic order and an unusual non-monotonic behavior of the nematic order is shown.

3.1 Motivation

Recent years has witnessed a growing interest in the self assembly of magnetic nanoparticles (MN) due to its wide range of applications, including magnetic fluids [15], biomedicine [16], magnetic resonance imaging (MRI) [17], data storage [18], magnetic filaments [80, 81, 82], among others. Basically, MN are particles with a magnetic dipole moment, which are regarded as particles composed of a magnetic mono-domain having a typical size from 15 to 150 *nm* [19]. Many efforts are currently being devoted to the synthesis and characterization of magnetic particles with anisotropic shape [83, 84]. Magnetic rod-like particles are often used as microrheology probes to enhance the visualization of their viscoelastic properties [22, 23]. Also, magnetic rods can be applied: (i) as components in micromechanical units [24, 25, 26]; (ii) as microscale propellers [27, 28, 29]. In addition to aforementioned applications, particles with anisotropic shape show distinguished properties when compared to their spherical counterparts, namely, magnetic birefringence [30] and thermal conductivity [31].

In this work we present a numerical study of the self-assembly of a two- dimensional system of stiff magnetic rods, composed of single dipolar beads linked one by one through internal head-to-tail alignment. A similar system was used earlier in experiment [37] and simulations [36]. Our motivation to explore in more detail the two-dimensional ($2D$) situation is driven by the fact that many experiments involving assemblies of colloids are actually done at surfaces and/or thin films [85, 86, 87, 88, 89].

Our model is characterized by permanently linked dipolar beads so that the net interaction is given by the superposition of dipolar fields of single dipole beads. This opens the possibility of new kinds of assembled clusters distinct from rod-like particles with a *single* longitudinal (or transversal) dipole moment, which was intensively studied both by theory and simulations [90, 91].

We also study the connectivity properties of the present system. The percolation behavior is of great relevance in highly connected materials due to the possibility of enhancing the electrical and thermal conductivity [94, 37]. In general, percolation in polymers plays a fundamental role in properties related to conductivity, because in many cases percolation can be made responsible for electrical switching properties. A goal in studying the connectivity properties is to explore the conditions under which the percolation transition is enhanced. By using elongated particles, it was already shown that an increase of the aspect ratio decreases the percolation threshold [95, 36]. The latter has also been realized by depletion effects [96] and by the application of an external-field [97, 36]. In the present work, we discuss the connectivity properties of magnetic rods in a $2D$ system, and show that the percolation transition with respect to the density behaves opposite as compared to the $3D$ case.

The last aim of this study is to analyze the appearance of orientational ordering. It is already known that elongated particles present nematic and smetic transitions driven by entropic effects so that they are isotropic for low densities and nematic for high densities [98]. In a recent study of a $3D$ system of magnetic nanorods (MNR), similar to the ones studied in this work, an improvement of the stability of the nematic phase was found for sufficiently long MNRs as a consequence of the interaction resulting from the arrangement of the dipoles along each MNR [36]. In our $2D$ system we find a different scenario, where a non-monotonic behavior of the nematic order parameter is observed for sufficiently long MNRs, as a consequence of the appearance of magnetic bulk domains.

This chapter is organized as follows: our model system is presented in Sec. 3.2. The results for the different cluster configurations are presented in Sec. 3.3. The connectivity properties are discussed in Sec. 3.4 and the ordered configurations in Sec. 3.5. Our conclusions are given in Sec. 3.6.

3.2 Model

MD simulations were used to investigate two-dimensional systems consisting of 2520 up to 2820 identical soft beads of diameter σ with a point-like magnetic dipole at their center. A stiff rod is formed by those soft beads, with their positions fixed with respect to the center of mass of the rod. The orientation of the dipoles is always aligned along the rod, as illustrated in Fig. 3.1. The length of the rod is defined as $l\sigma$, where l is the number of beads, which is also its aspect ratio. To model the dipolar particles we use a dipolar soft sphere (DSS) potential [9], consisting of the repulsive part of the Lennard-Jones potential u^{rep} and a point-like dipole-dipole interaction part u^D. It was found that this potential does not induce a vapor-liquid phase transition as, e.g., the Stockmayer potential does [9, 10]. The interaction energy between two rods a and b is the sum of the pair interactions between their respective dipolar spheres (DS)

$$U_{a,b}(\mathbf{R}_{a,b}, \theta_a, \theta_b) = \sum_{j \neq m} u_{j,m}, \tag{3.1}$$

$$u_{j,m} = u^{rep}(\mathbf{r}^{a,b}_{jm}) + u^D(\mathbf{r}^{a,b}_{jm}, \boldsymbol{\mu}^a_j, \boldsymbol{\mu}^b_m), \tag{3.2}$$

where

$$u^{rep} = 4\epsilon \left(\frac{\sigma}{r_{jm}}\right)^{12}, \tag{3.3}$$

$$u^D = \frac{\boldsymbol{\mu}_j \cdot \boldsymbol{\mu}_m}{r^3_{jm}} - \frac{3(\boldsymbol{\mu}_j \cdot \mathbf{r}_{jm})(\boldsymbol{\mu}_m \cdot \mathbf{r}_{jm})}{r^5_{jm}}, \tag{3.4}$$

with $\mathbf{R}_{a,b}$ the vector joining the center of rods a and b with orientations θ_a and θ_b. The vector $\mathbf{r}^{a,b}_{jm}$ connects the center of bead m of rod a with respect to the center of bead j of rod b (Fig. 3.1). The force between two beads is given by

$$\mathbf{f}_{jm} = -\boldsymbol{\nabla} u_{jm}. \tag{3.5}$$

The torque on bead m, (see the Appendix A) is

$$\mathbf{N}_m = \boldsymbol{\mu}_m \times \sum_{m \neq j} \mathbf{B}_{jm} + \mathbf{d}_m \times \sum_{m \neq j} \mathbf{f}_{jm}, \tag{3.6}$$

where $\mathbf{d}_m$ is the vector joining the center of the rod with the center of bead m, as illustrated in Fig. 3.1 and $\mathbf{B}_{jm}$ is the magnetic field generated by the dipole moment μ_j at the position of the dipole μ_m, which is given by

$$\mathbf{B}_{jm} = \frac{3(\boldsymbol{\mu}_m \cdot \mathbf{r}_{jm})\mathbf{r}_{jm}}{r^5_{jm}} - \frac{\boldsymbol{\mu}_m}{r^3_{jm}}. \tag{3.7}$$

The summations in Eq. (3.6) are considered only for dipoles belonging to distinct rods. The orientation of the rods is given by a unitary vector $\mathbf{s}$ given by $\mathbf{s} = \mathbf{d}_m/|\mathbf{d}_m|$. We solve the translational and rotational equations of motion using a leapfrog algorithm:

$$r_\alpha(t + \delta t) = r_\alpha(t) + v_\alpha(t + \delta t/2)\delta t, \tag{3.8}$$

$$s_\alpha(t + \delta t) = s_\alpha(t) + u_\alpha(t + \delta t/2)\delta t. \tag{3.9}$$

The sub-index α refers to the α-component of the vectors $\mathbf{r}$, $\mathbf{v}$, $\mathbf{s}$, and $\mathbf{u}$, with $\mathbf{u} = \boldsymbol{\omega} \times \mathbf{s}$, where ω is the angular velocity. We introduce the reduced units $t^* = t/\sqrt{\epsilon^{-1} m\sigma^2}$ for time,

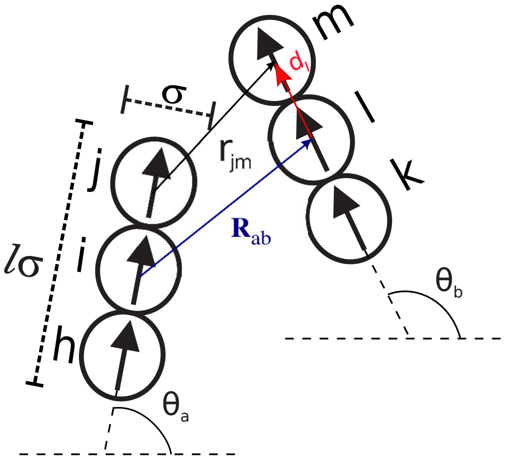

Figure 3.1: Schematic illustration of the interaction between two magnetic rods with indication of the important parameters of the pair interaction potential.

where m is the mass of the rod, $U^* = U/k_BT$ is for energy, where k_B is the Boltzmann constant, $\mu^* = \mu/\sqrt{k_BT\sigma^3}$ is for dipole moment, and, finally, $r^* = r/\sigma$ is for position. The ratio of thermal energy to soft-sphere repulsion constant is chosen as $k_BT/\epsilon = 0.1$, which is also our reduced unit of temperature $T^* = Tk_B/\epsilon$. In order to fix the temperature, we employ the Berendsen thermostat [51, 99] with a time constant $\tau = 2\delta t$, where the time step was taken as $\delta t = 0.005 - 0.01$. Periodic boundary conditions are taken in both spatial directions. In the $2D$ case, the dipolar pair interaction falls off fast (r^{-3}) and therefore it is sufficient to take the simulation box sufficiently large such that no special long-range summation techniques [41] has to be used as in the case for e.g. Coulomb $1/r$ interactions. We define the packing fraction as $\eta = \rho^* l\pi/4$, where ρ^* is the dimensionless density $\rho^* = \rho\sigma^2$.

To check the equilibration in our simulations we follow the total energy as a function of time. In equilibrium, the total energy fluctuates around an average value. For very dilute systems ($\eta < 0.2$) the equilibrium is reached after 1×10^6 time steps ($1 \times 10^4\sqrt{\epsilon^{-1}m\sigma^2}$), while for $\eta \geq 0.2$ we need about $5 \times 10^5 - 1 \times 10^6$ time steps ($2.5 \times 10^3\sqrt{\epsilon^{-1}m\sigma^2} - 5 \times 10^3\sqrt{\epsilon^{-1}m\sigma^2}$). Time averages over energies and other quantities are taken over 1×10^6 time steps after equilibrium is reached. Unless stated, we consider $\sigma^* = 1$ and $\mu^{*2} = 10$, which means that each bead has the same magnitude of dipole moment. Such a value is justified by the fact that we aim to investigate the weak coupling regime, in order to emphasize the geometrical effects due to the increase of the aspect ratio of the particles. Common experimental values of μ^{*2} at room temperature ranges in the interval $1 \leq \mu^{*2} \leq 100$. For example, in experiments using iron nanoparticles [37], it is found that the saturation magnetization $M_s(\text{Fe}) = 1700\ kA/m$ and the radius of the particles is $r \approx 5\ nm$. In this case, we estimate $\mu^* \approx 4.4$ at room temperature ($T \approx 293\ K$). Also, in experiments [101] carried out using aqueous dispersions of superparamagnetic microspheres of ferrite grains (Estapor (R) from Merck - reference M1- 030/40) for $r \approx 205\ nm$ and $M_s \approx 6 \times 10^4$ A/m, the magnetization (M) of the particles is completely reversible and adjustable by an external magnetic field. If we consider $T = 293\ K$ and $M \approx 22,6\%$ of M_s on that system, we obtain $\mu^* \approx 3.16$ $(\sim \sqrt{10})$.

The minimum energy configuration was chosen among the ones obtained by running simulations several times $(10 - 30)$, each with distinct initial conditions (coordinates and momenta).

3.3 Cluster Formation

We start by presenting the dependence of the DSS pair interaction potential on the angle and separation between the rods. The study of the pair interaction potential is interesting to understand the nature of the resulting many-body interaction and to help us to set the values of the parameters useful to analyze the results. The dependence of the DSS pair interaction potential as a function of the angle ϕ between rods (with aspect ratio $l = 4$) is presented in Fig. 3.2(a) for different separation δ. The separation δ is defined as the shortest distance between two rods for a given angle [see inset in Fig. 3.2(a)]. We

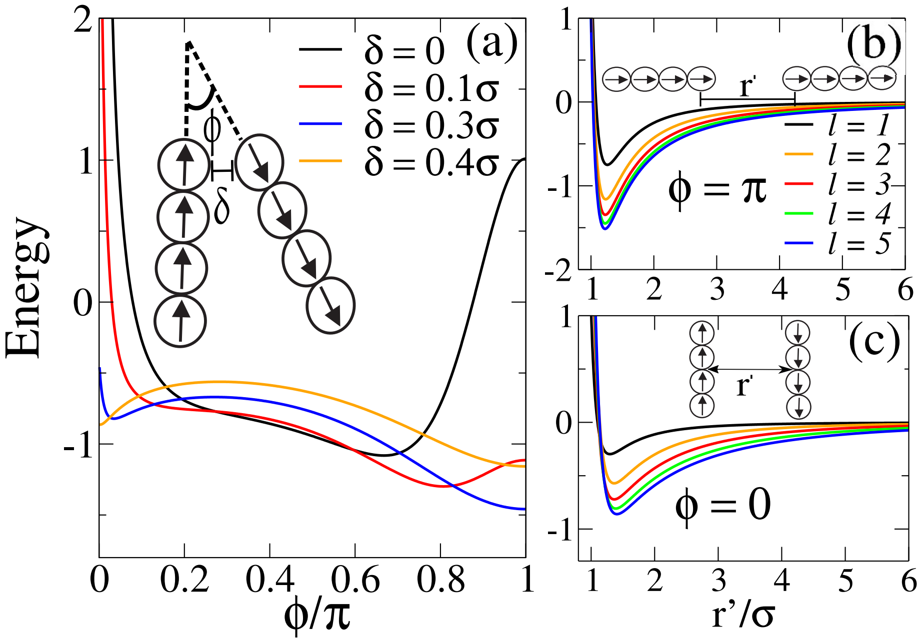

Figure 3.2: The pair interaction energy (a) as a function of the angle ϕ for different inter-rod separation δ; (b) as a function of the interparticle distance for $\phi = \pi$, and (c) for $\phi = 0$. In (*b*) and (*c*) the different colors represent different values of the aspect ratio, indicated in (*b*).

choose $\delta = 0.4\sigma$ as the separation distance at which we consider two rods as being bonded. In Fig. 3.2(a) the curve for $\delta = 0.4\sigma$ exhibits a local minimum for $\phi = 0$ and a global minimum at $\phi = \pi$, justifying our choice for the critical value of δ. The results shown in Fig. 3.2 are for $l = 4$, but the same critical distance was taken for all values of l considered in this study, since such a behavior of the interaction potential remains for different l

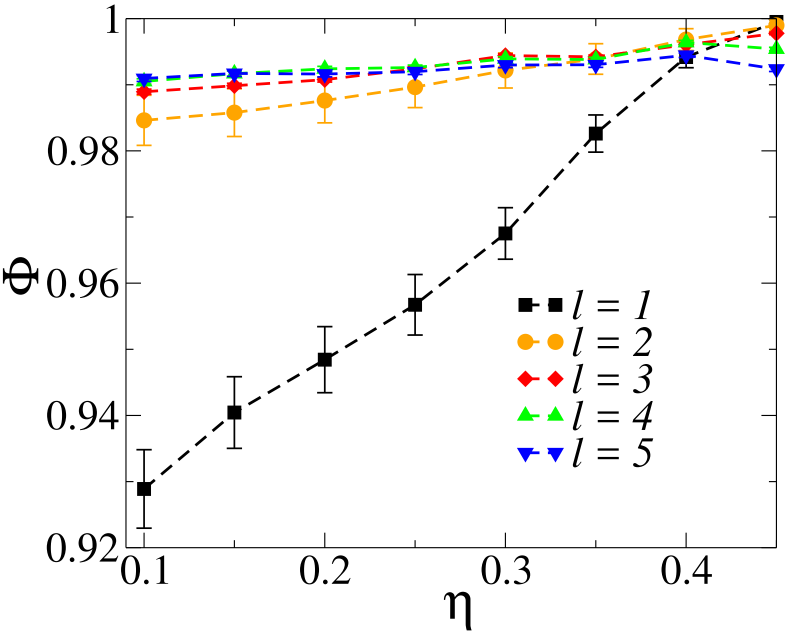

Figure 3.3: The polymerization as a function of the packing fraction η for different aspect ratios.

values. The dependence of the pair interaction potential with respect to the separation between two rods for different aspect ratio is shown in Fig. 3.2(b) for $\phi = \pi$ (parallel head-to-tail alignment) and in Fig. 3.2(c) for $\phi = 0$ (side-by-side dipoles with opposite orientation). In both cases, the attraction for low separation increases with increasing aspect ratio. Note that the parallel head-to-tail assembly ($\phi = \pi$) is energetically more favorable for the formation of chains, for every l, as found in ferrofluids in the absence of external magnetic fields, both in simulations [102, 103, 104] and in experiment [105].

The attraction between magnetic rods becomes stronger for larger l, suggesting that, in the many-body case, the formation of clusters is facilitated as l increases. To show if this is indeed the case, we analyze the degree of polymerization [58], defined as:

$$\Phi = \left\langle \frac{N_c}{N} \right\rangle , \tag{3.10}$$

where N_c is the number of clustered rods and N is the total number of rods.

In Fig. 3.3 the polymerization Φ as a function of η is presented for different aspect ratio. In general $0.92 < \Phi < 1$, which is consistent with a previous molecular dynamics study of dipole-like colloids [106] for $T^* = 0.1$, where Φ increases with increasing η. For $l = 1$, the behavior stands out from the other l values, which is a consequence of the increase of the interparticle attraction with increasing l for low packing fraction as shown in Figs. 3.2(b) and 3.2(c). For $\eta \geq 0.4$, the degree of polymerization presents the opposite dependence with respect to l, i.e., Φ decreases with increasing l. Since in highly dense systems, the larger aspect ratio of the rods introduces strong depletion interaction restricting the head-to-tail arrangements of the rods. We discuss such a behavior in more detail in the next section.

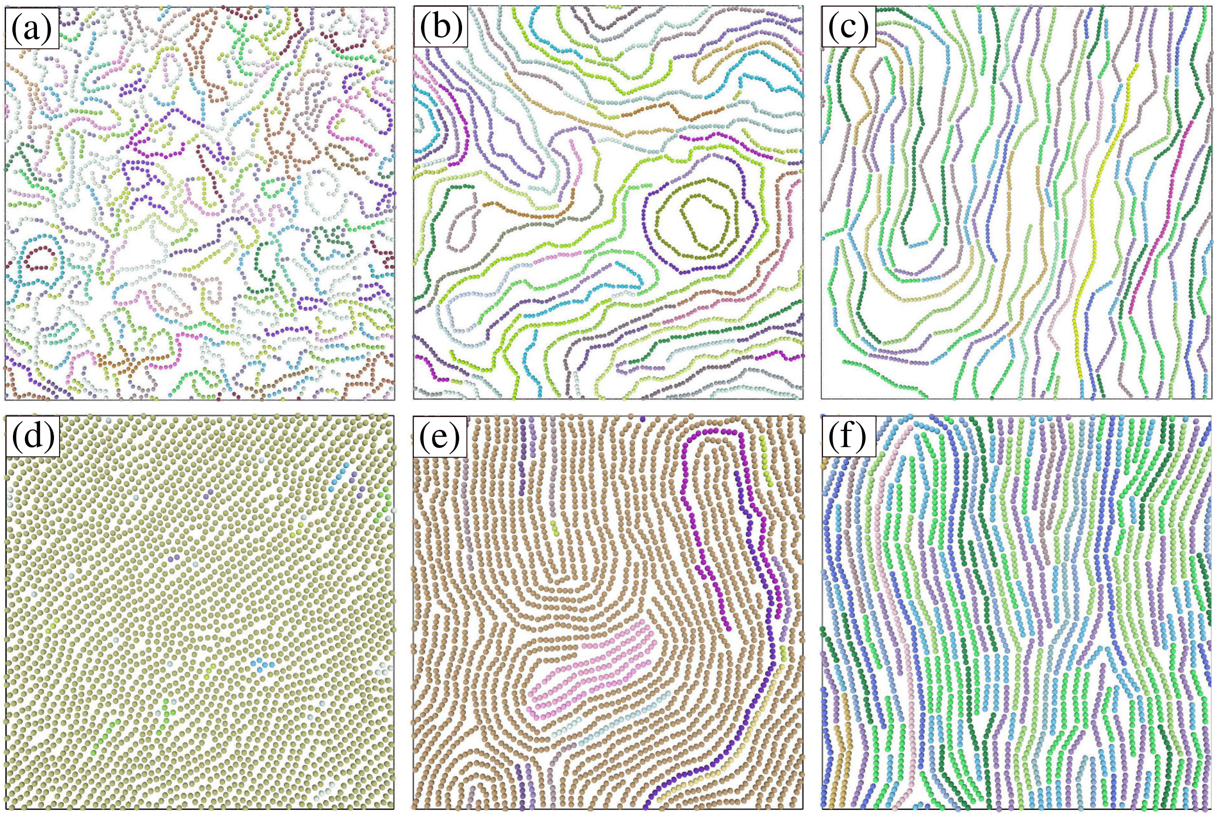

Figure 3.4: Some representative equilibrium configurations for $T^* = 0.1$. Each color represents a different size of cluster. (d) and (e) Percolated systems. (a) $\eta = 0.2$, $l = 1$; (b) $\eta = 0.2$, $l = 3$; (c) $\eta = 0.2$, $l = 5$; (d) $\eta = 0.4$, $l = 1$; (e) $\eta = 0.4$, $l = 3$; (f) $\eta = 0.4$, $l = 5$.

Some representative equilibrium configurations are presented in Fig. 3.4. The head-to-tail tendency is present in all configurations. For low packing fraction the chains can form rings, which are not observed for $l = 5$ due to geometrical reasons. In the large packing fraction regime ($\eta \geq 0.4$) the side-by-side arrangement comes into play.

We analyze the structure of the system by computing the pair correlation function [8]:

$$\mathbf{g}(\mathbf{r}) = \frac{\left\langle \sum_a \sum_{b \neq a}^{N} \delta(r - R_{ab}) \right\rangle}{2N\pi r \rho^*}, \tag{3.11}$$

where R_{ab} is the separation between the center of the rods a and b (see Fig. 3.1). As shown in Fig. 3.5(a), for low packing fraction, the position of the multiple peaks are related to the length of the rod for all l. This is the result of the head-to-tail alignment of neighboring rods. For a higher packing fraction ($\eta = 0.4$) intermediate peaks are observed [Fig. 3.5(b)]. For example, for $l = 3$, besides peaks at multiples of 3σ, there is a peak at $r \approx 1.8\sigma$. For $l = 5$, there are peaks at $r \approx 1.8\sigma$ and $r \approx 3.8\sigma$. These intermediate peaks are due to the side-by-side configuration of neighboring rods, either parallel, antiparallel, or both.

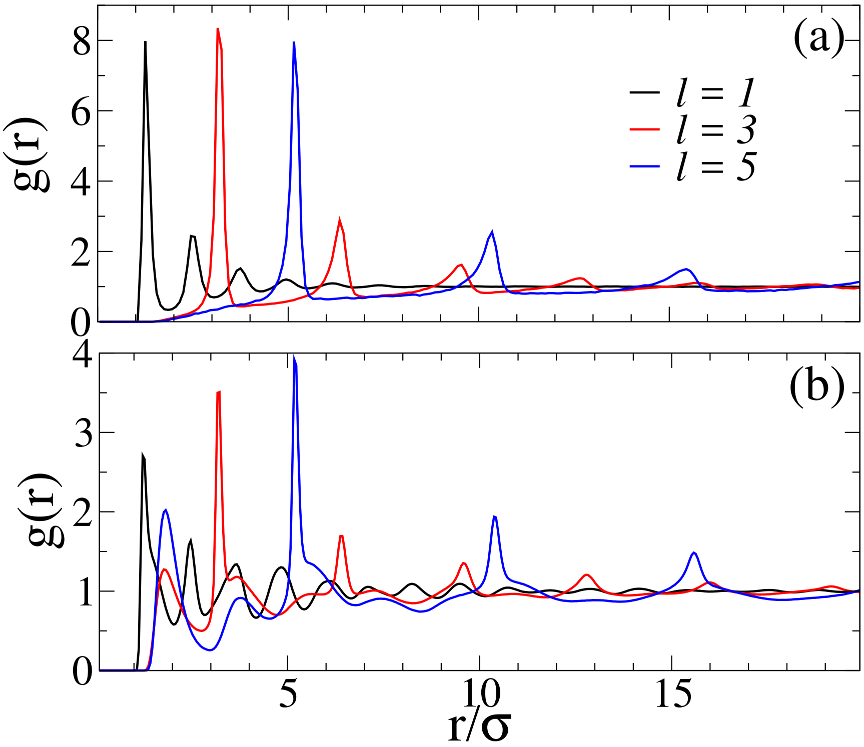

Figure 3.5: The pair correlation function for different aspect ratio and for (a) $\eta = 0.1$ and (b) $\eta = 0.4$.

In order to better understand the microstructure of the clusters, we calculate the angle correlation $f(\theta)$ among the first neighboring rods, defined as:

$$f(\theta) = \frac{1}{A}\left\langle \sum_{a} \sum_{b \neq a}^{N} \delta(\theta - \theta_{ab}) \right\rangle \qquad \text{for} \quad r_{ij} \leq \delta_c, \tag{3.12}$$

where $\theta_{ab} = \theta_a - \theta_b$ (see Fig. 3.1), $r_{ij} = |\mathbf{r}_i - \mathbf{r}_j|$ is the separation between dipole i and dipole j, and A is the normalization constant, defined as $A = \int_0^{\pi} f(\theta) d\theta$.

The function $f(\theta)$, Eq. (3.12), calculated for rods with distinct lengths and for different packing fractions is presented in Fig. 3.6. The rods are mostly connected to each other along the same direction, i.e., $f(\theta)$ is more pronounced around $\theta/\pi = 0$ and $\theta/\pi = 1$. The former trend reflects the head-to-tail or the parallel alignment, while the latter trend is related to the antiparallel arrangement. The larger the packing fraction the larger $f(\theta)$ is around $\theta/\pi = 1$. The angle correlation for $\theta = \pi$ as a function of the packing fraction η is shown in the inset of Fig. 3.6. As expected, the frequency of antiparalell arrangement increases with increasing η. The η dependence of $f(\theta)$ is qualitatively the same for distinct aspect ratios. The case $\theta = 0$ was not considered in the insets because it represents two kinds of arrangements, the parallel side-by-side and the parallel head-to-tail. In the next section, the side-by-side arrangement is discussed in more detail.

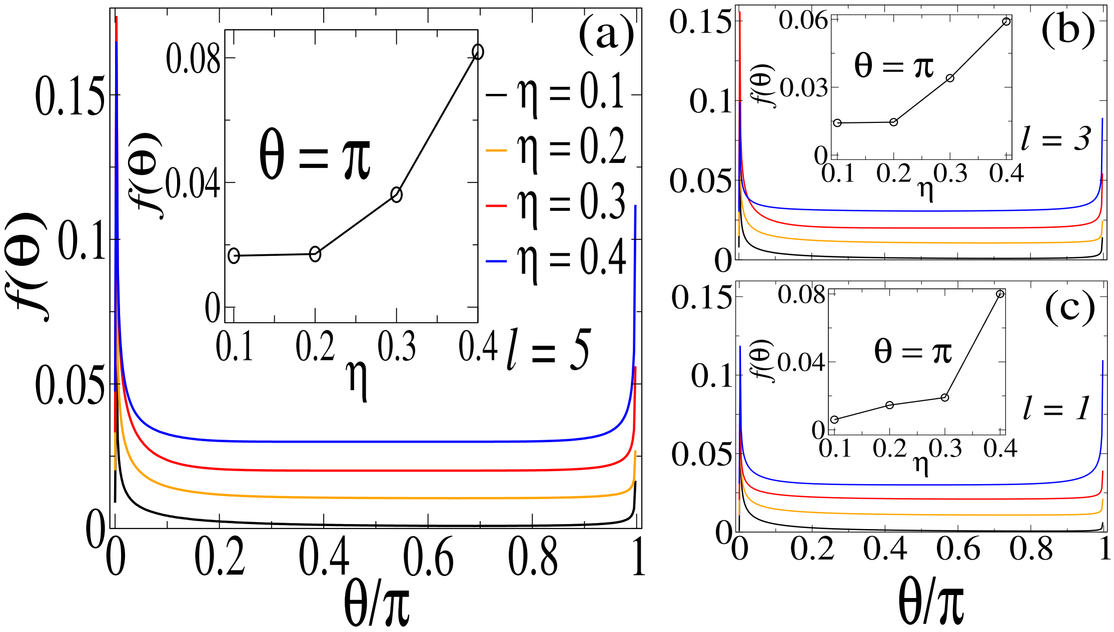

Figure 3.6: The angle correlation between the nearest neighboring particles for: (a) $l = 5$, (b) $l = 3$, (c) $l = 1$; and different values of η. Subsequent curves are shifted by 0.01 along the y axis in order to accentuate the small differences. The angle correlation for $\theta = \pi$ as a function of the packing fraction η is presented in the inset of each figure.

3.4 Connectivity properties

In this section we examine the connectivity properties of the self-assembled structures by studying the percolation transition, which is marked by the formation of an infinite cluster spanning over the system. Configurations are percolated when, accounting for periodic boundary conditions, one of the cluster forms a percolating path [62], i.e., the cluster is connected through the opposite borders of the simulation box. For systems with transient bonds the percolation transition is defined in the thermodynamic limit, where the average cluster size diverges [107]. For systems with a finite size of computational unit cell, the fraction of monomers in the largest cluster S_{max} can be taken as the order parameter [69, 70], namely:

$$S_{max} = \left\langle \frac{N_{\mathrm{larg}}}{N} \right\rangle, \tag{3.13}$$

where N_{larg} is the number of rods belonging to the largest cluster. For finite size systems, the percolation transition is well characterized when $S_{max} = 0.5$ [70]. Here, we evaluate S_{max} as a function of the packing fraction. Such an order parameter was considered in the study of the gelation transition [108, 69], which is related to the connectivity properties of the system. It has already been reported that $3D$ systems with elongated particles exhibit a percolation transition for lower density when their aspect ratio increases [95, 36].

In Fig. 3.7 we show the average size of the largest cluster (S_{max}) as a function of the packing fraction for $l = 1$, $l = 3$ and $l = 5$. S_{max} can be interpreted as the probability

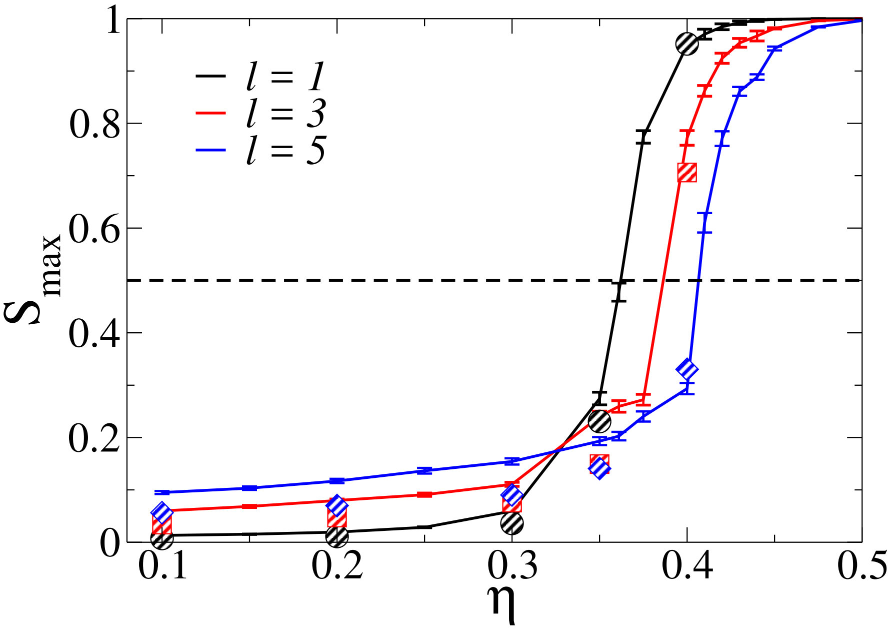

Figure 3.7: The average fraction of monomers in the largest cluster that is present in the ground state configuration as a function of packing fraction for different aspect ratio. The horizontal dashed line at 0.5 represents the percolation threshold. The results of the simulation for twice the number of particles in the computational unit cell is represented by symbols.

that one monomer belongs to the largest cluster. Notice that, the percolation transition is shifted to larger packing fraction with increasing l, which is opposite to what is found in $3D$ systems of elongated magnetic rods [36].

In order to better understand these results, we show in Fig. 3.8 the angle correlation [see Eq. (12)] excluding the parallel head-to-tail alignment, so that $\theta = 0$ ($\theta = \pi$) means parallel (antiparallel) arrangement of the bonded side-by-side rods. For low packing fraction ($\eta = 0.1$), a large diversity of possible alignments beyond the side-by-side arrangements are found [e.g., see also Fig. 3.4(b)]. However, a higher probability for side-by-side arrangement is found for larger η and larger l. For $l = 5$, the possible non-head-to-tail arrangements are mainly side-by-side arrangements, either parallel or antiparallel (see inset of Fig. 3.8). Note from Figs. 3.2(b)-(c) that the attractive well is wider and shallower in the antiparallel case (see Fig. 3.2(c)), which allows thermal fluctuations to break the clusters more easily, and make the largest cluster more unstable. In addition, the larger the aspect ratio, the harder it is for the rods to form large clusters in a head-to-tail arrangement. Since the percolated cluster is essentially characterized by head-to-tail bonds, such a condition is more difficult to realize for large l. As a consequence, the percolation transition is shifted to larger η when l increases. Although not shown, we find that the head-to-tail arrangement is also more stable than a parallel side-by-side arrangement.

Clusters that extend across the computational unit cell appear in Figs. 3.4(d) and 3.4(e). Note that the largest cluster almost extends over the whole system. In the head-

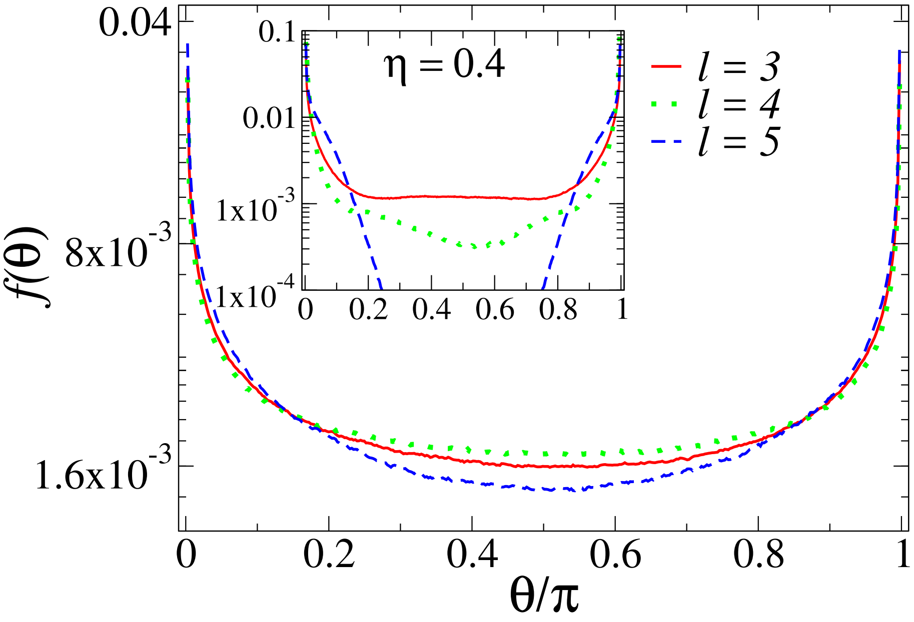

Figure 3.8: The angle correlation between the nearest neighboring rods excluding the parallel head-to-tail alignment for $\eta = 0.1$. Results for $\eta = 0.4$ are shown in the inset. In both cases the y axis is in log scale.

to-tail alignment, the rods form chains, which are, in some cases, curved or circular paths.

Now we study the dependence of the cluster size distribution $n(s)$ on the aspect ratio of the magnetic rods. In Fig. 3.9 we present the average cluster size distribution for $\eta = 0.4$. In general, $n(s)$ decreases with increasing cluster size. Close to percolation $n(s)$ develops a power-law dependence with exponent $\tau \simeq -2.05$, which is related to the random percolation prediction made for a $2D$ system ($\tau = -187/91 = -2.055$) [59] in the thermodynamic limit. Due to the finite size of the system considered in the simulations, percolated fluids exhibit a single peak for large s, comparable to the system size, and these states are denoted as random percolated [109, 63]. The $n(s)$ curves also confirm that the percolation transition for the system with larger aspect ratio takes place for larger η. The increase of the aspect ratio of the rods results in a stronger interaction between rods due to the addition of soft beads. Note that the case with $l = 5$ and $\mu^{*2} = 10$ is not percolated, while for $l = 1$ and $\mu^{*2} = 10$ it is percolated (Fig. 3.9). Each bead contributes with $\mu^* = \sqrt{10}$, to the net dipole moment of the rod, in order that, for $l = 5$ the net dipole moment is $\mu^*_{net} = 5\sqrt{10}$, or $\mu^{*2}_{net} = 250$. With these numbers ($l = 1$, $\mu^* = 10$ - percolated, and $l = 5$, $\mu^* = 250-$ not percolated) it is not clear whether the stronger interaction or the larger aspect ratio of the rods (or both effects) is relevant to prevent the formation of the percolated configuration. To check the importance of the interaction between rods in driving the percolation transition, we study the case in which the rods have aspect ratio $l = 1$ and $\mu^{*2} = 250$, for packing fraction $\eta = 0.4$, which is shown as inset in Fig. 3.9. Our findings indicate that, although the dipolar nature of the interaction is fundamental to the results found in the present study, since the percolation threshold for non-interacting

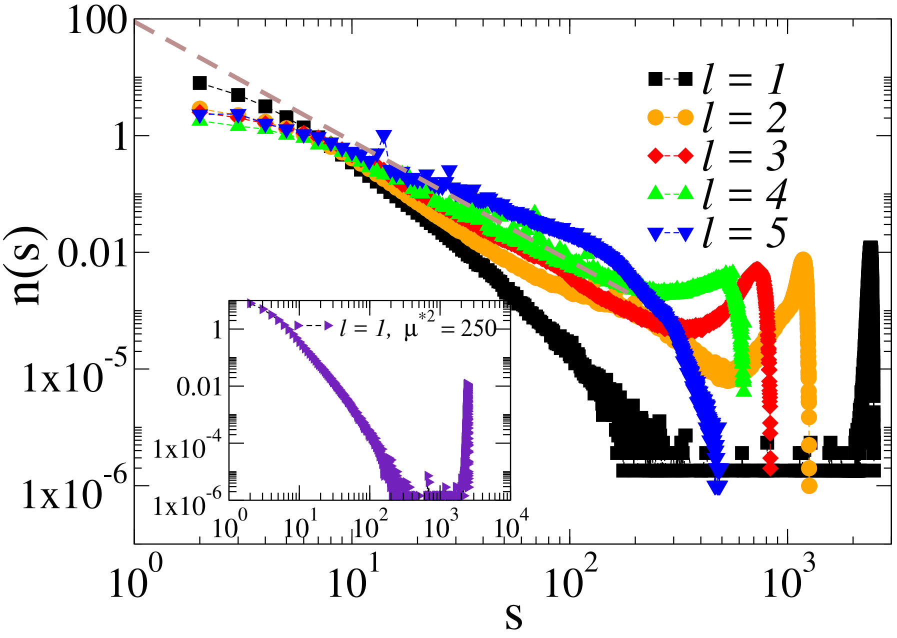

Figure 3.9: The cluster size distribution for $\eta = 0.4$, and different aspect ratios. The dashed line represents the function $n(s) \propto s^{-2.05}$. In the inset, the $l = 1$ case for $\mu^{*2} = 250$. Both axes are in log scale.

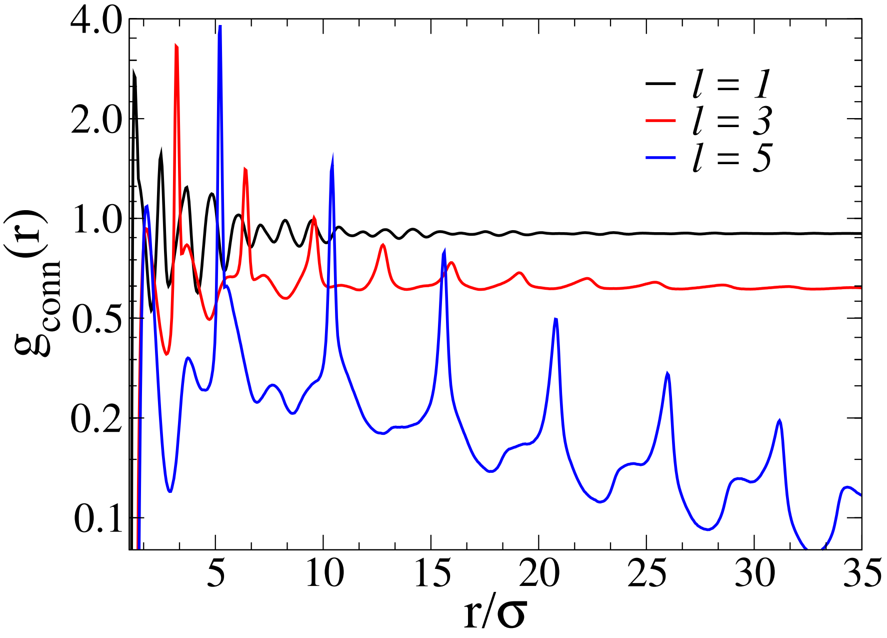

Figure 3.10: The pair connectedness function for different aspect ratio values for packing fraction $\eta = 0.4$. The y axis is in log scale.

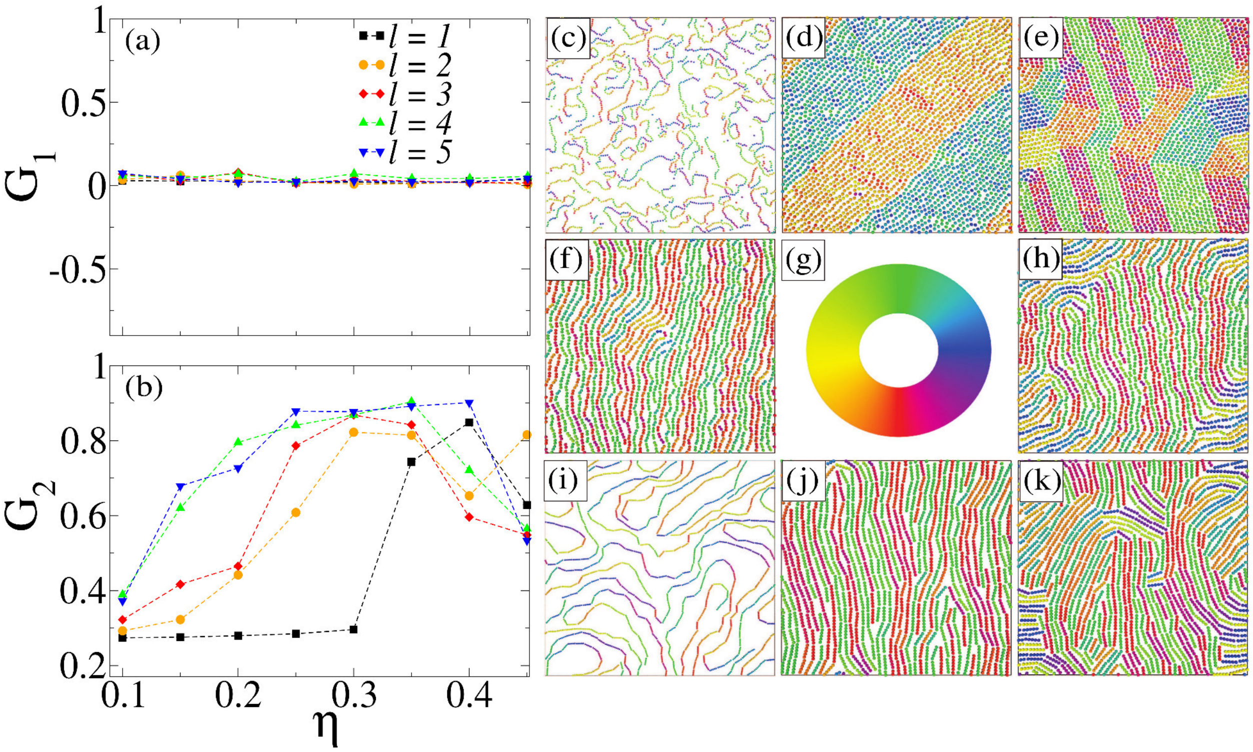

Figure 3.11: (a) The polarization and (b) the nematic order parameter for different aspect ratios as a function of the packing fraction. The orientations of some representative configurations are depicted in the right figures for $T^* = 0.1$ and for $l = 1$ with (c) $\eta = 0.1$, (d) $\eta = 0.4$, (e) $\eta = 0.45$ and for $l = 2$ with (f) $\eta = 0.4$, (h) $\eta = 0.45$ and for $l = 5$ with (i) $\eta = 0.1$, (j) $\eta = 0.4$; (l) $\eta = 0.45$. (g) The colors indicate the orientation of the dipoles in plane.

rigid rods in a two dimensional system decreases with increasing aspect ratio [110, 111], the geometric effect (aspect ratio and $2D$ confinement) is the determining factor that rules the connectivity behavior of the system. Another useful quantity to obtain information about percolation is the pair connectedness function $g_{conn}(r)$, which is defined as the conditional probability of finding a particle at a distance r from a particle located at the origin, connected via a sequence of bonds, i.e., within the same cluster [112]. In the limit when the whole system forms a single cluster, the pair connectedness function matches the pair correlation function [Eq. (3.11)].

In Fig. 3.10 we show $g_{conn}(r)$ for different aspect ratios and for packing fraction $\eta = 0.4$. For an infinite-size cluster, $g_{conn}(r)$ becomes different from zero in the limit $r \to \infty$. From what is presented in Figs. 3.7 and 3.9, percolation is suppressed when we increase the aspect ratio of the rods, so that for packing fraction $\eta = 0.4$ the $l = 1$ and $l = 3$ cases are percolated, while on the other hand, the $l = 5$ case is not. We see that such a behavior is also clearly reflected in $g_{conn}(r)$. The results presented in this section indicates that the dependence of the percolation transition on the packing fraction is mainly ruled by geometric effects.

3.5 Orientational Ordering

In this section we investigate the appearance of orientational order. $3D$ suspensions of passive rodlike particles in thermal equilibrium were found to be isotropic for low densities and nematic for high densities [98]. Here we investigate the occurrence of liquid-crystalline ordering in $2D$ by analyzing the ferromagnetic order parameter G_1, i.e., the polarization:

$$G_1 = \left\langle \frac{1}{N} \left| \sum_i^N \hat{\boldsymbol{\mu}} \cdot \hat{\boldsymbol{d}} \right| \right\rangle, \tag{3.14}$$

where N is the number of rods, $\hat{\boldsymbol{\mu}} = \boldsymbol{\mu}/|\boldsymbol{\mu}|$, and $\hat{\boldsymbol{d}}$ is the unit eigenvector related to the largest eigenvalue (G_2) of the following matrix:

$$\boldsymbol{Q_{kf}} = \frac{1}{2N} \sum_i^N (3\hat{\boldsymbol{\mu}}_k^i \hat{\boldsymbol{\mu}}_f^i - \delta_{kf}), \tag{3.15}$$

where i refers to particle i and the indexes k and f denote the cartesian components of the orientation vector. G_2 is also referred to as the orientational order parameter, i.e., the nematic order parameter [41]. As shown in Fig. 3.11(a), the polarization is negligible for any l, indicating that no ferromagnetic ordering is present. On the other hand, Fig. 3.11(b) indicates that an orientational order of the rod axes is present. As expected, an increase of the aspect ratio shifts the increase of G_2 towards lower packing fraction. In the case of a single dipole ($l = 1$) we observe a rather distinct isotropic-nematic transition as compared to the $l \neq 1$ cases. These results are consistent with the findings of Alvarez *et al.*[36], in the sense that a larger aspect ratio increases the stability of the nematic phase. However, we also find a non-monotonic behavior of the orientational ordering for high packing fraction due to the presence of magnetic bulk domains, which present local ferromagnetic order. Monte Carlo simulations of a corresponding 2D systems revealed frustrated structures characterized by large domains of local ferroelectric order, but no long-range order [113], which are consistent with the present study. In a $2D$ system at finite temperature, the nematic and smetic transition is not observed for long-range interaction [114, 115, 116, 117]. On the other hand, the magnetic dipolar interaction in $2D$ is short-range, in order that it is possible to observe such an isotropic-nematic transition [118, 119]. In Figs. 3.11(c-k) it is possible to observe the orientation of the rods for different configurations. In Fig. 3.11(e) a local hexagonal-order can be seen as a consequence of the fact that for low temperature and sufficiently high density the dipole-like colloids form crystalline structures (positional ordering). Such a local-hexagonal order of the corresponding 2D system at $T^* = 0.1$ was recently reported by Schmidle *et al.* [106]. An interesting lane-like configuration is shown in Fig. 3.11(d). Previously, a similar lane-formation for a binary mixture of particles driven against each other by an external field was predicted [120, 121]. The lane formation is an instability where, for strong enough driving forces, alike particles are driven to move behind each other in order to avoid collisions with oppositely driven particles. Similar structure was also reported for self-propelled particles [122, 118, 123]. In the present study, the lane-formation appears in a mono dispersive system as a nematic and an intermediate isotropic-hexagonal ordering transition of circular ($l = 1$) particles provided by the magnetic interaction, which makes particles in the different lanes distinct due to the opposite orientation of their dipoles.

3.6 Conclusions

In summary, we investigated a $2D$ system consisting of magnetic rods using MD simulations. Each rod was composed of soft beads having a central point-like dipole which interact via a DSS potential. This model was motivated by recent experimental [37] and theoretical [36] studies. Structural properties were investigated with particular attention to the dependence on the aspect ratio and the packing fraction. We considered aspect ratios ranging from $l = 1$ to $l = 5$.

The head-to-tail assembly was identified as the most energetically favorable for any aspect ratio. Such a configuration favors the formation of chain segments. However, the increase of the packing fraction was fundamental to observe other kinds of alignment as e.g. parallel and antiparallel arrangements of the dipoles. Given the preference of head-to-tail configurations and thus chain formation, we paid special attention to the appearance of a cluster extending over the whole system for sufficient large packing fraction (percolated cluster). Nevertheless, the side-by-side arrangement and the two-dimensional confinement suppresses the percolation transition for higher aspect ratio. Such a behavior is opposite to what was observed in $3D$ [95, 36]. This result should also be contrasted to an earlier study of a non-magnetic filament network system of rods and crosslinkers in which the percolation transition was independent of the filament length [70].

The transition to the isotropic-nematic phase was facilitated by the increase of the aspect ratio of the rods. However, the nematic behavior did not exhibit any monotonic behavior with respect to the packing fraction due to the presence of magnetic bulk domains at large η-values, characterized by local ferromagnetic order. Specifically, for $l = 1$, the nematic behavior in the bulk domain was followed by hexagonal-order which is expected in the limit of high density and low temperature.

The results shown in this work were obtained for low temperature ($T^* = 0.1$). For temperatures one order of magnitude smaller (higher) than the one considered here, $T^* = 0.1$, the percolation transition occurs at lower (higher) values of the packing fraction, as observed in Ref. [106]. For sufficiently high temperatures the clusters are destroyed, suppressing the percolation transition. A more detailed systematic study of the temperature dependence of the structural properties of the present study is left to future work.

4

Clustering and percolation properties of magnetic peapod-like rods with tunable directional interaction

Based on extensive Langevin Dynamics simulations we investigate the structural properties of a two-dimensional ensemble of magnetic rods with a peapod-like morphology, i.e, rods consisting of aligned single dipolar beads. Self-assembled configurations are studied for different directions of the dipole with respect to the rod axis. We found that with increasing misalignment of the dipole from the rod axis, the smaller the packing fraction at which the percolation transition is found. For the same density, the system exhibits different aggregation states for different misalignment. We also study the stability of the percolated structures with respect to temperature, which is found to be affected by the microstructure of the assembly of rods.

4.1 Introduction

Many efforts are currently devoted to the search of new functionalized particles in order to satisfy the constant need for materials with different properties. Recent advances in particle synthesis has resulted in a rapid growth of this field of material science. Colloids with directional interactions are promising candidates [124, 125, 126]. By tuning the direction, the self-assembling process can be controlled leading to the emergence of specific structures. A paradigm example are dipolar colloids whose interactions are governed by permanent or field-induced, magnetic or electric dipole moments, as well as particles with more complex multipolar interactions.

Nanoparticles (NP) with a magnetic mono-domain (MN), are a typical example with a wide range of applications, including magnetic fluids [15], biomedicine [16], Magnetic Resonance Imaging (MRI) [17], data storage [18], among others. Currently growing attention is being paid to magnetic particles with anisotropic shape, due to their more complex properties when compared to those with spherical shape, as for example magnetic birefringence [127] and thermal conductivity [31]. Beyond anisotropy in the shape of the particles, the same attention was also addressed to cases where the anisotropy is in the location of the dipole with respect to the center of symmetry of the particle. In recent theoretical works the structure of fluids containing spherical particles with embedded off-centered magnetic dipoles [128, 129] was investigated.

Beyond the nature of the interaction itself, the morphology of the NP can be used as a controlling parameter to functionalize the MN through the interaction direction, i.e. by tuning the dipole moment's direction of a peapod-like rigid rod. This is experimentally realised through the synthesis of monodisperse magnetoresponsive rods of desired diameter, length, and magnetic susceptibility [40].

Driven by the interest in the phase behavior of polar liquid crystals, earlier models of rod-like particles with a *single* longitudinal (or transversal) dipole moment have been intensively studied both by theory and numerical simulations [90, 91, 92, 93]. We present here a numerical study of the self-assembly of a two dimensional system of stiff peapod-like straight filaments, composed of single magnetic dipolar beads that are rigidly linked one by one. A similar system was studied earlier by experiment [37] and simulations [36, 130]. The interaction is given by the superposition of the dipolar fields of each dipole bead. Differently of our previous work [130], in this study the direction of the dipole moment is altered with respect to the rod axis, opening the possibility of a plethora of new kinds of assembled clusters. Many experiments involving assemblies of colloids are actually done at surfaces and/or thin films [131, 132, 133, 134, 88, 89], which motivates us to explore two dimensional ($2D$) systems.

We also study the connectivity properties of the present system by focusing on the percolation transition as a function of the direction of the dipole moment. The percolation transition is related to gelation in attractive-driven colloidal systems. Percolation behavior is also of great relevance in highly connected materials due to the possibility of enhancing the electrical and thermal conductivity [94, 37]. In addition, there is a relation with the change of the viscosity in systems with sufficient strong bond strength [135, 136].

The interaction strength may either increase or decrease the volume fraction required for percolation according to the definition of the separation at which two particles are considered to be connected, the dimensionality, and the proximity to the critical temperature [137]. As observed by Miller and Frenkel [138] for a system with adhesive hard spheres (AHS), the localization of the percolation threshold, the critical value of a given parameter where the percolation statistically happens, also depends on the interaction strength between particles, which is directly related with the temperature of the system. Therefore it is worth to explore possible routes under which the percolation transition is enhanced. Concerning the dimensionality, and, by using elongated particles, it was shown, in the $3D$ case, that an increase of the aspect ratio decreases the percolation threshold [95, 36], while the opposite behavior is observed in the $2D$ case [130]. In the present work we study the equilibrium configurations and the percolation transition as a function of the angular misalignment of the dipole moment with respect to the rod axis, and we show that larger values of this misalignment yields an enhancement of the percolation transition, i.e., an infinite extended cluster is formed for lower density.

The paper is organized as follows: our model system and simulation details are given in Sect. 2. The obtained different cluster configurations are presented in Sect. 3. The connectivity properties are discussed in Sect. 4. Our conclusions are given in Sect. 5.

4.2 Model and Simulation Methods

Extensive Langevin Dynamics simulations were performed to study a two-dimensional ($2D$) system consisting of typically, unless stated otherwise, $N = 840$ identical stiff rods of aspect ratio $l = 3$. The phase behavior of a mono-dispersed system with the same aspect ratio was recently studied [139] and is considered an established reference system [140]. For suspensions studied experimentally, the aspect ratio $l = 3$ is in the lowest accessible limit [141]. The magnetic nature of the rod is simulated by attaching a point dipole of permanent magnetic moment μ at the center of each bead (see Fig. 4.1). The orientation of the dipoles with respect to the axial direction of the rod is given by the angle Ψ, as illustrated in Fig. 4.1. To model the dipolar particles we use a dipolar soft sphere (DSS) potential [130], consisting of the repulsive part of the Lennard-Jones (LJ) potential u^{rep} and a point-like dipole-dipole interaction part u^D. The total interaction energy between rods a and b is the sum of the pair interaction terms between their respective dipolar

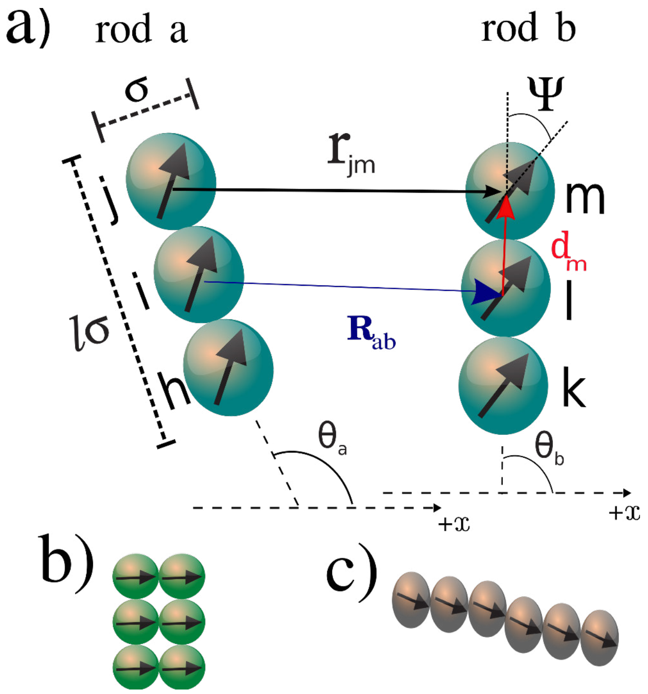

Figure 4.1: Schematic illustration of the interaction between two magnetic rods with: a) indication of the important parameters of the pair interaction potential; b) ribbon-like arrangement; c) head-to-tail arrangement.

spheres (DS)

$$U_{a,b}(\mathbf{R}_{a,b},\theta_a,\theta_b)=\sum_{j\neq m}u_{j,m}, \tag{4.1}$$

$$u_{j,m}=u^{rep}(\mathbf{r}^{a,b}_{jm})+u^{D}(\mathbf{r}^{a,b}_{jm},\boldsymbol{\mu}^a_j,\boldsymbol{\mu}^b_m), \tag{4.2}$$

where

$$u^{rep} \;=\; 4\epsilon\left(\frac{\sigma}{r_{jm}}\right)^{12}, \tag{4.3}$$

$$u^{D} \;=\; \frac{\boldsymbol{\mu}_j\cdot\boldsymbol{\mu}_m}{r^3_{jm}}-\frac{3(\boldsymbol{\mu}_j\cdot\mathbf{r}_{jm})(\boldsymbol{\mu}_m\cdot\mathbf{r}_{jm})}{r^5_{jm}}, \tag{4.4}$$

with σ the diameter of each bead, and ϵ is the LJ soft-repulsion constant, $\mathbf{R}_{a,b}=\mathbf{R}_b-\mathbf{R}_a$ is the vector which connects the center of rod b with the center of rod a. The orientation of rods a and b are given by θ_a and θ_b, respectively. The vector $\mathbf{r}^{a,b}_{jm}$ connects the center of bead m of rod b with the center of bead j of rod a (see Fig. 4.1). The force on bead m due to bead j is given by

$$\mathbf{f}_{jm}=-\boldsymbol{\nabla}u_{jm}. \tag{4.5}$$

The torque on bead m is [130]

$$\boldsymbol{\tau}_m=\boldsymbol{\mu}_m\times\sum_{m\neq j}\mathbf{B}_{jm}+\mathbf{d}_m\times\sum_{m\neq j}\mathbf{f}_{jm}, \tag{4.6}$$

where $\mathbf{d}_m$ is the vector connecting the center of bead m (rod b) with the center of rod b as illustrated in Fig. 4.1, and $\mathbf{B}_{jm}$ is the magnetic field generated by the dipole moment μ_j at the position of the dipole μ_m, which is given by

$$\mathbf{B}_{jm}=\frac{3(\boldsymbol{\mu}_m\cdot\mathbf{r}_{jm})\mathbf{r}_{jm}}{r^5_{jm}}-\frac{\boldsymbol{\mu}_m}{r^3_{jm}}. \tag{4.7}$$

The summations in Eq. (4.6) are considered only for dipoles belonging to distinct rods. The orientation of the rods is given by the unitary vector $\mathbf{s}$ given by $\mathbf{s}=\mathbf{d}_m/\mid\mathbf{d}_m\mid$. As the dipole moment is misaligned by Ψ, the total torque in a rod b is

$$\mathbf{N}_b=\sum_{m}^{l}\boldsymbol{\tau}_m=\sum_{m}^{l}\left(\hat{\boldsymbol{\mu}}_m\times\underbrace{\sum_{m\neq j}\mu_m\boldsymbol{B}_{jm}}_{\mathbf{G}'}+\hat{\boldsymbol{s}}_m\times\underbrace{\sum_{m\neq j}d_m\boldsymbol{f}_{jm}}_{\mathbf{G}''}\right) \tag{4.8}$$

where $\hat{\boldsymbol{\mu}}=\boldsymbol{\mu}/|\boldsymbol{\mu}|$ and revisiting Eq. (2.12)

$$I\dot{\boldsymbol{\omega}}=\hat{\boldsymbol{\mu}}\times\mathbf{G}'+\mathbf{s}\times\mathbf{G}'', \tag{4.9}$$

$$\mathbf{u}=\boldsymbol{\omega}\times\mathbf{s}, \tag{4.10}$$

where orientation is defined by $\mathbf{s}$, the unit vector along the major rod axis, $\mathbf{u}=d\mathbf{s}/dt$. Doing the derivative of Eq. (4.10) with respect to the time

$$\boldsymbol{\alpha}=\dot{\boldsymbol{\omega}}\times\mathbf{s}+\boldsymbol{\omega}\times\mathbf{u}. \tag{4.11}$$

From Eq. (4.9) we have

$$\boldsymbol{\alpha} \;=\; I^{-1}(\hat{\boldsymbol{\mu}} \times \mathbf{G}' + \mathbf{s} \times \mathbf{G}'') \times \mathbf{s} + \boldsymbol{\omega} \times \boldsymbol{\omega} \times \mathbf{s}. \tag{4.12}$$

Using the identity of Eq. (A38), we find

$$\begin{aligned} \boldsymbol{\alpha} &= I^{-1}[(\mathbf{G}'' - \mathbf{s}(\mathbf{G}'' \cdot \mathbf{s})) + \mathbf{G}' \underbrace{(\hat{\boldsymbol{\mu}} \cdot \mathbf{s})}_{\cos\Psi} - \hat{\boldsymbol{\mu}}(\mathbf{s} \cdot \mathbf{G}')] + \boldsymbol{\omega} \underbrace{(\boldsymbol{\omega} \cdot \mathbf{s})}_{0} - \mathbf{s} \underbrace{(\boldsymbol{\omega} \cdot \boldsymbol{\omega})}_{\omega^2}, && (4.13) \\ &= I^{-1}[(\mathbf{G}'' - \mathbf{s}(\mathbf{G}'' \cdot \mathbf{s})) + \mathbf{G}' \underbrace{(\hat{\boldsymbol{\mu}} \cdot \mathbf{s})}_{\cos\Psi} - \hat{\boldsymbol{\mu}}(\mathbf{s} \cdot \mathbf{G}')] - \mathbf{s}\omega^2. && (4.14) \end{aligned}$$

As $\boldsymbol{\omega} = \omega\hat{z}$ and $\mathbf{s} = s_x\hat{x} + s_y\hat{y}$ [see Eq. (2.18)]

$$\begin{aligned} \mathbf{u} \cdot \mathbf{u} &= (\boldsymbol{\omega} \times \mathbf{s}) \cdot (\boldsymbol{\omega} \times \mathbf{s}), \\ &= [\omega\hat{z} \times (s_x\hat{x} + s_y\hat{y})] \cdot [\omega\hat{z} \times (s_x\hat{x} + s_y\hat{y})], \\ &= \omega^2 s_x^2 + \omega^2 s_y^2 = \omega^2 \underbrace{(s_x^2 + s_y^2)}_{1} = \omega^2. && (4.15) \end{aligned}$$

Thus

$$\boldsymbol{\alpha} = I^{-1}[(\mathbf{G}'' - \mathbf{s}(\mathbf{G}'' \cdot \mathbf{s})) + \mathbf{G}' \underbrace{(\hat{\boldsymbol{\mu}} \cdot \mathbf{s})}_{\cos\Psi} - \hat{\boldsymbol{\mu}}(\mathbf{s} \cdot \mathbf{G}')] - \mathbf{s}(\mathbf{u} \cdot \mathbf{u}). \tag{4.16}$$

The translational and rotational Langevin equations of motion of rod b with mass M_b and moment of inertia I_b, are given by

$$M_b \frac{d\mathbf{v}_b}{dt} = \mathbf{F}_b - \Gamma_T \mathbf{v}_b + \boldsymbol{\xi}_b^T(t), \tag{4.17}$$

$$I_b \frac{d\boldsymbol{\omega}_b}{dt} = \mathbf{N}_b - \Gamma_R \boldsymbol{\omega}_b + \boldsymbol{\xi}_b^R(t), \tag{4.18}$$

where $\mathbf{v}_b = d\mathbf{R}_b/dt$, $\boldsymbol{\omega}_b$ is the angular velocity, $\mathbf{F}_b$ and $\mathbf{N}_b$ are the total force and torque acting on rod b, respectively, while Γ_T and Γ_R are the translational and rotational friction constants. $\boldsymbol{\xi}_b^T$ and $\boldsymbol{\xi}_b^R$ are the Gaussian random force and torque, respectively, which obey the following white noise conditions:$\langle \boldsymbol{\xi}_b^\alpha(t) \rangle = 0$, $\langle \boldsymbol{\xi}_b^\alpha(t) \cdot \boldsymbol{\xi}_{b'}^\alpha(t') \rangle = 2\Gamma_\alpha k_B T \delta_{bb'} \delta(t - t')$, $\alpha = T, R$. For rod-like particles, the translational friction constant is a combination of the parallel and perpendicular components with respect to the rod axis, so that the total translational diffusion coefficient is $D_T = \frac{1}{3}(D_\parallel + 2D_\perp)$ for $D_\perp = \frac{1}{2}D_\parallel$ [73]. However, since the dynamical properties are not studied in the present work, for equilibrium simulations the values of Γ_T as well as Γ_R are irrelevant. We introduce the ratio $\Gamma_T/\,\Gamma_R = 4/3$ because such a ratio is already known to produce fast relaxation to equilibrium in similar systems [73]. As a consequence, by applying Velocity Verlet integration method, the equations of motion for the rod's CM are

$$\begin{aligned} \mathbf{R}_b(t + \delta t) &= \mathbf{R}_b(t) + \left(1 - \Gamma_T \frac{\delta t}{2}\right) \mathbf{v}_b(t)\delta t + \left(\mathbf{F}_b(t) + \sqrt{\frac{2k_B T \Gamma_T}{\delta t}}\, \hat{\boldsymbol{\xi}}_T(t)\right) \frac{\delta t^2}{2M_b}, \\ \mathbf{v}_b(t + \delta t) &= \frac{1}{1 + \frac{\Gamma_T \delta t}{2}} \left[\mathbf{v}_b \left(t + \frac{\delta t}{2}\right) \left(\mathbf{F}_b(t + \delta t) + \sqrt{\frac{2k_B T \Gamma_T}{\delta t}}\, \hat{\boldsymbol{\xi}}_T(t + \delta t)\right) \frac{\delta t}{2M_b}\right], \end{aligned} \tag{4.19}$$

and for rotational motion, we have

$$\begin{aligned}
\mathbf{s}(t+\delta t) &= \mathbf{s}(t) + \left(1 - \Gamma_R \frac{\delta t}{2}\right)\mathbf{u}(t)\delta t + \left(\boldsymbol{\alpha}(t) + \sqrt{\frac{2k_B T \Gamma_T}{I_b \delta t}}\hat{\boldsymbol{\xi}}_R(t) \times \mathbf{s}(t)\right)\frac{\delta t^2}{2}, \\
\mathbf{u}(t+\delta t) &= \frac{1}{1+\frac{\Gamma_R \delta t}{2}}\left[\mathbf{u}\left(t+\frac{\delta t}{2}\right) + \left(\boldsymbol{\alpha}(t+\delta t) + \sqrt{\frac{2k_B T \Gamma_R}{I_b \delta t}}\hat{\boldsymbol{\xi}}_R(t+\delta t) \times \mathbf{s}(t+\delta t)\right)\frac{\delta t}{2I_b}\right],
\end{aligned} \tag{4.20}$$

where $\hat{\boldsymbol{\xi}}_T$ and $\hat{\boldsymbol{\xi}}_R$ are a dimensionless stationary Gaussian unitary vectors (see Sec. 2.2.2) for translation and for rotation, respectively, evaluated by the Box-Muller procedure [142]. We define the reduced unit of time as $t^* = t/\sqrt{\epsilon^{-1}M\sigma^2}$, where M is the mass of the rod. The energy is given in reduced units as $U^* = U/\epsilon$, the dipole moment in dimensionless units as $\mu^* = \mu/\sqrt{\epsilon\sigma^3}$, and the dimensionless distances as of $r^* = r/\sigma$. Unless stated otherwise, the ratio of the thermal energy to the soft-sphere repulsion constant is chosen to be $k_BT/\epsilon = 0.1$, where ϵ/k_B is the temperature unit and k_B is the Boltzmann constant. Periodic boundary conditions are taken in both spatial directions. Since the dipolar pair interaction falls off as (r^{-3}), we take the simulation box sufficiently large such that no special long-range summation techniques [41] are needed. We define the packing fraction as $\eta = N_{beads}\pi(\sigma/2)^2/L^2$, where $N_{beads} = 2520$ is the total number of dipolar beads of the system and L^2 is the simulation box area. Since $N_{beads} = lN$, we can rewrite the packing fraction as $\eta = \rho^* l\pi/4$, where ρ^* is the dimensionless density $\rho^* = \rho\sigma^2$, and $\rho = N/L^2$. The reduced time step is typically in the range $\delta t^* = 10^{-4} - 10^{-3}$.

All simulations are performed at a very slow cooling rate. Initially, we set the temperature at $k_BT/\epsilon = 2$ and slowly reduced it in steps $\Delta k_BT/\epsilon = 0.05$, each 5×10^5 time steps, till the final temperature is reached. The quantities of interest are then averaged over more than 10^6 time steps. All the beads from all rods have the same dipole moment whose magnitude we set as $\mu^* = 1$. Common experimental values of μ^{*2} at room temperature ranges in the interval $0.1 \leq \mu^{*2} \leq 10$. For example, in experiments [101] carried out using aqueous dispersions of superparamagnetic microspheres of ferrite grains (Estapor (R) from Merck - reference M1- 030/40) for $r \approx 205\ nm$ and $M_s \approx 6 \times 10^4\ A/m$, the magnetization (M) of the particles is completely reversible and adjustable by an external magnetic field. If we consider $T = 293\ K$ and $M \approx 22,6\%$ of M_s, we obtain $\mu^* \approx 1$.

4.3 Results and Discussion

4.3.1 Cluster Formation

We first present the dependence of the DSS pair interaction potential on the separation between rods. The study of the pair interaction potential is needed in order to understand the nature of the resulting many-body interaction and to help us to set the values of the useful parameters that help to understand the self-assembled structures. The dependence

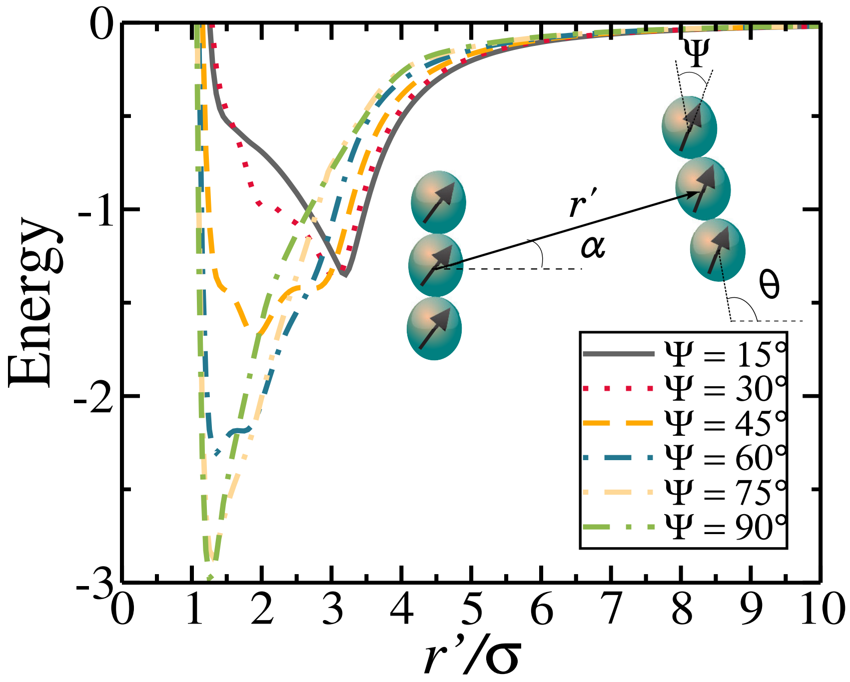

Figure 4.2: The pair interaction energy as a function of interrod separation ($\mathbf{r}'$) minimized with respect to $\boldsymbol{\alpha}$ and $\boldsymbol{\theta}$.

of the DSS pair interaction potential as a function of the separation between rods and minimized with respect to some characteristic angles is presented in Fig. 4.2. Rather different potential profiles are obtained with changing values of Ψ. For low values of Ψ ($\leq 30°$) the minima are located at $r'/\sigma \approx 3$, which corresponds to the aspect ratio of the rods. The values of α and θ which minimize the pair-interaction energy indicate that rods are favourably in the head-to-tail bond. As Ψ is increased the position of the global minimum is displaced to smaller values of r'/σ, suggesting that the head-to-tail bond disappears, giving rise to the ribbon-like bond configuration (see Fig. 4.1). Ribbon-like configurations are defined here as a side-by-side assembly as a consequence of the head-to-tail tendency of alignment between dipoles of beads in different rods and which are sufficiently displaced from the axial direction ($\Psi > 45°$). Similar ribbon-like configurations were very recently observed for microscopic magnetic ellipsoids [38, 34], and in peanut-shaped colloids [39]. For $\Psi = 45°$ we have a mixing of head-to-tail and ribbon-like arrangements with intermediate bonding energy and separation.

In order to find the separation (δ_c) used as a definition when two rods are bonded, we analyze the interrod separation related to the minimal energy value. From Fig. 4.2, we observe that the largest interrod separation related to the global minimum is located around $\approx 3.4\sigma$ for $\Psi = 15°$ and 1.4σ for $\Psi = 90°$. In the former the rods are in the head-to-tail arrangement, while in the latter they are in the ribbon-like configuration. In both cases, the shortest separation between beads of different rods is $\approx 1.4\sigma$ (bead-to-bead center distance). Therefore, we define here that two rods are bonded if the shortest separation between them is $\leq 1.4\sigma$.

Since the attraction between magnetic rods becomes stronger for larger Ψ (Fig. 4.2), we expect that the ribbon-like configurations will become more stable, implying that the formation of clusters is facilitated in the many-body case. To show that this is indeed the case, we analyze the degree of polymerization [58], defined as

$$\Phi = \left\langle \frac{N_c}{N} \right\rangle , \tag{4.21}$$

where N_c is the number of clustered rods and N is the total number of rods.

The polymerization as a function of the packing fraction η for different Ψ is presented in Fig. 4.3. There is a clear distinction of η-dependence of the polymerization for distinct values of Ψ. For $\Psi \leq 30°$ the polymerization increases with increasing η, while for $\Psi > 30°$, the value of Ψ does not change as η is increased. In principle we would expect that the tendency for aggregation should be stronger as η is increased. However, such a behavior is found only when $\Psi \leq 30°$, where the head-to-tail arrangement is mostly observed. For $\Psi = 45°$, the configurations are a mixture of head-to-tail and ribbon-like arrangements (minimum energy at $r/\sigma \approx 2$, Fig. 4.2) and the polymerization does not change significantly as η is changed. On the other hand, the larger Ψ, the larger is Φ, since, based on the minimized pair interaction function (Fig. 4.2), there is an increase of interrod attraction specially when the rods form a ribbon-like arrangement. For $\Psi \geq 60°$, the value of Φ does not change as Ψ is increased, and all the rods are connected to each other mostly arranged in the ribbon-like arrangement as the minimum energy is found for $r/\sigma \approx 1.4$.

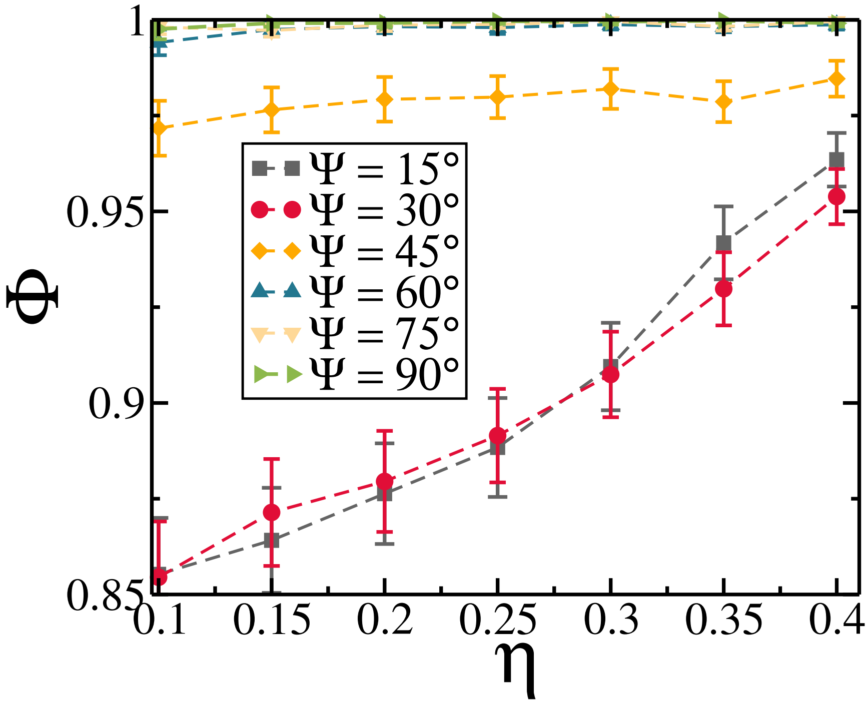

Figure 4.3: The polymerization as a function of the packing fraction η for different Ψ.

Some representative equilibrium configurations are presented in Fig. 4.4 for packing fraction $\eta = 0.1$ and $\eta = 0.3$, and distinct Ψ. We observe that the head-to-tail arrangements are found for $\Psi = 15°$ and $\Psi = 30°$, while the ribbon-like configurations are observed for $\Psi = 60°$ and $\Psi = 90°$. Such arrangements of the rods can be better characterised by computing the pair correlation function [8]

$$\mathbf{g}(\mathbf{r}) = \frac{\left\langle \sum_a \sum_{b \neq a}^{N} \delta(r - R_{ab}) \right\rangle}{2N\pi r \rho^*}, \tag{4.22}$$

where R_{ab} is the separation between the center of the rods a and b (see Fig. 4.1).

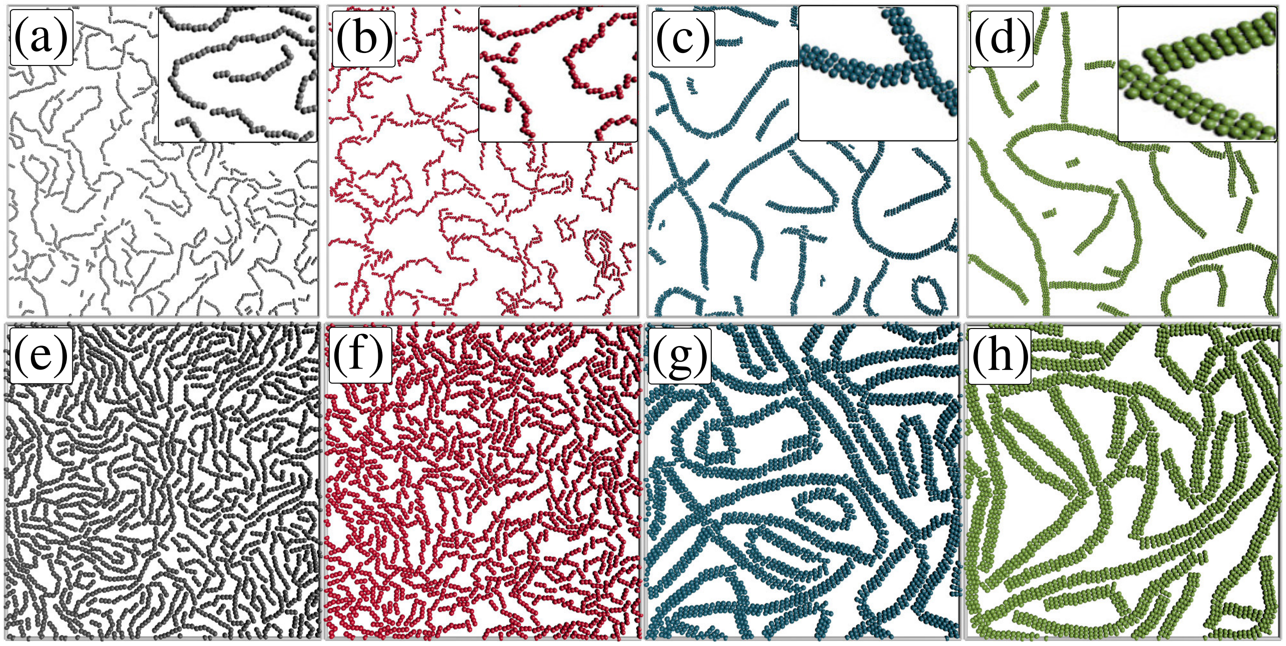

Figure 4.4: Some representative equilibrium configurations for $k_BT/\epsilon = 0.1$ and packing fraction $\eta = 0.1$ with (a) $\Psi = 15°$; (b) $\Psi = 30°$; (c) $\Psi = 60°$; (d) $\Psi = 90°$; and for $\eta = 0.3$ with (e) $\Psi = 15°$; (f) $\Psi = 30°$; (g) $\Psi = 60°$; (h) $\Psi = 90°$. The insets are enlargments of part of the structures.

We present in Fig. 4.5 the pair correlation function for $\eta = 0.1$ and for different values of Ψ. As shown, the position of the peaks changes towards smaller r for larger Ψ. For $\Psi = 15°$ and $\Psi = 30°$ the first largest peak is at $r/\sigma \approx 3$, which coincides with the value of the aspect ratio of the rods and is associated with the head-to-tail alignment. When Ψ increases, multiple peaks proportional to $r/\sigma \leq 3$ are found, and this is a consequence of the tendency to form side-by-side arrangements, e.g., for $\Psi \geq 60°$ the first largest peak is at $r/\sigma \approx 1.4$. For intermediate values of the first largest peak position, i.e. $r/\sigma \approx 2$ for $\Psi = 45°$, is a consequence of the mixed structures of head-to-tail and ribbon-like alignments, as expected by the pair interaction in Fig. 4.2. For $\Psi \leq 45°$ the $g(r)$ does not maintain a constant structure and it loses the long-range correlation, which is a typical behavior of liquid-like structures. On the other hand, for $\Psi \geq 60°$ the $g(r)$ has regular peaks and long-range correlation, which is a typical behavior of solids. These results indicate, qualitatively, that the system goes from a liquid-like configuration ($\Psi \leq 45°$) to a solid-like ribbon-like configuration ($\Psi \geq 60°$), as a consequence of the fact that the attraction between rods in the ribbon-like configuration is much stronger than that observed in the linear head-to-tail arrangement, see Fig. 4.2. In addition, such ribbon-like arrangements are expected to be more stable against thermal fluctuations.

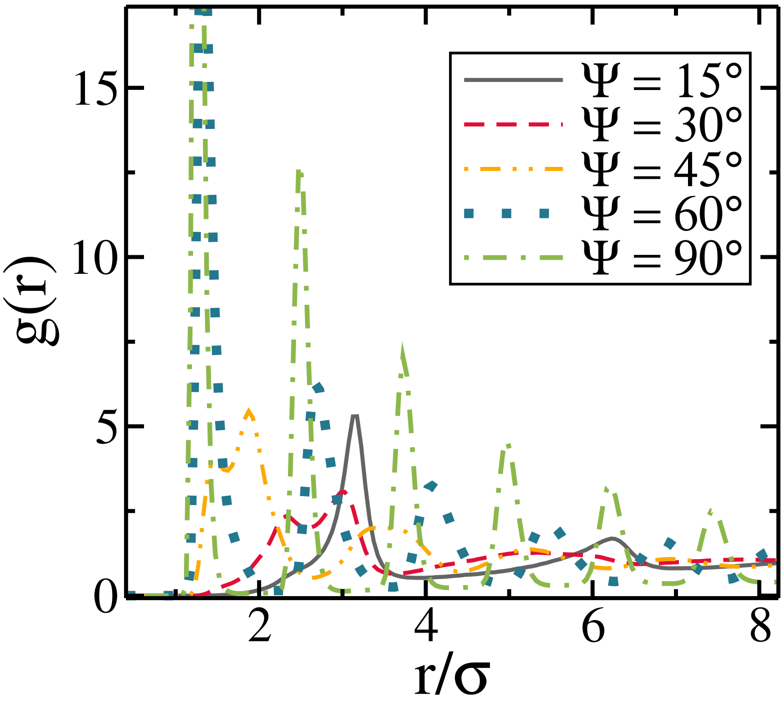

Figure 4.5: The pair correlation function for different values of Ψ with $\eta = 0.1$.

4.3.2 Connectivity Properties

Now we discuss the connectivity properties of the self-assembled structures. We focus our analysis on the study of the formation of percolated aggregates, which are defined as infinite connected clusters spanned over the system. The percolation transition is defined in the thermodynamic limit, where the average cluster size diverges [107]. We say that a configuration is percolated when, accounting for periodic boundary conditions, there is a percolating path [62], i.e., a cluster connected through opposite borders of the simulation box. A common feature of systems consisting of interacting particles subject to thermal fluctuations is that their bonds are transient. For low temperature, the lifetime of the bonds is sufficiently long, and the clusters are well defined over time. In our simulations, the temperature is one order of magnitude smaller than the average pair-interaction energy between rods, and the clusters are rather stable. In order to characterize the formation of the percolated clusters, we calculate an order parameter [69, 70] defined as the fraction of monomers in the largest clusters, S_{max}, i.e.

$$S_{max} = \left\langle \frac{N_{larg}}{N} \right\rangle, \tag{4.23}$$

where N_{larg} is the number of rods belonging to the largest cluster. Previous studies showed that for finite size systems, the percolation transition is well characterized when the size of the largest cluster is at least 50% of the total number of particles, i.e., $S_{max} = 0.5$ [69, 70]. Such an order parameter is useful to study the connectivity properties of the system, specially gelation [108, 69]. Here, we evaluate S_{max} as a function of the packing fraction and the orientation of the dipole moments with respect to the axial direction of the rod. S_{max} as a function of the packing fraction is presented in Fig. 4.6(a) for different Ψ. The percolation transition is shifted towards smaller packing fraction with increasing Ψ, due to the stronger attraction between rods observed in these cases. As a consequence, the emergence of ribbon-like structures is facilitated. This is shown more clearly in Fig. 4.6(b), where S_{max} is presented as a function of Ψ for different packing fractions. In all cases S_{max} increases with increasing Ψ, indicating that the rods interact more attractively, facilitating the formation of larger clusters. For small enough η ($\lesssim 0.1$) there is no formation of an infinite cluster independent of Ψ. Also, we observe that S_{max} saturates for $\Psi \gtrsim 75°$. The small η ($\lesssim 0.1$) and the tendency to form ribbons, which make the chains of the rods shorter in length, are the reasons for the absence of the extended clusters.

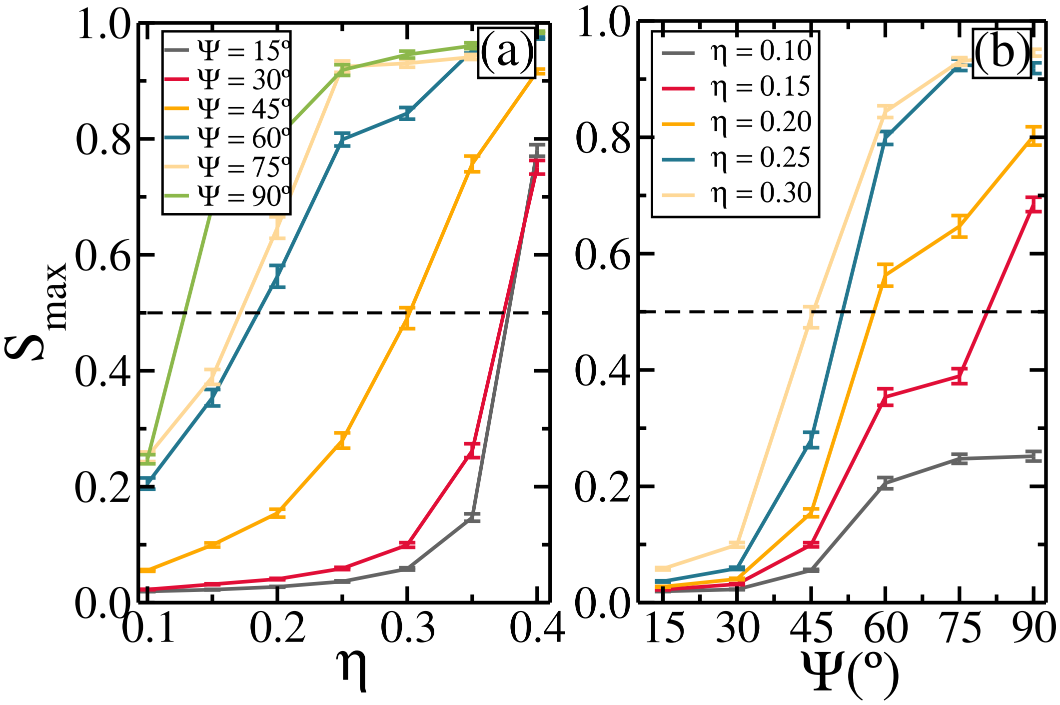

Figure 4.6: The average fraction of monomers in the largest cluster: (a) as a function of the packing fraction for different Ψ and (b) as a function of Ψ for different packing fractions. The horizontal dashed line at 0.5 refers to the percolation threshold.

The connectivity properties can also be studied by the analysis of the cluster size distribution $n(s)$, where s is the size of the cluster, i.e. the number of rods belonging to the cluster. In Fig. 4.7 we present the average cluster size distribution for different Ψ with $\eta = 0.2$ [Fig. 4.7(a)] and $\eta = 0.4$ [Fig. 4.7(b)]. In general, $n(s)$ decreases with increasing cluster size. The percolated configuration exhibits a single peak for large s, comparable to the system size, due to the finite size of the system considered in the simulations, and these states are denoted as random percolated [109, 63]. For $\eta = 0.2$, the system is percolated for $45° < \Psi \leq 60°$ (see Fig. 4.6(b)). Close to percolation ($\Psi \simeq 45°$) the $n(s)$ curve presents a power law dependence, $n(s) \propto s^{\tau}$, with exponent $\tau \simeq -2.05$, which is related to the well-known $2D$ random percolation prediction[59]($\tau = -187/91 \simeq -2.05$)

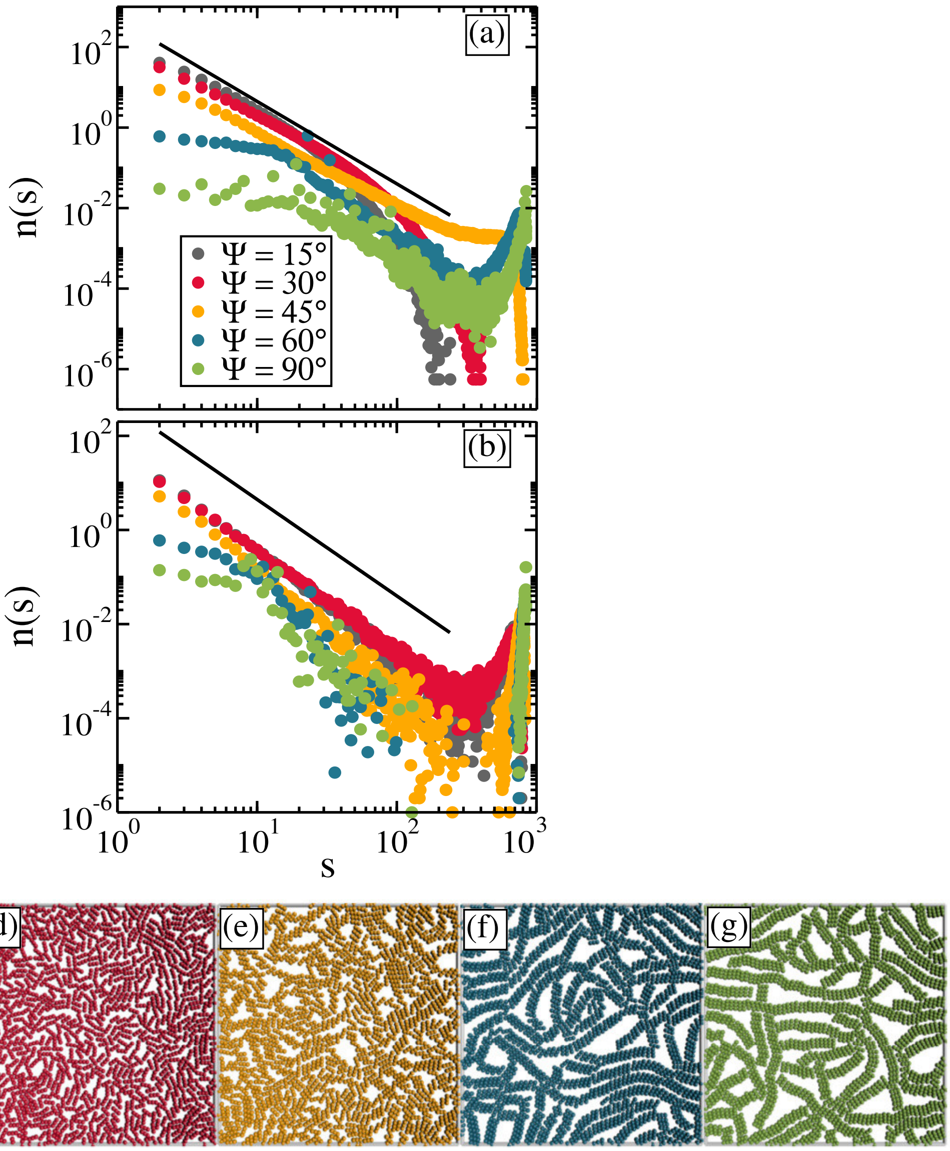

Figure 4.7: The cluster size distribution for different Ψ with (a) $\eta = 0.2$ and (b) $\eta = 0.4$. The solid line represents the function $n(s) \propto s^{-2.05}$. Axes are in log scale. Equilibrium configuration at $\eta = 0.4$ and for: (c) $\Psi = 15°$; (d) $\Psi = 30°$; (e) $\Psi = 45°$; (f) $\Psi = 60°$; (g) $\Psi = 90°$.

valid in the thermodynamic limit. Similar random percolated structures were found in Langevin Dynamics of functionalized colloids [143]. For $\eta = 0.4$, a similar s-dependence for $n(s)$, also with $\tau \simeq -2.05$, is found for $\Psi \simeq 30°$, where the rods aggregate together through head-to-tail bonds, similar as shown in Fig. 4.1(c). In both, $\eta = 0.2$ and $\eta = 0.4$, a similar power law dependence $n(s) \propto s^{\tau}$ is observed, but with different mechanism. For $\eta = 0.2$, the rods aggregate to each other through head-to-tail bonds and the chains of rods start to merge into one another in a random way. For $\eta = 0.4$, the rods are connected to each other as ribbon-like arrangements forming long chains, which, in turn, are randomly bonded to each other. The $n(s)$ curves also confirm that the percolation transition for the system with larger Ψ takes place for smaller η.

Another way to characterize the percolated structures is through the pair connectedness function $g_{conn}(r)$, defined as the conditional probability of finding a pair of particles separated by a distance r, both connected via a sequence of bonds, i.e., within the same cluster [112]. When an infinite cluster is present $g_{conn}(r)$ remains finite on every length scale. On the other hand, when a non-percolated structure is formed, we have $g_{conn}(r) \to 0$ for finite distances. A theory of the pair connectedness function has been previously developed for fluids as well as for lattice systems when the presence of physical clusters of particles in the system is explicitly taken into account [144]. In the limit when the whole system forms a single cluster, the pair connectedness function matches the pair correlation function [Eq. (4.3.1)].

In Figs. 4.8(a) and 4.8(b) we show the pair connectedness function $g_{conn}(r)$ for packing fraction $\eta = 0.2$ and $\eta = 0.4$, respectively, and different values of Ψ. An infinite-size percolated cluster is observed when g_{conn} assumes non-zero values in the limit $r \to \infty$, otherwise the cluster is not percolated. As can be observed the results are in agreement with those obtained through other distinct quantities, $n(s)$ and S_{max}.

In Fig. 4.9 we briefly illustrate the effect of the increase of the aspect ratio on the percolation transition. For $\Psi = 15°$, larger values of l are associated with larger values of S_{max} at $\eta = 0.4$. Specifically, the system for $l = 3$ at $\eta = 0.4$ is clearly percolated, whereas for $l = 5$ it is in the transition region, and for $l = 7$ the system is not percolated. This shows that the percolation transition is suppressed for larger values of aspect ratio. Such a result agrees with our previous study [130]. For $\Psi > 15°$, the behavior is the opposite, i.e., the percolation transition is enhanced for larger values of l. This suggests that when the head-to-tail arrangements are dominant, the attraction between the rods is weaker, as already discussed, and the geometrical effects resultant from the increase of the rods aspect ratio (in a $2D$ system) make it harder to form large clusters [130]. This changes when the ribbon-like arrangement comes into play, because this arrangement has a stronger attraction and the geometrical effects resultant from the larger η and larger l no longer hamper the formation of large clusters, since the side-by-side arrangements is expected to be more present in the higher packing fraction regime.

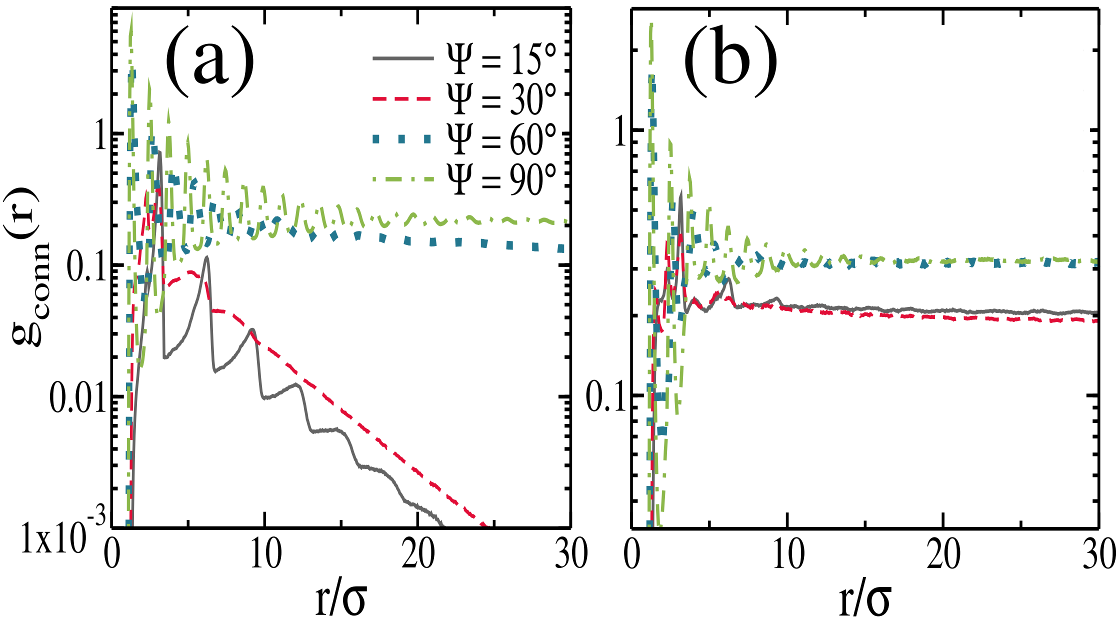

Figure 4.8: The pair connectedness function for different Ψ values and for packing fraction (a) $\eta = 0.2$ and (b) $\eta = 0.4$. The y-axes are in log scale.

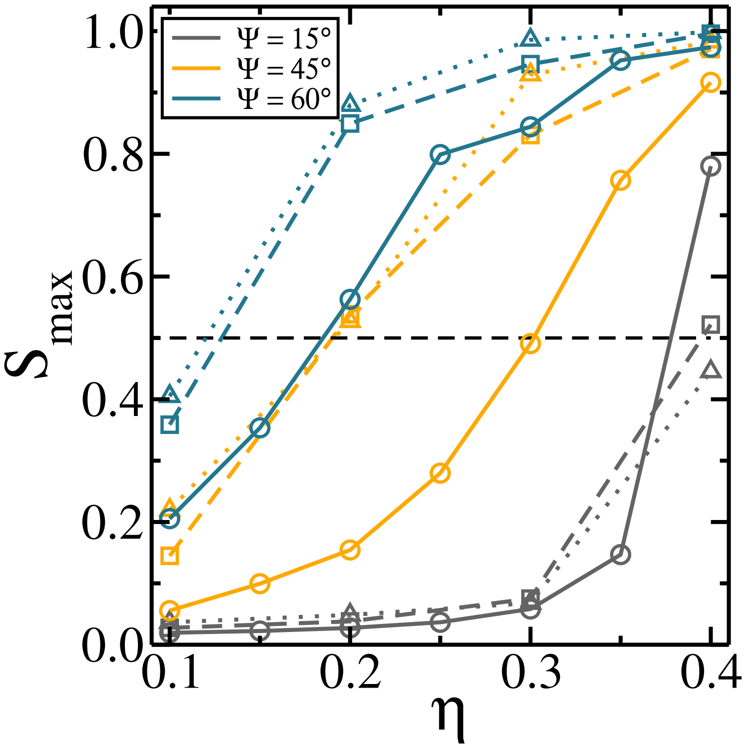

Figure 4.9: The average fraction of monomers in the largest cluster as a function of the packing fraction for different Ψ and different aspect ratios. Solid line with circle symbols: $l = 3$. Dashed line with square symbols: $l = 5$. Dotted lines with triangle symbols: $l = 7$.

4.3.3 Effect of temperature

In this section we study the effect of temperature on the connectivity properties. The increase of temperature has a similar effect as to decrease the effective interparticle interaction. Although, from the perspective of reducing finite-size effects, it is advantageous to consider the percolation transition as a function of the density rather than as a function of temperature. However, it is worth to study the effect of temperature on the connectivity properties and to examine the stability of the clusters. It is expected that the percolation transition is hampered when temperature of an interacting system increases [112, 106], since stronger thermal fluctuations may break the transient bonds.

In general, the ribbon-like arrangement is more stable against thermal fluctuations when compared to the head-to-tail structure. A specific example of the effect of temperature on the self-assembled configurations and on the percolation transition is presented in Fig. 4.10(a), where the average size of the largest cluster (S_{max}) is shown for $\eta = 0.4$ and for three values of Ψ. As pointed out previously, the system is percolated ($S_{max} \geq 0.5$) for all the three considered values of Ψ for sufficiently small temperature ($k_BT/\epsilon = 0.1$). In general, S_{max} decreases with increasing k_BT/ϵ, but how fast this happens depends on Ψ. The lower the value of Ψ, the lower the value of S_{max} for a given temperature. As a consequence, we may conclude that the percolated configurations of rods with larger Ψ are more stable against thermal fluctuations as compared to those with lower Ψ, and this is due to the formation of ribbon-like arrangements (see Fig. 4.10). When compared to the head-to-tail bond between two rods, the ribbon-like one is stronger, since all

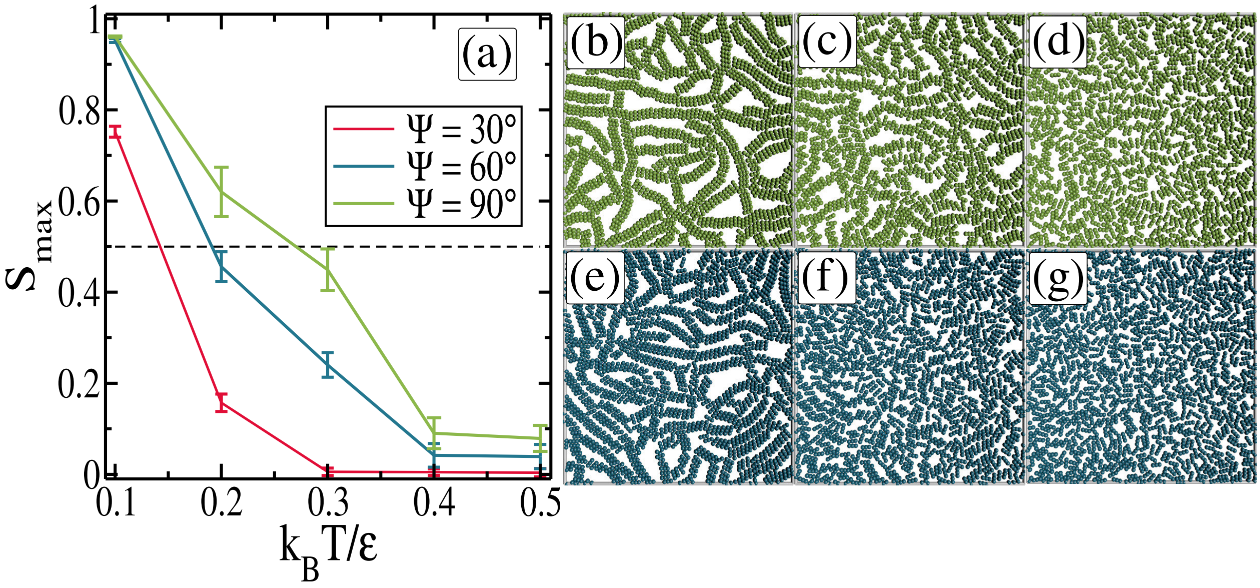

Figure 4.10: (a) The average fraction of monomers in the largest cluster as a function of temperature for $\eta = 0.4$. Some representative equilibrium configurations for $\eta = 0.4$ and: (b) $\Psi = 90°$, $k_BT/\epsilon = 0.1$; (c) $\Psi = 90°$, $k_BT/\epsilon = 0.3$; (d) $\Psi = 90°$, $k_BT/\epsilon = 0.5$; (e) $\Psi = 60°$, $k_BT/\epsilon = 0.1$; (f) $\Psi = 60°$, $k_BT/\epsilon = 0.3$; (g) $\Psi = 60°$, $k_BT/\epsilon = 0.5$.

dipoles of one rod are more strongly attracted to the dipoles of the other rod for $\Psi > 45°$, forming local head-to-tail bonds. We present in Figs. 4.10(b)-(g) snapshots of the ribbon-like structures, with ($\Psi = 90°$ and $\Psi = 60°$). For temperatures $k_BT/\epsilon = 0.1, 0.3$, and 0.5, highlighting how the clusters melt when submitted to higher temperatures. From these results, we may conclude that the percolation transition is enhanced for a system of peapod-like rods with larger values of Ψ even when it is analyzed as a function of temperature.

4.4 Conclusion

In summary, we investigated a two-dimensional system consisting of magnetic rods using Langevin Dynamics simulations. Each rod is composed of 3 soft beads having a central point-like dipole which interact via a DSS potential. This model is motivated by recent experimental [37] and theoretical [36, 130] studies. A novelty of our system is the misalignment of the dipole moment of the individual beads with respect to the axial axis, opening the possibility of forming complex structures using nonspherical particles [40, 39, 38, 34]. Structural properties were investigated with particular attention to the dependence on the dipole's direction Ψ and the packing fraction. We considered Ψ ranging from $\Psi = 15°$ to $\Psi = 90°$.

Due to the dipole-dipole head-to-tail assembly tendency, the increase of Ψ produces a range of different configurations. As a consequence, we found that for $\Psi \geq 45°$ we observe ribbon-like structures which are energetically the most favorable. Given the preference of ribbon-like chain configurations we paid special attention to the appearance of a cluster extending over the whole system for a sufficient large packing fraction, i.e., the percolation configuration. We observed that the larger Ψ, the stronger the attraction between rods, facilitating the clustering process and favoring the formation of the infinite cluster. As a consequence, the larger Ψ, the smaller the packing fraction for the occurrence of the percolation transition. We found that by increasing the aspect ratio of the rods the packing fraction increases, and different geometrical effects are observed depending on the dominant kind of rod arrangement. For head-to-tail arrangements, the percolation transition is hampered with increasing l. The opposite behavior was observed when the ribbon-like arrangement becomes dominant.

We also investigated the temperature dependence of the percolated configuration by analysing how the average size of the cluster depends on k_BT/ϵ. We observed that percolated configurations with large Ψ are thermodynamically more stable as a consequence of the formation of ribbon-like bonds, which is characterized by local head-to-tail arrangements.

5

Concluding Remarks

In this thesis we studied the self-assembly of magnetic rods in two dimensions by using numerical simulation techniques, specifically Molecular dynamics and Langevin dynamics simulation. In Chapter 1 an overview of soft condensed matter systems was given that are relevant for the present thesis. In Chapter 2 we presented the numerical methods used to study the systems investigated in the subsequent chapters. The results of the thesis were presented in Chapters 3 and 4.

In Chapter 3, the self-assembly of a two-dimensional system consisting of magnetic rods was investigated using Molecular Dynamics simulations. We analyzed the structural properties with particular attention to the dependence on the aspect ratio of the rods and the packing fraction of the system. We identified that the head-to-tail bond was the most energetically favorable for any aspect ratio leading to the chain formation. Other kinds of bonds, in which the rods are placed side by side with, e.g. parallel and antiparallel alignment, were observed with increasing packing fraction. Given such different kinds of arrangements we investigated the appearance of a percolated cluster for sufficient large packing fraction. We observed that the side-by-side arrangement and the two-dimensional confinement suppressed the percolation transition to higher aspect ratio. Such a behavior is opposite to what was previously observed for the $3D$ case. The transition to the isotropic-nematic phase was also investigated. We found that such a transition was facilitated by the increase of the aspect ratio of the rods, as expected. However, we also observed that the presence of magnetic bulk domains at large η-values, characterized by local ferromagnetic order, was responsible for the non-monotonic behavior of the nematic order with respect to the packing fraction. As a perspective, one may study the effect of the dimensionality of the system on the percolation transition, since the system exhibits different behavior for $2D$ and $3D$, by considering a quasi-$3D$ system.

In Chapter 4, the structural properties of magnetic rods with a misaligned dipole moment were investigated. We gave particular attention to the dependence on the misalignment on the self-assembled structures. We observed that the misalignment of the dipole moment (Ψ) of the individual beads with respect to the axial axis, opened the possibility of forming complex structures as a consequence of dipole-dipole head-to-tail assembly tendency. We observed that for $\Psi \geq 45°$ we found ribbon-like structures which are energetically the most favorable. We studied the appearance of a percolated cluster as a function of Ψ with increasing packing fraction. The larger Ψ, the stronger the attraction between rods, facilitating the clustering process and favoring the formation of an infinite cluster. As a consequence, the percolation transition occurred at smaller packing fractions for larger Ψ. Different geometrical effects are observed depending on the dominant kind of rod arrangement upon increasing of the aspect ratio. For head-to-tail arrangements, the percolation transition is hampered when increasing l. The opposite behavior was observed when the ribbon-like arrangement becomes dominant. We also investigated the temperature dependence of the percolated configuration by analysing how the average size of the cluster depends on k_BT/ϵ. We observed that percolated configurations with large Ψ are thermodynamically more stable as a consequence of the formation of ribbon-like bonds, which is characterized by local head-to-tail arrangements. An interesting perspective is to study the dynamical properties of the different aggregation state as affected by the different misalignment of the dipole moment.

Appendix A

Derivation of the torque on a magnetic rod composed by dipolar beads

To prove Eq. (3.6), we must go back to the definition of the torque on a current distribution $\boldsymbol{J}(\boldsymbol{r})$. The infinitesimal torque on dV with a current distribution $\boldsymbol{J}(\boldsymbol{r})$ by a non-uniform magnetic field is

$$d\boldsymbol{N}_{o'} = (\boldsymbol{r}_i - \boldsymbol{r}_{o'}) \times \boldsymbol{J} \times \boldsymbol{B} dV, \tag{A1}$$

where $\boldsymbol{r}_i$ is the coordinate which localizes dV (where $\boldsymbol{B}$ acts). The torque is calculated with respect to $\boldsymbol{r}_{o'}$, so $\boldsymbol{r}_i - \boldsymbol{r}_{o'}$ is the displacement vector.

The point is how to evaluate the contribution of the torque by each dipole moment when $\boldsymbol{r}_{o'}$ and the "center"[1] of the dipole (bead) are not the same. However, the torque of a magnetic dipole measured with respect to its center, (center of the current distribution), namely $\boldsymbol{r}_o$, it is already known. By adding and subtracting $\boldsymbol{r}_o$ in Eq. (A1)

$$d\boldsymbol{N}_{o'} = (\boldsymbol{r}_i + \boldsymbol{r}_o - \boldsymbol{r}_o - \boldsymbol{r}_{o'}) \times \boldsymbol{J} \times \boldsymbol{B} dV. \tag{A2}$$

After integration of Eq. (A3) over the volume, we have

$$\boldsymbol{N}_{o'} = \int_V (\boldsymbol{r}_i - \boldsymbol{r}_o) \times \boldsymbol{J} \times \boldsymbol{B} dV + \int_V (\boldsymbol{r}_o - \boldsymbol{r}_{o'}) \times \boldsymbol{J} \times \boldsymbol{B} dV. \tag{A3}$$

As the magnetic field is non-uniform, we may perform a Taylor's expansion in $\boldsymbol{B}(\boldsymbol{r})$ around a vector which localizes the coordinate of dipole moment $\boldsymbol{r}_d$, as long as $\boldsymbol{B}(\boldsymbol{r})$ does not vary significantly over position

$$\boldsymbol{B}(\boldsymbol{r}) = \boldsymbol{B}(\boldsymbol{r}_d) + [(\boldsymbol{r} - \boldsymbol{r}_d) \cdot \boldsymbol{\nabla}_d]\boldsymbol{B}(\boldsymbol{r}_d) + ... \tag{A4}$$

---

[1] The quotation marks are because the magnetic dipole actually has no center, since magnetism is not due to magnetic monopoles which we can separate them each other. The representation of the magnetic dipole is only a mathematical tool to depict the Ampère model (current loop at the center of the dipole).

In order to compute the net torque with respect to "o", the vector $(\boldsymbol{r}_i - \boldsymbol{r}_o)$ must span over the whole volume V. On the other side, $(\boldsymbol{r}_o - \boldsymbol{r}_{o'})$ is a fixed vector.

When we evaluate the torque in a current loop by an external magnetic field B, we usually assume that its center is the origin of the coordinate system, which also corresponds to the center of its related magnetic dipole. Such an expression is well-known as: $\boldsymbol{N} = \boldsymbol{\mu} \times \boldsymbol{B}$. Therefore, let "o" be in the center of current distribution, so $\boldsymbol{B}$ and $\boldsymbol{J}$ must be regarded with respect to the same origin "o"

$$\boldsymbol{J}(\boldsymbol{r}) \rightarrow \boldsymbol{J}(\boldsymbol{r}_i - \boldsymbol{r}_o) \qquad \boldsymbol{B}(\boldsymbol{r}) \rightarrow \boldsymbol{B}(\boldsymbol{r}_i - \boldsymbol{r}_o). \tag{A5}$$

For the sake of simplification, let us call $(\boldsymbol{r}_i - \boldsymbol{r}_o)$ just $\boldsymbol{r}$, thus

$$\boldsymbol{N}_{o'} = \int_V \boldsymbol{r} \times \boldsymbol{J}(\boldsymbol{r}) \times \boldsymbol{B}(\boldsymbol{r}) dV + (\boldsymbol{r}_o - \boldsymbol{r}_{o'}) \times \int_V \boldsymbol{J}(\boldsymbol{r}) \times \boldsymbol{B}(\boldsymbol{r}) dV. \tag{A6}$$

However, we know that the net force $(\boldsymbol{F})$ on a current distribution is

$$\boldsymbol{F} = \int_V \boldsymbol{J}(\boldsymbol{r}) \times \boldsymbol{B}(\boldsymbol{r}) dV, \tag{A7}$$

using Eq. (A4) and Eq. (A7)

$$\boldsymbol{F} = \int_V \boldsymbol{J}(\boldsymbol{r}) \times \left\{ \boldsymbol{B}(\boldsymbol{r}_d) + [(\boldsymbol{r} - \boldsymbol{r}_d) \cdot \boldsymbol{\nabla}_d] \boldsymbol{B}(\boldsymbol{r}_d) + ... \right\} dV. \tag{A8}$$

As the integral acts on $\boldsymbol{r}$, we have

$$\boldsymbol{F} = \left(\int_V \boldsymbol{J}(\boldsymbol{r}) dV \right) \times \boldsymbol{B}(\boldsymbol{r}_d) + \int_V \boldsymbol{J}(\boldsymbol{r}) \times [(\boldsymbol{r} \cdot \boldsymbol{\nabla}_d) \boldsymbol{B}(\boldsymbol{r}_d)] dV - \left(\int_V \boldsymbol{J}(\boldsymbol{r}) dV \right) \times [(\boldsymbol{r}_d \cdot \boldsymbol{\nabla}_d) \boldsymbol{B}(\boldsymbol{r}_d)] + ... \tag{A9}$$

Making use of the following identity [145]

$$\int_V (F \boldsymbol{J} \cdot \boldsymbol{\nabla} G + G \boldsymbol{J} \cdot \boldsymbol{\nabla} F) dV = 0, \tag{A10}$$

as long as $\boldsymbol{F}(\boldsymbol{r})$ and $\boldsymbol{G}(\boldsymbol{r})$ are well-behaved, $\boldsymbol{\nabla} \cdot \boldsymbol{J} = 0$ and $J \neq \infty$ for any r. Let us define, $\boldsymbol{F}(\boldsymbol{r}) = 1$ and $\boldsymbol{G}(\boldsymbol{r}) = x_i$

$$\int_v [1 \cdot \boldsymbol{J} \cdot \underbrace{\nabla x_i}_{\hat{e}_i} + x_i \cdot \boldsymbol{J} \cdot \underbrace{\nabla 1}_{0}] dV = 0, \tag{A11}$$

$$\int_v \boldsymbol{J} \cdot \hat{e}_i dV = 0, \tag{A12}$$

$$\int_v \boldsymbol{J}_i dV = 0. \tag{A13}$$

Therefore, the volume integral of any $\boldsymbol{J}$ component is zero, thus

$$\int_V \boldsymbol{J} dV = 0. \tag{A14}$$

This term is the magnetic equivalent to the interaction caused by the electric charge to the electric field (Gauss's Law). As there are no magnetic monopoles, it should indeed be null. Thus, from Eq. (A9)

$$\boldsymbol{F} = \int_V \boldsymbol{J}(\boldsymbol{r}) \times [(\boldsymbol{r} \cdot \boldsymbol{\nabla}_d)\boldsymbol{B}(\boldsymbol{r}_d)]dV + ... \tag{A15}$$

Using the following identity:

$$\boldsymbol{\nabla}(\boldsymbol{A} \cdot \boldsymbol{B}) = (\boldsymbol{A} \cdot \boldsymbol{\nabla})\boldsymbol{B} + \boldsymbol{A} \times (\boldsymbol{\nabla} \times \boldsymbol{B}) + (\boldsymbol{B} \cdot \boldsymbol{\nabla})\boldsymbol{A} + \boldsymbol{B} \times (\boldsymbol{\nabla} \times \boldsymbol{A}), \tag{A16}$$

for $\boldsymbol{A} = \boldsymbol{r}$, $\boldsymbol{B} = \boldsymbol{B}(\boldsymbol{r}_d)$ and $\boldsymbol{\nabla} = \boldsymbol{\nabla}_d$, we have

$$\boldsymbol{\nabla}_d(\boldsymbol{r} \cdot \boldsymbol{B}(\boldsymbol{r}_d)) = (\boldsymbol{r} \cdot \boldsymbol{\nabla}_d)\boldsymbol{B}(\boldsymbol{r}_d) + \boldsymbol{r} \times (\boldsymbol{\nabla}_d \times \boldsymbol{B}(\boldsymbol{r}_d)) + (\boldsymbol{B}(\boldsymbol{r}_d) \cdot \boldsymbol{\nabla}_d)\boldsymbol{r} + \boldsymbol{B}(\boldsymbol{r}_d) \times (\boldsymbol{\nabla}_d \times \boldsymbol{r}). \tag{A17}$$

As $\boldsymbol{\nabla}_d$ acts in $\boldsymbol{r}_d$ and $\boldsymbol{\nabla}_d \times \boldsymbol{B}(\boldsymbol{r}_d) = 0$ ($\boldsymbol{J}(\boldsymbol{r})$ is not the source of $\boldsymbol{B}(\boldsymbol{r}_d)$)

$$\boldsymbol{\nabla}_d(\boldsymbol{r} \cdot \boldsymbol{B}(\boldsymbol{r}_d)) = (\boldsymbol{r} \cdot \boldsymbol{\nabla}_d)\boldsymbol{B}(\boldsymbol{r}_d), \tag{A18}$$

thus

$$\boldsymbol{F} = \int_V \boldsymbol{J}(\boldsymbol{r}) \times \boldsymbol{\nabla}_d[\boldsymbol{r} \cdot \boldsymbol{B}(\boldsymbol{r}_d)]dV..., \tag{A19}$$

however

$$\boldsymbol{\nabla}_d \times \{[\boldsymbol{r} \cdot \boldsymbol{B}(\boldsymbol{r}_d)]\boldsymbol{J}(\boldsymbol{r})\} = \boldsymbol{\nabla}_d[\boldsymbol{r} \cdot \boldsymbol{B}(\boldsymbol{r}_d)] \times \boldsymbol{J}(\boldsymbol{r}) + [\boldsymbol{r} \cdot \boldsymbol{B}(\boldsymbol{r}_d)] \underbrace{[\boldsymbol{\nabla}_d \times \boldsymbol{J}(\boldsymbol{r})]}_{0}, \tag{A20}$$

thus

$$\boldsymbol{J}(\boldsymbol{r}) \times \boldsymbol{\nabla}_d[\boldsymbol{r} \cdot \boldsymbol{B}(\boldsymbol{r}_d)] = -\boldsymbol{\nabla}_d \times \{[\boldsymbol{r} \cdot \boldsymbol{B}(\boldsymbol{r}_d)]\boldsymbol{J}(\boldsymbol{r})\}\,. \tag{A21}$$

Using Eq. (A19) and Eq. (A21), we have

$$\boldsymbol{F} = -\int_V \boldsymbol{\nabla}_d \times \{[\boldsymbol{r} \cdot \boldsymbol{B}(\boldsymbol{r}_d)]\boldsymbol{J}(\boldsymbol{r})\}\, dV..., \tag{A22}$$

$$\boldsymbol{F} = -\boldsymbol{\nabla}_d \times \left(\boldsymbol{B}(\boldsymbol{r}_d) \cdot \int_V \boldsymbol{r}\boldsymbol{J}(\boldsymbol{r})dV\right)... \tag{A23}$$

From the Ref. [145], we have

$$\boldsymbol{B} \cdot \int_V \boldsymbol{r} J_i dV = -\frac{1}{2}\sum_{j,k} \epsilon_{ijk} B_j \int_V (\boldsymbol{r} \times \boldsymbol{J})_k dV, \tag{A24}$$

remembering that

$$(\boldsymbol{a} \times \boldsymbol{b})_k = \sum_{ij} \epsilon_{ijk} a_i b_j, \qquad \epsilon_{ijk} = \epsilon_{jki}, \tag{A25}$$

thus

$$\boldsymbol{B} \cdot \int_V \boldsymbol{r} J_i dV = -\frac{1}{2}\left[\boldsymbol{B} \times \int_V (\boldsymbol{r} \times \boldsymbol{J})dV\right]_i. \tag{5.1}$$

Finally

$$\boldsymbol{B}\cdot\int_V \boldsymbol{r}\boldsymbol{J}(\boldsymbol{r})dV=-\frac{1}{2}\left[\boldsymbol{B}\times\int_V(\boldsymbol{r}\times\boldsymbol{J})dV\right]. \tag{A26}$$

By the definition of magnetic dipole related to a current distribution

$$\boldsymbol{\mu}=\frac{1}{2}\int_V \boldsymbol{r}\times\boldsymbol{J}dV, \tag{A27}$$

thus

$$\boldsymbol{B}\cdot\int_V \boldsymbol{r}\boldsymbol{J}(\boldsymbol{r})dV=\boldsymbol{\mu}\times\boldsymbol{B}(\boldsymbol{r}). \tag{A28}$$

Using Eq. (A28) on Eq. (A22)

$$\boldsymbol{F}=-\boldsymbol{\nabla_d}\times\{\boldsymbol{\mu}\times\boldsymbol{B}(\boldsymbol{r}_d)\}+... \tag{A29}$$

Taking the relevant terms of Eq. (A31) and using the following identity

$$\boldsymbol{\nabla}_d\times(\boldsymbol{B}(\boldsymbol{r}_d)\times\boldsymbol{\mu})=(\boldsymbol{\nabla}_d\cdot\boldsymbol{\mu})\boldsymbol{B}(\boldsymbol{r}_d)-(\boldsymbol{\nabla}_d\cdot\boldsymbol{B}(\boldsymbol{r}_d))\boldsymbol{\mu}_d+(\boldsymbol{\mu}\cdot\boldsymbol{\nabla}_d)\boldsymbol{B}(\boldsymbol{r}_d)-(\boldsymbol{B}(\boldsymbol{r}_d)\cdot\boldsymbol{\nabla}_d)\boldsymbol{\mu}, \tag{A30}$$

therefore

$$\boldsymbol{F}=-\boldsymbol{\nabla_d}\times\{(\boldsymbol{\nabla}_d\cdot\boldsymbol{\mu})\boldsymbol{B}(\boldsymbol{r}_d)-(\boldsymbol{\nabla}_d\cdot\boldsymbol{B}(\boldsymbol{r}_d))\boldsymbol{\mu}_d+(\boldsymbol{\mu}\cdot\boldsymbol{\nabla}_d)\boldsymbol{B}(\boldsymbol{r}_d)-(\boldsymbol{B}(\boldsymbol{r}_d)\cdot\boldsymbol{\nabla}_d)\boldsymbol{\mu}\}. \tag{A31}$$

As $\boldsymbol{\mu}$ does not depend on $\boldsymbol{r}_d$ and $\boldsymbol{\nabla}_d\cdot\boldsymbol{B}(\boldsymbol{r}_d)=0$, we have

$$\boldsymbol{\nabla}_d\times(\boldsymbol{B}(\boldsymbol{r}_d)\times\boldsymbol{\mu})=(\boldsymbol{\mu}\cdot\boldsymbol{\nabla}_d)\boldsymbol{B}(\boldsymbol{r}_d), \tag{A32}$$

but

$$\boldsymbol{\nabla}_d\left[\boldsymbol{\mu}\cdot\boldsymbol{B}(\boldsymbol{r}_d)\right]=(\boldsymbol{\mu}\cdot\boldsymbol{\nabla}_d)\boldsymbol{B}(\boldsymbol{r}_d)+\boldsymbol{\mu}\times\underbrace{[\boldsymbol{\nabla}_d\times\boldsymbol{B}(\boldsymbol{r}_d)]}_{0}+\underbrace{(\boldsymbol{B}(\boldsymbol{r}_d)\cdot\boldsymbol{\nabla}_d)\boldsymbol{\mu}}_{0}+\boldsymbol{B}(\boldsymbol{r}_d)\times\underbrace{(\boldsymbol{\nabla}_d\times\boldsymbol{\mu})}_{0}, \tag{A33}$$

Consequently

$$\boldsymbol{\nabla}_d\left[\boldsymbol{\mu}\cdot\boldsymbol{B}(\boldsymbol{r}_d)\right]=(\boldsymbol{\mu}\cdot\boldsymbol{\nabla}_d)\boldsymbol{B}(\boldsymbol{r}_d), \tag{A34}$$

As $U^D=-\boldsymbol{\mu}\cdot\boldsymbol{B}$ is the interaction between $\boldsymbol{\mu}$ and the net magnetic field $\boldsymbol{B}$

$$\boldsymbol{\nabla}(\boldsymbol{\mu}\cdot\boldsymbol{B})=-\boldsymbol{\nabla}U^D, \tag{A35}$$

finally

$$\boldsymbol{F}=-\boldsymbol{\nabla}_d U^D. \tag{A36}$$

Therefore, for now, the Eq. (A3) will be

$$\boldsymbol{N}_{o'}=\int_V \boldsymbol{r}\times\boldsymbol{J}(\boldsymbol{r})\times\boldsymbol{B}(\boldsymbol{r})dV+(\boldsymbol{r}_o-\boldsymbol{r}_{o'})\times\left\{-\boldsymbol{\nabla}U^D\right\}. \tag{A37}$$

We must solve the first integral of Eq. (A37), in this regard, we use the following identity

$$\boldsymbol{A}\times(\boldsymbol{B}\times\boldsymbol{C})=\boldsymbol{B}(\boldsymbol{A}\cdot\boldsymbol{C})-\boldsymbol{C}(\boldsymbol{A}\cdot\boldsymbol{B}), \tag{A38}$$

Thus

$$\int_V \boldsymbol{r} \times \left[\boldsymbol{J}(\boldsymbol{r}) \times \boldsymbol{B}(\boldsymbol{r})\right] dV = \int_V \left[\boldsymbol{r} \cdot \boldsymbol{B}(\boldsymbol{r})\right] \boldsymbol{J}(\boldsymbol{r}) dV - \int_V \left[\boldsymbol{r} \cdot \boldsymbol{J}(\boldsymbol{r})\right] \boldsymbol{B}(\boldsymbol{r}) dV. \tag{A39}$$

We are interested in magnetic field at dipole moment's position, so, let us do the approximation: $\boldsymbol{B}(\boldsymbol{r}) \approx \boldsymbol{B}(\boldsymbol{r}_d)$,

$$\int_V \boldsymbol{r} \times \left[\boldsymbol{J}(\boldsymbol{r}) \times \boldsymbol{B}(\boldsymbol{r}_d)\right] dV = \int_V \left[\boldsymbol{r} \cdot \boldsymbol{B}(\boldsymbol{r}_d)\right] \boldsymbol{J}(\boldsymbol{r}) dV - \int_V \left[\boldsymbol{r} \cdot \boldsymbol{J}(\boldsymbol{r})\right] \boldsymbol{B}(\boldsymbol{r}_d) dV. \tag{A40}$$

As the integral acts in $\boldsymbol{r}$, we find

$$\int_V \boldsymbol{r} \times \left[\boldsymbol{J}(\boldsymbol{r}) \times \boldsymbol{B}(\boldsymbol{r}_d)\right] dV = \boldsymbol{B}(\boldsymbol{r})_d \cdot \int_V \boldsymbol{r}\boldsymbol{J}(\boldsymbol{r}) dV - \boldsymbol{B}(\boldsymbol{r}_d) \int_V \left[\boldsymbol{r} \cdot \boldsymbol{J}(\boldsymbol{r})\right] dV. \tag{A41}$$

The first integral of Eq. (A41) is known from Eq. (A28). In the second integral, we will use Eq. (A10) for $F = G = x_i$

$$\begin{aligned} \int_V \left(x_i \boldsymbol{J} \cdot \boldsymbol{\nabla} x_i + x_i \boldsymbol{J} \cdot \boldsymbol{\nabla} x_i\right) dV &= 0, \\ \int_V \left(x_i \boldsymbol{J} \cdot \hat{e}_i x_i + x_i \boldsymbol{J} \cdot \hat{e}_i x_i\right) dV &= 0, \\ \int_V \left(x_i J_i x_i + x_i J_i x_i\right) dV &= 0, \\ \int_V \boldsymbol{r} \cdot \boldsymbol{J} dV = 0 \qquad \mathit{for} \qquad \boldsymbol{r} = \sum x_i \hat{e}_i, \qquad \boldsymbol{J} &= \sum J_i \hat{e}_i. \end{aligned}$$

Therefore, the Eq. (A41) will be

$$\int_V \boldsymbol{r} \times \left[\boldsymbol{J}(\boldsymbol{r}) \times \boldsymbol{B}(\boldsymbol{r}_d)\right] dV = \boldsymbol{m} \times \boldsymbol{B}(\boldsymbol{r}_d). \tag{A42}$$

Finally, the Eq. (A37) will be

$$\boldsymbol{N}_{o'} = \boldsymbol{\mu} \times \boldsymbol{B}(\boldsymbol{r}_d) + (\boldsymbol{r}_o - \boldsymbol{r}_{o'}) \times \left\{-\boldsymbol{\nabla} U^D\right\}. \tag{A43}$$

Where, $\boldsymbol{B}(\boldsymbol{r}_d)$ is the magnetic field generated by another source [$\boldsymbol{B}_{ij}$ from Eq. (3.6)], e.g. by other dipole moments, at μ's position. The vector $\boldsymbol{r}_o - \boldsymbol{r}_{o'}$ is the displacement vector between the center of μ and the point which the torque is computed, e.g. the center of rod [$\boldsymbol{d}_m$ from Eq. (3.6)].

In the Eq. (3.6), we also have the force which comes from LJ interaction $U^{rep} = \sum u^{rep}$. As we consider the center of dipole equals to the center of soft bead, the displacement vector $\boldsymbol{d}_m$ is the same. The net magnetic field ($\boldsymbol{B}(\boldsymbol{r}_d)$) is the sum of all $\boldsymbol{B}_{jm}$ generated by all dipole moments

$$\begin{aligned} \boldsymbol{N}_{o'} &= \boldsymbol{\mu} \times \boldsymbol{B}(\boldsymbol{r}_d) + (\boldsymbol{r}_o - \boldsymbol{r}_{o'}) \times \left\{-\boldsymbol{\nabla} U^D + U^{rep}\right\}, \\ \boldsymbol{N}_{o'} &= \boldsymbol{\mu} \times \boldsymbol{B}(\boldsymbol{r}_d) + \boldsymbol{d}_m \times \boldsymbol{F}. \end{aligned} \tag{A44}$$

where, $\boldsymbol{F}$ is the net force on $\boldsymbol{\mu}$. By these means, the derivation of Eq. (3.6) is completed.

Appendix B
Publications related to this thesis

1) **Jorge L. C. Domingos**, F. M. Peeters and W. P. Ferreira, *Self-assembly of rigid magnetic rods consisting of single dipolar beads in two dimensions*, Phys. Rev. E **96**, 012603 (2017).

2) **Jorge L. C. Domingos**, F. M. Peeters and W. P. Ferreira, *Self-assembly and clustering of magnetic peapod-like rods with tunable directional interaction*, PloS One **13**(4), e0195552 (2018).

Bibliography

[1] P. M. Chaikin and T.C. Lubensky, *Principles of Condensed Matter Physics* Cambridge University Press, (2000).

[2] G. Gompper, J.K.G. Dhont, D. Richter, *European Physical Journal E* **26**, 1 (2008).

[3] A. Einstein, *Annalen der Physik* **322**, 8 (1905).

[4] M. Doi, *Soft matter physics* Oxford University Press, (2013).

[5] R. A. L. Jones, *Soft Condensed Matter* Oxford University Press, (2002).

[6] W. B. Russel, A. D. Saville and R. W. Schowalter, *Colloidal dispersions* Cambridge University Press, (1989).

[7] J. J. Edward, *Proceedings of the Royal Society of London A: Mathematical, Physical and Engineering Sciences* Cambridge University Press, **106**, 738 (1924).

[8] D. C. Rapaport, *The Art of Molecular Dynamics Simulation*, Cambridge University press (2004).

[9] M. E. van Leeuwen and B. Smit, *Physical Review Letters* **71**, 3991 (1993).

[10] B. Groh and S. Dietrich, *Physical Review E* **50**, 3814 (1994).

[11] R. P. Sear, *Physical Review Letters* **76**, 13 (1996).

[12] W. H. Stockmayer, *The Journal of Chemical Physics* **9**, 5 (1941).

[13] M. J. Stevens and G.S. Grest, *Physical Review E* **51**, 6 (1995).

[14] P. I. C. Teixeira, J.M. Tavares and M.M.T. da Gama, *Journal of Physics: Condensed Matter* **12**, 33 (2000).

[15] T. Albrecht, C. Bührer, M. Fähnle, K. Maier, D. Platzek and J. Reske, *Applied Physics A* **65**, 215 (1997).

[16] A. K. Gupta and M. Gupta, *Biomaterials* **26**, 3995 (2005).

[17] E. Duguet, S. Mornet, S. Vasseur, F. Grasset, P. Veverka, G. Goglio, A. Demourgues, J. Portier and E. Pollert, *Progress in Solid State Chemistry* **34**, 237 (2006).

[18] T. Hyeon, *Chemical Communications* 927 (2003).

[19] S. Gubin, *Magnetic Nanoparticles*, Wiley (2009).

[20] N. A. Frey, Peng, Sheng, Cheng, Kai, Sun and Shouheng, *Chem. Soc. Rev.* **38**, 2532 (2008).

[21] M. Klokkenburg, B. H. Erné, J. D. Meeldijk, A. Wiedenmann, A. V. Petukhov, R. P. A. Dullens and A.P. Philipse, *Physical review letters* **97**, 18 (2006).

[22] P. Bender, A. Tschöpe and R. Birringer, *Journal of Magnetism and Magnetic Materials* **346**, 152 (2013).

[23] R. Colin, L. Chevry, J. F. Berret and B. Abou, *Soft Matter* **10**, 1167 (2014).

[24] T. Petit, L. Zhang, K. E. Peyer, B. E. Kratochvil and B. J. Nelson, *Nano Letters* **12** 156 (2011).

[25] T. Sawetzki, S. Rahmouni, C. Bechinger and D. W. Marr, *Proceedings of the National Academy of Sciences* **105**, 20141 (2008).

[26] B. Kavčič, D. Babič, N. Osterman, B. Podobnik and I. Poberaj, *Applied Physics Letters* **95**, 023504 (2009).

[27] C. E. Sing, L. Schmid, M. F. Schneider, T. Franke and A. Alexander-Katz, *Proceedings of the National Academy of Sciences* **107**, 535 (2010).

[28] L. Zhang, T. Petit, Y. Lu, B. E. Kratochvil, K. E. Peyer, R. Pei, J. Lou and B. J. Nelson, *ACS Nano* **4**, 6228 (2010).

[29] T. R. Kline, W. F. Paxton, T. E. Mallouk and A. Sen, *Angewandte Chemie* **117**, 754 (2005).

[30] B. J. Lemaire, P. Davidson, J. Ferré, J. P. Jamet, P. Panine, I. Dozov, J. P. Jolivet, *Physical Review Letters* **88**, 125507 (2002).

[31] J. Philip, P. Shima and B. Raj, *Applied Physics Letters* **91**, 203108 (2007).

[32] Y. Piao, J. Kim, H. B. Na, D. Kim, J. S. Baek, M. K. Ko, J. H. Lee, M. Shokouhimehr and T. Hyeon, *Nature Materials* **7**, 242 (2008).

[33] J. Yan , K. Chaudharyn, S. C. Bae, J. A. Lewis and S. Granick, *Nature communications* **4**, 1516 (2013).

[34] F. Martinez-Pedrero, A. Cebers and P. Tierno*Phys. Rev. Applied* **6**, 034002 (2016).

[35] O. Bomati-Miguel, A. F. Rebolledo and P. Tartaj, *Chemical Communications*, 35 (2008).

[36] C. E. Alvarez and S. H. Klapp, *Soft Matter* **8**, 7480 (2012).

[37] R. Birringer, H. Wolf, C. Lang, A. Tschöpe and A. Michels, *Zeitschrift für Physikalische Chemie* **222**, 229 (2008).

[38] F. Martinez-Pedrero, A. Cebers and P. Tierno, *Soft matter* **12**, 3688 (2016).

[39] S. H. Lee and C. M. Liddell, *Small* **5**, 17 (2009).

[40] H. Singh, P. E. Laibinis and T. A. Hatton, *Langmuir* **21**, 11500 (2005).

[41] M. P. Allen and D. J. Tildesley, *Computer Simulation of Liquids*, Oxford university press (1989).

[42] P. P. Ewald, *Annalen der Physik* **64**, (64) (1921).

[43] D. Frenkel and B. Smit, *Understanding molecular simulations: from algorithms to applications*, Academic Press (2002).

[44] D. Beeman, *Journal of Computational Physics* **20**, 2 (1976).

[45] C. K. Birdsall and A. B. Langdon, *Plasma physics via computer simulation*, CRC press (2004).

[46] L. Verlet, *Physical Review* **159**, 1 (1967).

[47] D. J. Auerbach, W. Paul, A. F. Bakker, C. Lutz, W. E. Rudge and F. F. Abraham, *Journal of Physical Chemistry* **91**, 4881 (1987).

[48] N. Metropolis, A. W. Rosenbluth, M. N. Rosenbluth, A. H. Teller and E. Teller, *The Journal of Chemical Physics 21*, 6 (1953).

[49] F. Reif, *Fundamentals of statistical and thermal physics*, McGraw-Hill (1965).

[50] R. K. Pathria and Beale, *Statistical Mechanics*, Elsevier Science (2011).

[51] H. J. Berendsen, J. P. M. Postma, W. F. van Gunsteren, A. DiNola and J. Haak, *The Journal of Chemical Physics* **81**, 3684 (1984).

[52] H. C. Andersen, *The Journal of Chemical Physics* **72**, 2384 (1980).

[53] W. G. Hoover, *Physical Review* **31**, 1695 (1985).

[54] R. L. Davidchack, R. Handel and M.V. Tretyakov, *The Journal of Chemical Physics* **130**, 23 (2009).

[55] Z. Wang, C. Holm and H. W. Müller, *Physical Review E* **66**, 021405 (2002).

[56] Available at: `https://en.wikipedia.org/wiki/Radial_distribution_function.` Accessed in January, 2018.

[57] D. Lucena, *Diffusive properties of soft condensed matter systems under external confinement*, Universidade Federal do Ceará, PhD Thesis (2014).

[58] S. S. Das, A. P. Andrews and S. Greer, *The Journal of Chemical Physics* **102**, 2951 (1995).

[59] M. Rubinstein and R. H. Colby, *Polymer Physics*, OUP Oxford (2003).

[60] P. J. Flory, *Principles of polymer chemistry* Cornell University Press, Ithaca and London, (1953).

[61] J. Russo, P. Tartaglia and F. Sciortino, *Soft Matter"* **6**, 4229 (2010).

[62] D. Stauffer and A. Aharony, *Introduction to Percolation Theory*, Taylor Francis Group (1994).

[63] P. D. Godfrin, N. E. Valadez-Pérez, R. Castaneda-Priego, N. J. Wagner and Y. Liu, *Soft Matter* **10**, 5061 (2014).

[64] E. Zaccarelli, P. J. Lu, F. Ciulla, D. A. Weitz and F. Sciortino, *J. Phys.: Condens. Matter* **20**, 494242 (2008).

[65] Y. Duda, *The Journal of Chemical Physics* **130**, 116101 (2009).

[66] L. Rovigatti, J. Russo and F. Sciortino, *Soft Matter* **8**, 6310 (2012).

[67] F. Romano and F. Sciortino, *Nature Materials* **10**, 171 (2011).

[68] F. Sciortino and E. Zaccarelli, *Curr. Opin. Solid State Mater. Sci.* **15**, 246 (2011).

[69] Y. Liu and R. Pandey, *The Journal of Chemical Physics* **105**, 825 (1996).

[70] R. Chelakkot and T. Gruhn, *Soft Matter* **8**, 11746 (2012).

[71] E. Butkov, *Física matemática*, Livros Técnicos e Científicos (1988).

[72] S. Kim and S. J. Karrila, *Microhydrodynamics: Principles and Selected Applications* Dover (2005).

[73] J. K. G. Dhont and W. J. Briels, *Rod-Like Brownian Particles in Shear Flow* Wiley-VCH Verlag GmbH & Co. KGaA, 147 (2007).

[74] R. D. Groot, *T*he Journal of Chemical Physics **136**, 6 (2012).

[75] Tirado and J. G. de La Torre, *The Journal of Chemical Physics* **71**, 2581 (1979).

[76] Tirado and J. G. de La Torre, *The Journal of Chemical Physics* **73**, 1986 (1980).

[77] R. Mannella, *Int. J. Mod. Phys. C* **13**, 11770 (2002).

[78] R. Mannella, *Physical Review E mathbf*69 041107 (2004).

[79] G. Nägele, J. K. G. Dhont and G. Meier, *Diffusion in Condensed Matter - Chapter* **16**, 619 (2005).

[80] S. L. Biswal and A. P. Gast, *Physical Review E* **68**, 021402 (2003).

[81] C. Goubault, P. Jop, M. Fermigier, J. Baudry, E. Bertrand and J. Bibette, *Physical Review Letters* **91**, 260802 (2003).

[82] J. M. Dempster, P. Vazquez-Montejo, M. O. de la Cruz, *Physical Review E* **95**, 052606 (2017).

[83] K. J. Lee, J. Yoon and J. Lahann, *Current Opinion in Colloid & Interface Science* **16**, 195 (2011).

[84] P. Tierno, *Physical Chemistry Chemical Physics* **16**, 23515 (2014).

[85] J. L. Baker, A. Widmer-Cooper, M. F. Toney, P. L. Geissler and A. P. Alivisatos, *Nano letters* **10**, 195 (2009).

[86] K. H. Bhatt and O. D. Velev, *Langmuir* **20**, 467 (2004).

[87] N. Osterman, D. Babič, I. Poberaj, J. Dobnikar and P. Ziherl, *Physical Review Letters* **99**, 248301 (2007).

[88] J. J. Juàrez and M. A. Bevan, *The Journal of Chemical Physics* **131**, 134704 (2009).

[89] O. D. Velev and S. Gupta,*Advanced Materials* **21**, 1897 (2009).

[90] G. Zarragoicoechea, D. Levesque and J. Weis, *Molecular Physics* **75**, 989 (1992).

[91] S. C. McGrother, A. Gil-Villegas and G. Jackson, *Molecular Physics* **95**, 657 (1998).

[92] D. Levesque, J. J. Weis and G. J. Zarragoicoechea, *Physical Review E* **47**, 496 (1993).

[93] D. C. Williamson and F. del Rio, *The Journal of Chemical Physics* **107**, 22 (1997).

[94] J. Philip, P. Shima and B. Raj, *Applied Physics Letters* **92**, 043108 (2008).

[95] K. Leung and D. Chandler, *Journal of Statistical Physics* **63**, 837 (1991).

[96] T. Schilling, S. Jungblut and M. A. Miller, *Physical Review Letters* **98**, 108303 (2007).

[97] R. H. J. Otten and P. van der Schoot, *Physical Review Letters* **108**, 088301 (2012).

[98] R. F. Kayser and H. J. Raveché, *Physical Review A* **17**, 2067 (1978).

[99] We are aware that the Berendsen thermostat does not include the temperature fluctuations in the canonical ensemble [100]. We also performed Langevin dynamics and Microcanonical MD simulations and the results are consistent with those obtained with the Berendsen thermostat, which led us to conclude that the physical properties studied in the present work are not sensitive to the choice of the thermostat.

[100] I. Solov'yov, A. Yakubovich, P. Nikolaev, I. Volkovets and A. Solov'yov, *Journal of Computational Chemistry* **33**, 2412 (2012).

[101] G. De Las Cuevas, J. Faraudo and J. Camacho, *The Journal of Physical Chemistry C* **112**, 945 (2008).

[102] J. Weis, *Molecular Physics* **93**, 361 (1998).

[103] R. Chantrell, A. Bradbury, J. Popplewell and S. Charles, *Journal of Applied Physics* **53**, 2742 (1982).

[104] J. M. Tavares, J. J. Weis and M. M. Teloda Gama,*Physical Review E* **65**, 061201 (2002).

[105] K. Butter, P. Bomans, P. Frederik, G. Vroege and A. Philipse, *Nature Materials* **2**, 88 (2003).

[106] H. Schmidle, C. K. Hall, O. D. Velev and S. H. Klapp, *Soft Matter* **8**, 1521 (2012).

[107] M. A. Miller, R. Blaak, C. N. Lumb and J.-P. Hansen, *The Journal of Chemical Physics* **130**, 114507 (2009).

[108] M. T. A. Bos and J. H. J. van Opheusden, *Physical Review E* **53**, 5044 (1996).

[109] L. V. Woodcock, *AIChE Journal* **58**, 1610 (2012).

[110] G. E. Pike and C. H. Seager, *Physical Review B* **10**, 1421 (1974).

[111] A. L. R. Bug, S. A. Safran and I. Webman, *Physical Review Letters* **54**, 1412 (1985).

[112] F. Sciortino, P. Tartaglia and E. Zaccarelli, *The Journal of Physical Chemistry B* **109**, 21942 (2005).

[113] J. Weis, *Molecular Physics* **100**, 579 (2002).

[114] D. R. Nelson and R. A. Pelcovits, *Physical Review B* **16**, 2191 (1977).

[115] J. Toner and D. R. Nelson, *Physical Review B* **23**, 316 (1981).

[116] M. A. Bates and D. Frenkel, *The Journal of Chemical Physics* **112**, 10034 (2000).

[117] R. Tavarone, P. Charbonneau and H. Stark, *The Journal of Chemical Physics* **143**, 114505 (2015).

[118] M. Abkenar, K. Marx, T. Auth and G. Gompper, *Physical Review E* **88**, 062314 (2013).

[119] T. Geigenfeind, S. Rosenzweig, M. Schmidt and D. de las Heras, *The Journal of Chemical Physics* **142**, 174701 (2015).

[120] J. Dzubiella, G. P. Hoffmann and H. Löwen, *Physical Review E* **65**, 021402 (2002).

[121] H. Lowen, *Soft Matter* **6**, 3133 (2010).

[122] F. Ginelli, F. Peruani, M. Bär and H. Chaté, *Physical Review Letters* **104**, 184502 (2010).

[123] S. R. McCandlish, A. Baskaran and M. F. Hagan, *Soft Matter* **8**, 2527 (2012).

[124] A. F. Demirörs, J. C. P. Stiefelhagen, T. Vissers, F. Smallenburg, M. Dijkstra, A. Imhof and A. van Blaaderen, *Physical Review X* **2**, 021012 (2015).

[125] J. de Araújo, F. Munarin, G. Farias, F. Peeters and W. Ferreira, *Physical Review E* **95**, 062606 (2017).

[126] E. Bianchi, R. Blaak, C. N. Likos, *Physical Chemistry Chemical Physics* **14**, 13 (2011).

[127] B. Lemaire and P. Davidson, *Physical Review Letters* **88**, 125507 (2002).

[128] A. I. Abrikosov, S. Sacanna, A. P. Philipse and P. Linse, *Soft Matter* **9**, 8904 (2013).

[129] A. B. Yener and S. H. Klapp, *Soft Matter* **12**, 2066 (2016).

[130] J. L. C. Domingos, F. M. Peeters and W. P. Ferreira, *Physical Review E* **96**, 012603 (2017).

[131] W. Gao, M. Rigout and H. Owens, *Applied Surface Science* **380**, 12 (2016).

[132] L. Li, X. Jiao, D. Chen and C. Li, *Crystal Growth & Design* **16**, 2700 (2016).

[133] T. S. Shim, Z. G. Estephan, Z. Qian, J. H. Prosser, S. Y. Lee, D. M. Chenoweth, D. Lee, S.-J. Park and J. C. Crocker, *Nature nanotechnology* **12**, 41 (2017).

[134] H. Yuan, I. J. Zvonkina, A. M. Al-Enizi, A. A. Elzatahry, J. Pyun and A. Karim, *ACS Applied Materials & Interfaces* **9**, 11290 (2017).

[135] A. P. Eberle, N. J. Wagner and R. Castañeda-Priego, *Physical Review Letters* **106**, 105704 (2011).

[136] A. P. Eberle, R. Castanñeda-Priego, J. M. Kim and N. J. Wagner, *Langmuir* **28**, 1866 (2012).

[137] A. Bug, S. Safran, G. S. Grest and I. Webman, *Physical Review Letters* **55**, 1896 (1985).

[138] M. A. Miller and D. Frenkel, *The Journal of Chemical Physics* **121**, 535 (2004).

[139] K. May, A. Eremin, R. Stannarius, S. D. Peroukidis, S. H. Klapp and S. Klein, *Langmuir* **32**, 5085 (2016).

[140] E. De Miguel, L. F. Rull, M. K. Chalam and K. E. Gubbins, *Molecular Physics* **74**, 405 (1991).

[141] K. May, R. Stannarius, S. Klein and A. Eremin, *Langmuir* **30**, 7070 (2014).

[142] G. E. Box and M. E. Muller, *The annals of mathematical statistics* **29**, 610 (1958).

[143] C. S. Dias, C. Braga, N. A. M. Araújo and M. N. Telo da Gama, *Soft matter* **12**, 1550 (2016).

[144] A. Coniglio, U. De Angelis and A. Forlani, *Journal of Physics A: Mathematical and General* **10**, 1123 (1977).

[145] K. D. Machado, *Teoria do Eletromagnetismo* **2**, UEPG, Ponta Grossa, (2002).